LBL-37309
UC-401

Lawrence Berkeley Laboratory

UNIVERSITY OF CALIFORNIA

CHEMICAL SCIENCES DIVISION

Photoelectron Holography Applied to Surface Structural Determination

B.L. Petersen
(Ph.D. Thesis)

May 1995

Prepared for the U.S. Department of Energy under Contract Number DE-AC03-76SF00098

DISCLAIMER

LBL-37309
UC-401

Photoelectron Holography Applied to Surface Structural Determination

Barry Lee Petersen
Ph.D. Thesis

Department of Chemistry
University of California, Berkeley

and

Chemical Sciences Division
Lawrence Berkeley Laboratory
University of California
Berkeley, CA 94720

May 1995

This work was supported in part by the U.S. Department of Energy, Director, Office of Energy Research, Office of Basic Energy Sciences, Chemical Sciences Division at Lawrence Berkeley Laboratory under Contract No. DE-AC03-76SF00098, by Materials Sciences Division at Lawrence Livermore National Laboratory Office under Contract No. W-7405-ENG-48, and by both Materials Sciences and Chemical Sciences Divisions at the National Synchrotron Light Source, Brookhaven National Laboratory, under Contract No. DE-AC02-76CH00016.

Photoelectron Holography Applied to Surface Structural Determination

by

Barry Lee Petersen

B.S. (Harvey Mudd College) 1990

A dissertation submitted in partial satisfaction of the

requirements for the degree of

Doctor of Philosophy

in

Chemistry

in the

GRADUATE DIVISION

of the

UNIVERSITY of CALIFORNIA at BERKELEY

Committee in charge:

Professor David A. Shirley, Co-Chair
Professor Charles B. Harris, Co-Chair
Professor Angelica M. Stacy
Professor Steven G. Louie

1995

Abstract

Photoelectron Holography
Applied to Surface Structural Determination

by

Barry Lee Petersen

Doctor of Philosophy in Chemistry

University of California at Berkeley

Professor David A. Shirley, Co-Chair
Professor Charles B. Harris, Co-Chair

Photoemitted electron waves are employed as coherent source waves for angstrom-scale holographic imaging of local atomic geometry at surfaces. Electron angular distribution patterns with a specific electron kinetic energy are collected above a sample surface and serve as a record of the interference between the source wave and the waves scattered from surrounding ion cores. Upon application a mathematical imaging integral transformation, the three-dimensional structural information is obtained directly from these collected patterns. Patterns measured with different electron kinetic energies are phase-summed for image improvement .

A platinum (111) clean metal surface is used as a model system to experimentally verify the technique. A pattern measured at $k = 9.6\text{Å}^{-1}$ (351 eV electron kinetic energy) is used to generate a full three-dimensional image of atom locations around an emitter with nearest neighbors within 0.1Å of the expected bulk positions. Atoms several layers beyond the nearest neighbors are also apparent. Twin-image reduction and artifact suppression is obtained by phase-summing eight patterns measured from $k = 8.8$ to 10.2Å^{-1} (295 to 396 eV). In total, thirty-two patterns were measured in 0.2Å^{-1} steps from $k = 6.0$ to 12.2Å^{-1} (137 to 567 eV) and are presented here.

Simple models of two-slit interference are compared with the electron scattering process to illuminate our understanding of the holographic recording of the structural

information. This view also shows why the technique occasionally fails due to destructive interferences. Simple theoretical models of electron scattering are compared to the experimental data to show the origin of the structural information and the differences that result from the atomic scattering process and from the nature of the source wave. Experimental parameters and their relationship to imaging is discussed. A detailed comparison is made to the platinum pattern measured at 351 eV using the simple theoretical model. The remaining data set is also modeled, and the eight appropriate theoretical patterns are used to regenerate the multiple-wavenumber experimental result.

A second metal system of a clean Cu (001) surface is also measured and imaged using the same technique. Using the copper system as an example, a study is done to show how this type of holography can have a tendency to favor the imaging of forward scattering atoms. This confirms the ability of the technique to be used in buried overlayer or interface studies, in addition to overlayer and bulk systems.

Dedication

This dissertation is dedicated to my parents,

Alene M. and Gary A. Petersen,

for their endless love, patience, and support.

Table of Contents

List of Figures

Acknowledgments

There are several individuals who have helped me immensely throughout the course of this research. In particular, I would like to thank Prof. David A. Shirley for his continuous interest and support, Lou Terminello for his invaluable consultation and his experimental expertise, and John Barton for his vision. I would also like to thank Zahid Hussain for his guidance and for his extensive knowledge of experimental physical chemistry.

Others who have contributed significantly to the process of this research include Alexis Schach von Wittenau, for sharing his computational knowledge, along with Wes Bethel and Jeff Moore, for helping with graphics presentations. Dawn Lapiano-Smith and C. Costas were instrumental in conduction of the experiments at Brookhaven. I would like to include the rest of the Shirley group, especially to Scot Kellar, Eric Hudson, Tony Huff, and Eddie Moler. I must also give credit to Prof. Philip C. Myhre, for his sound advice at the appropriate time.

Finally, I would like to thank those who offered personal support during the course of this program. I will always be indebted to my brother, for teaching me how to learn and for keeping a protective eye on my progress. Thanks also to Tobias, who stood by me from start to finish, Pam, for her generosity. I must also mention Steve, Chris, and Peter, for their time. Special thanks go to Tracy, who encouraged and supported me in the exploration of life outside of this research project.

This work was supported by the Director, Office of Energy Research, Office of Basic Energy Sciences, Chemical Sciences Division of the U.S. Department of Energy, LBL under Contract No. DE-AC03-76SF00098 and LLNL Office of BES, Materials

Science Division, under Contract No. W-7405-ENG-48, and was in part conducted at the National Synchrotron Light Source, Brookhaven National Laboratory, which is supported by the Department of Energy (Division of Materials Sciences and Division of Chemical Sciences of Basic Energy Sciences) under Contract No. DE-AC02-76CH0016.

Chapter 1

INTRODUCTION

This dissertation describes the successful application of photoelectron holography, a new approach to determining the relative positions of atoms on surfaces. The technique is based on a holographic interpretation of angle-dependent oscillations in the partial cross section for core-level photoemission from a single crystal system. These oscillations are superimposed upon an atomic-like background and observed with an energy selective electron spectrometer over the kinetic energy range of 100 to 600 eV. Following appropriate data analysis and reduction, full three-dimensional angstrom-resolution images of the positions of neighboring atoms near surfaces may be obtained for the direct elucidation of true local geometry around the emitting atom. This work will present an example of photoelectron holography applied to a model system, the (111) surface of platinum, in both single and multiple-wavenumber cases. The result will be compared to the simplest models of electron interference and scattering in order to assess the practical applicability of the method, as well as its limitations. To reinforce the assessment, a second system, the (001) surface of copper is also presented. This analysis of well-known systems will experimentally verify photoelectron holography as a new direct technique with some unique characteristics for subsequent application to more sophisticated surface structural determinations.

This introduction will be concerned with establishing a basis for the following study and with describing the contents in more detail. The first section will present the

material in general terms in order to clarify the purpose of the work and its relationship to chemistry and physics. It will be presented in a manner that does not require specific knowledge of the field and makes the material accessible to the non-specialist. The next two sections will be more specific in outlining first some of the historical background which led to this work, followed by a statement of the purpose of these studies. The fourth and final section will present a concise description of the contents of this dissertation and their interrelationships.

I. General Overview

One of the most fundamental questions a chemist asks is how chemical reactions take place. Pursuing this question can lead to the discovery of why an observed reaction occurs and eventually to the capability of harnessing this knowledge for potential benefit. It is necessary for the experimentalist to find creative solutions to these questions. Often, this requires a wide-ranging, general knowledge of the physical world, for the most productive application to any particular problem. A single method may give the required answer, or it may require a combination of various physical tests to determine a suitable answer to the question posed.

Although the majority of chemical studies focus on systems of homogeneous phase, the study of solid surfaces probes the interaction of atoms or molecules at the solid-gas interface. In this case, atoms of the bulk solid or in free gaseous states are constrained to different configurations than those which are otherwise unperturbed. An atom or molecule constrained to a specific configuration due to its interaction with a surface may provide information about the chemical states accessible to that species, and often its reactivity changes. This is due to the nature of the associated chemical bonds and electron sharing between the surface and adsorbate. Techniques used to study bulk or gaseous systems may be inappropriate for surfaces due to the lower relative concentration of surface to bulk atoms. In these cases, systems must be found with a high

surface-to-bulk concentration, or more commonly, techniques must be applied which have a high sensitivity to the surface region.

The tools used for probing surfaces follow from an understanding of the physical world. Electromagnetic radiation in its may forms can be used to change or disturb the systems of interest, and the extent of the disturbance is measured and used as clues to understanding the causes of the observed effect. The large body of solid state physics research can be applied in these studies, along with the techniques of other fields. As shown in some of this work, the study of waves and optics also applies, where electron waves act similarly to the traditional visible wave counterpart. In the present study, chemistry and physics merge to answer some fundamental questions about the organization of atoms at surfaces.

The work presented in this thesis involves the successful application and explanation of holography using electron waves to image the position of atoms in crystals. It is helpful here to draw the analogy between optical and electron holography. While there are many different ways of performing holography experiments, the most general version is shown in Figure 1.1a. In this configuration, coherent light which travels directly to a detector is combined with the same light reflected from a three-dimensional object. The two waves cover different distances, and the phase difference between the original (source) wave and the reflected wave is recorded at the detector in the form of a two-dimensional interference pattern, which is the 'hologram.' By re-illuminating this interference pattern with the original coherent source wave, a three-dimensional virtual image may be obtained. An analogous situation occurs in the case of photoelectrons [1,2], shown in Figure 1.1b. In this case, however, the coherent wave source is the photoemitted electron wave emanating from the emitting source atom. This wave also propagates to the detector and scatters off the surrounding atoms. The original and the scattered waves meet at the detector to produce an interference pattern, which may be transformed mathematically to reveal the three-dimensional location of atoms

surrounding the emitter. The major difference between the two cases, and the reason for using electron waves, is the associated wavelength. The de Broglie wavelength of electrons, where $\lambda = \sqrt{150 / E_K(\text{eV})}$, in the 50-1000 eV range is much smaller (λ=1.7 to 0.4Å) than that of visible light. Additionally, the mean free path of electrons in this range is relatively small (~<10Å) making them much more surface-sensitive than corresponding photons of comparable wavelength.

The strength of this technique lies in its direct characteristics. Because images of the crystal structure are obtained directly from the data without the need for theoretical fitting schemes, the result produced is not encumbered with the ambiguity associated with theoretical fits. Results obtained in this way have much greater reliability and the theory serves only as a check against major discrepancies. As experimentalists, we cannot assume the theory is infallible before starting the experiments. In these electron holography experiments, true information is provided solely from the measured data. Theoretical comparisons are only used in attempts to confirm our predictions about the origin of this measured data.

The experiments described in this study were carried out using a two dimensional electron analyzer [3], schematically shown in Figure 1.2. This analyzer allows for the collection of electrons of a specific kinetic energy in two dimensions over an 84° solid angle above the sample. The samples in these studies were pure single crystal metals, approximately 1/4" thick, cut and polished along the surface of interest. These ideal surfaces are necessary to direct and simplify the questions asked. These crystals were affixed to a goniometer mounted inside a stainless steel vacuum chamber which housed the analyzer. The surface was then cleaned using cycles of ion bombardment and annealed in ultrahigh vacuum ($<10^{-9}$ torr) to give clean, ordered surfaces with only the metal species of interest detectable. The crystal is exposed to linearly polarized soft x-rays and the analyzer is adjusted to collect only those electrons from the core level of interest. The number of electrons is counted at each angle and over several electron

kinetic energies. The electron intensity varies with both angle and energy, giving rise to the interference pattern.

The chemical principles we want to explore are measured by a variety of physical techniques. These measurements produce a pattern analogous to an optical hologram which must be inverted mathematically to form a three-dimensional image of crystal structure. The formalism for this transformation has been previously established [2] and will be applied primarily to a collected platinum (111), but also to a copper (001) data set. Additionally, there are conditions when the transformation will be unsuccessful due to inherent characteristics of the application of the transformation on electrons in crystals. These topics will be addressed in the following chapters.

II. Historical Background

The main elements of this work follow in a natural progression from previous work done in the area of surface structural analysis. Since reviews of material specific to the given chapter are included in those chapters, this review will be more general in scope. The goal is to define the context from which photoelectron holography developed and to establish the problems it is best suited to solve.

Atomic scale structural determinations in crystals have been standardized for some time. Of these, x-ray diffraction is most commonly used for determination of bulk crystalline samples. Additionally, the technique of extended x-ray absorption fine structure (EXAFS) [4,5] has also been used for bulk studies. It involves a core-photoelectron final state interference which takes place on the emitting atom, generating fine structure modulations of the photoabsorption cross section. Fourier analysis of these fine structure modulations give information about the radial bond lengths of nearest neighbors surrounding the specific atom probed. The advantage of EXAFS is its sensitivity to the different chemical species within the sample. There are other techniques as well, but these two require the use and detection of x-rays.

When the atoms of interest lie on or near the surface, alternative techniques must be applied which are sensitive to this region. Many creative solutions to this problem have been employed, and some of the more common applications will be described here. Two direct techniques, scanning tunneling microscopy [6] and atomic force microscopy [7], provide angstrom-resolution images of the topmost surface layer by exploring that layer directly from above. The strength of these probes is their ability to produce a measurement of an area of a surface without implicitly requiring theoretical comparison. Of the many other methods employed, surface extended x-ray absorption fine structure (SEXAFS) [8], low energy electron diffraction (LEED) [9], and angle-resolved photoemission extended fine structure (ARPEFS) [10] are used most often and are also the most quantitative. Surface EXAFS is simply a surface-sensitive form of EXAFS in which an adsorbate core-level is used as the photoexcitation initial state which generates surface geometrical information [11]. The other two methods, LEED and ARPEFS, take advantage of the limited mean free paths of electrons in the 50-1000 eV energy range caused by inelastic scattering. In LEED, a primary electron beam is incident on a surface of long range order and the reflected electrons are detected. The measured two-dimensional LEED pattern provides direct information about the periodicity and translational symmetry of a surface. More detailed information, such as bond lengths and the actual relative location of the surface atoms within a unit cell, are obtained from measured intensities in a manner similar to x-ray crystallography, by comparison of measured results to computationally intensive theoretical calculations. LEED is also mostly insensitive to the nature of the chemical species involved. ARPEFS employs the angular dependent variation of electron intensity over wavenumber which exploits for structure the interference between the probability amplitude for the photoemitted electron to travel from the ionized atom to the detector and that for the electron to scatter from a nearby atom. A combination of Fourier analysis and theoretical fitting are used to establish the local geometry around a chemically specific emitting atom. Since

photoelectron holography as applied here is derived from the electron scattering theory and intuitive view commonly applied to ARPEFS, it is instructive to cover this topic more extensively here.

Strong interference effects were first observed in photoemission from single crystal substrates by Siegbahn [12] and Fadley and Bergstrom [13]. The modulation of the photoemission partial cross-section of a core level of substrate or adsorbed atoms as a function of electron kinetic energy angle was predicted as a "final-state interference effect" [14,15] which could be used to probe surface structure. This prediction was confirmed later [16-18] and was given the rather misleading although functional name of 'photoelectron diffraction.' 'Photoelectron interference' may be more descriptive of the physical phenomenon which occurs. The experiments involved using core-level photoelectrons or core-like Auger transitions and observing the modulations in the resulting photoemission intensities. Figure 1.3 illustrates the basic principle described here. A core-level electron is ejected from a surface atom by a monochromatic beam of energy hv. The kinetic energy of the emitted electron is equal to the photon energy less the core-level binding energy. Using the de Broglie relation, the wavevector k of the emitted electrons may be obtained:

$$k = \frac{\sqrt{2m_e(E_K + V_0)}}{\hbar}, \qquad (1)$$

where m_e is the rest mass of an electron and V_0 is the inner potential of the solid. The outgoing wave travels either to the detector directly or to other parts of the crystal, where it is scattered off of the surrounding atoms before going to the detector. The path length difference of the two waves reaching the detector creates a phase difference between the two waves and is recorded as an interference effect. By changing the angle of observation or by varying the energy of the incident photons, the measured interference intensity modulates, thus exhibiting the changes in the interference effect and making it more readily tractable.

Scanned angle photoelectron measurements, generally termed x-ray photoelectron diffraction (XPD), involve varying the direction of observation while fixing the electron wavevector. Azimuthal photoelectron diffraction [19] and polar photoelectron diffraction (PPD) [20] fall into this category. These methods take advantage of the strongly peaked forward scattering features at high electron wavenumbers. Although inappropriate for atomic-adsorption emitter systems, it serves well for determining the angular position of atoms between the emitter and detector. However, bond length information is not obtainable using these techniques since there is no significant measured phase difference for the directly forward-scattered atoms.

In comparison to angle measurements, experiments have also been done which vary the wavenumber of the emitted electrons by changing the photon energy. This is usually done by using a tunable photon source of appropriate range, such as a synchrotron. Early experiments employing this scanning method measured photoelectron intensity in the direction of the surface normal and were termed normal photoelectron diffraction (NPD) [21]. In these experiments, the intensity of electrons from 50 to 200 eV was compared to LEED-like "quasikinematic" simulations [22]. Since it focuses on reflections from planes of atoms, results obtained from this technique tended to emphasize the perpendicular distance between adsorbate overlayers and the substrate without equal sensitivity to all other structural parameters.

The development of angle resolved photoelectron extended fine structure (ARPEFS) resulted from an attempt to take advantage of energy-dependent photoemission data from off-normal emission directions. Instead of a LEED-like approach, ARPEFS followed the cluster based EXAFS approach, which focuses more on the photoelectron final-state interference effect. However, the EXAFS oscillations depend on the total x-ray absorption spectrum, which relates them to an integral of the ARPEFS oscillations over all emission angles [15] and over all final states excited at a particular x-ray photon energy [23]. ARPEFS also usually spans a kinetic energy range

of 100 to 600 eV in order to give higher resolution in Fourier analysis transforms and to avoid some of the more purely isotropic electron scattering that occurs at lower energies. Using a two-step process of Fourier transformation for path length estimates and comparison to proposed adsorption sites followed by a full multiple scattered wave theoretical calculation, the best structure is determined according to the trial simulation structure giving the best agreement between experiment and theory. This technique is capable of giving good results, however, the analysis can be time consuming and the final results have an inherent ambiguity owing to the arbitrary nature of the selection of parameters. By performing ARPEFS at several different angles some of this ambiguity may be decreased, but the time requirements are still a limiting factor.

In 1986, Szöke [1] recognized the relationship of the scattering problem in crystals to holography. The photoemitted electron wave constituted a source wave, and the scattered waves at the atom cores could be related to reflected waves which would recombine with the source wave in the far-field region at a detector above the surface. The measured two-dimensional interference pattern is effectively a hologram, and proper treatment of this pattern should give a three-dimensional image of the local environment around the source atom. Barton in 1988 [2] recognized the similarity of the holography proposal to the ARPEFS technique and established the formalism for data interpretation based on previous ARPEFS work. A brief description of this formalism follows.

If the photoemitted wave is labeled $\psi_0(\boldsymbol{k})$ and the primary scattered wave from a single neighboring atom is $\psi_S(\boldsymbol{k})$, then the total combined wave at the detector, $\Psi_T(\boldsymbol{k})$, is given as:

$$\Psi_T(\boldsymbol{k}) = \psi_0(\boldsymbol{k}) + \psi_S(\boldsymbol{k}). \qquad (2)$$

The form of $\psi_0(k)$ depends on the initial state and $\psi_S(k)$ is dependent on $\psi_0(k)$ with an added scattering factor modification. The intensity at the detector is given as the square of the amplitude, or:

$$I_T(k) = |\Psi_T(k)|^2 = \psi_0^* \psi_0 + \psi_0^* \psi_S + \psi_S^* \psi_0 + \psi_S^* \psi_S. \quad (3)$$

The interference portion, $\chi(k)$, is given as:

$$\chi(k) = \psi_0^* \psi_S + \psi_S^* \psi_0 \quad (4)$$

$$= \frac{I_T(k) - I_0(k)}{I_0(k)} \quad (5)$$

where we have made use of the fact that $\psi_S^* \psi_S$ is small compared to $\chi(k)$ and $I_0(k) = \psi_0^* \psi_0$. In the single scattering model, including all of the scattering atoms and a generalized source wave, the photoelectron intensity $\chi(k)$ can be expressed as (see Figure 1.3):

$$\chi(k) = \sum_j A_j(k) \cos\left[kr_j(1-\cos\theta_j) + \phi_j\right], \quad (6)$$

where $A_j(k)$ is an angular dependent combination of non-structural factors and ϕ_j is the scattering phase shift.

In the case of ARPEFS, the first step is a one dimensional Fourier transform over the wavenumber index, which gives path length differences as $r_j(1-\cos\theta_j)$. In holography, the procedure is different. Rather than an initial transform over wavenumber, the transformation is done over angle. The form of the integral is obtained

from the Helmhotlz-Kirchoff integral theorem [24]. Knowing the wavefield on the surface of a sphere allows the wavefield in the interior to be derived from Green's theorem. The result is a Fourier-like integral:

$$U(\boldsymbol{r}) = \frac{1}{2\pi R^2} \iint_S \chi(\hat{\boldsymbol{k}})\, e^{-i\boldsymbol{r}\cdot\boldsymbol{k}} d\sigma \tag{7}$$

For most values of $\boldsymbol{r}$, the exponential terms oscillate and the result is small image intensity. When $\boldsymbol{r} \approx \pm r_j$, the exponential terms are always near 1 and a large image intensity can occur. Expressing this imaging integral in terms of k_x and k_y, the relationship to the more familiar double Fourier integral is obvious:

$$U(r) = \frac{1}{2\pi R^2} \int_{-1}^{1} \int_{-1}^{1} \chi(\hat{\boldsymbol{k}}) \exp[ikz(1-\hat{k}_x^2-\hat{k}_y^2)^{1/2}] \exp(ikx\hat{k}_x + iky\hat{k}_y) d\hat{k}_x d\hat{k}_y \tag{8}$$

The angle variables, k_x and k_y, are conjugate to the two lateral space variables x and y. The third dimension in real space, z, comes from a phase factor [2]. The transform is done repeatedly at a single wavenumber over the vertical index z and stacked in order to obtain the final three-dimensional image. In most cases the two-dimensional Fast Fourier transform may be used.

Armed with a technique of quickly handling all of the angular data at a single wavenumber, the formalism for a multiple-wavenumber analysis followed in 1991 [25]. This technique involves a phased-sum approach, in which the transformed real-space volume is multiplied by a phasing term and summed over wavenumber according to:

$$M(\boldsymbol{r}) = \sum_i F_i(k_i, \chi_i, \boldsymbol{r}) e^{-ik_i \boldsymbol{r}}, \tag{9}$$

where $F_i(\boldsymbol{r})$ represents the full three-dimensional volume obtained in the single wavenumber case. This summation has the combined benefits of reducing twin-image intensity and eliminating artifacts due to multiple scattering. Most importantly, this provided a direct surface sensitive technique which took advantage of both angular and kinetic energy data.

The primary difference between ARPEFS and holography is the predilection of ARPEFS to preferentially image backscattering atoms. Conversely, in cases where there are forward scatterers, holography will tend to image the forward scattering atoms in energy ranges where forward scattering dominates. In all other cases, holography will give equal weight to all atoms dependent only upon the distance the wave must travel to the detector and surrounding atoms, thus providing a true full three-dimensional image. ARPEFS is sensitive to phase changes with wavenumber, which will always be dominated by direct backscattering since this is the position of the greatest path length difference to the detector. In fact, many ARPEFS analysts remove all broad forward scattering information prior to transformation. Because it involves comparison to a theoretical model, ARPEFS generally gives much higher accuracy (±0.02Å) than the resolution of holography (~1Å, depending on electron kinetic energy). In these cases, holography may be more appropriate as a tool to obtain initial structures for other techniques, thereby reducing the ambiguity and time required for definitive structural determinations. Also, since holography is chemically specific and offers the ability to image forward scatterers, it may be applied to the imaging of buried interfaces much more successfully than previous studies with XPD.

In sum, photoelectron holography developed in a series of techniques designed to probe surface structure. It is one version of a methodology which employs the full range of measurable momentum-space data in order to perform a transformation to a useful real-space counterpart. Its major advantage, which it shares with some of its predecessors, is the ability to select and use the emitting atom itself as a source which

probes the local atomic environment. It is important to stress the connection to EXAFS and ARPEFS, from which this technique is essentially derived. The next section develops the specific purpose of this work and its relationship to the theory of photoelectron holography.

III. Purpose of this Work

The primary reason for conducting this research was to experimentally verify the proposed technique of photoelectron holography. In order to achieve this goal, the well-understood clean platinum (111) crystal surface was used as the main system for these experiments. Sample preparation was straightforward, the scattering characteristics of platinum were ideal, the bulk structure was well known from x-ray diffraction work, and the hexagonally closed packed atomic arrangement offered three uniquely different atomic arrangements in each layer for depth and imaging studies. For this project, the first step was to verify the success of the technique at a single wavenumber [2], and the second was to show the successful application of the multiple-wavenumber analysis [25] to the same system. Once the method for applying the technique was established, it was important to verify the work with a second simple system, the (001) surface of copper.

The secondary purpose was to gain knowledge about the application of this technique to real systems. As with almost any method, there are cases where routine application of the principles described will not produce the desired result. Additionally, the specific methods of analysis or configuration of the experiment may determine the final result. In these situations, it is important to know why discrepancies occur, when they may occur, and what can be done to recover from any potential losses. This is one of the advantages of having a complete enough data set to thoroughly explore. Concepts detailed in the current study should be applicable to other more complex systems.

In order to fully understand the origin of the measured data and the meaning of the corresponding results, a theoretical comparison is required. Of course, the technique

itself should not require such a comparison, since it is direct, but such a comparison helps to confirm and establish the cause of the previously obtained results. Because the holographic component of this imaging technique is based in simple theory, the theoretical models used in this work focus on the fundamentals of electron scattering theory. The primary reason for using simple theoretical models is that they make possible two connections. First, by knowing the origins of the measured intensities, it is possible to assess how any image forms from its corresponding pattern. Second, by directly comparing the more complex measured data to the simple model result, image formation (or lack of image formation) may be understood by means of a comparison of the measured patterns and theoretical patterns which should give the ideal holographic imaging result. As more complex atomic elements are added to the theoretical model, it is possible in most cases to establish how an experimentally measured pattern may produce a result dissimilar to that expected. In short, the adherence to simple theoretical models in this study stems from the attempt to understand the most basic models of electron scattering in solids and their direct connection to holographic imaging. Because highly quantitative comparisons may in many cases give inadequate holographic images, it makes no sense to fit the data exactly - the real value for the direct nature of the technique will involve noting the similarity between experiment and simple theory.

The final purpose of this work is to assess the applicability of photoelectron holography as a technique and to use this assessment in the design of future experiments. These experiments and corresponding analyses begin to predict more obvious uses for the technique and methods of improving its reliability. Future experiments employing this particular technique stand to benefit from the information gained here. Interfaces, adsorbates, and bulk systems may be explored. In addition, the experimental design parameters of the most useful kinetic energy or angle ranges, and the most appropriate analyzer configuration also stem from this work. The conclusions made here will lead to

a better understanding of the most favorable parameters and expectations of success for imaging surface atomic geometry with photoelectron holography.

IV. Contents

In consideration of the historical setting and the purpose guiding this research, the contents of this dissertation are now outlined. The next five chapters result from work done on an extensive platinum (111) data set which contains thirty-two patterns measured from k = 6.0 to 12.2 $Å^{-1}$ with a step size of 0.2$Å^{-1}$. The first two chapters following this introduction describe the successful application of the technique of photoelectron holography to the experimental set, first in terms of a single wavenumber analysis, at k = 9.6$Å^{-1}$ (351 eV), and then using the multiple wavenumber analysis scheme for eight of the patterns, from k = 8.8 to 10.2$Å^{-1}$ (295-396 eV). Chapter 4 describes in detail a fundamental limitation of photoelectron holography, image intensity variations due to the presence of more than a single scattering atom. In Chapter 5, the single wavenumber result of Chapter 2 at k = 9.6$Å^{-1}$ is described in detail using simple theoretical constructs along with a more complete study of the origin of the formed images. Chapter 6 concludes the platinum study with a presentation of the full platinum data set along with a simple theoretical comparison. Also in Chapter 6, the multiple wavenumber result of Chapter 3 is reproduced theoretically. In Chapter 7, a similar application of the developed analytic technique is done in order to improve the previously published results of a copper (001) data set of nine patterns measured from k = 8.0 to 11.2 $Å^{-1}$, as a further verification of the conclusions of the platinum work. Chapter 8 concludes this work with some speculation about the directions for future work in this area.

References

[1] A. Szoke, in *Short Wavelength Coherent Radiation: Generation and Applications,* edited by D.T. Atwood and J. Bokor (AIP Conf. Proc. 146, New York, 1986).

[2] J.J. Barton, Phys. Rev. Lett. 61 (1988) 1356; J.J. Barton, J. Electron Spectrosc. Relat. Phenom. 51 (1990) 37.

[3] D.E. Eastman, J.J. Donelon, N.C. Hien, and F.J. Himpsel, Nucl. Instrum. Methods 172 (1980) 327.

[4] Edward A. Stern, Phys. Rev. B 10 (1974) 3027.

[5] P.A. Lee and J.B. Pendry, Phys. Rev. B 11 (1975) 2795.

[6] G. Binnig and H. Rohrer, Helv. Phys. Acta 55, (1982) 726.

[7] G. Binnig, C.F. Quate, and C. Gerber, Phys. Rev. Lett. 12 (1986) 930.

[8] J. Stöhr, D. Denley, and P. Perfetti, Phys. Rev. B 18 (1978) 4132.

[9] J.B. Pendry, *Low Energy Electron Diffraction* (Academic, London, 1974).

[10] J.J. Barton, C.C. Bahr, Z. Hussain, S.W. Robey, J.G. Tobin, L.E. Klebanoff, and D.A. Shirley, Phys. Rev. Lett. 51 (1983) 272.

[11] M. DeCrescenzi, L. Papagno, G. Chiarello, R. Scarmozzino, E. Colavita, R. Rosei, and S. Mobilio, Sol. State Commun. 40 (1981) 631.

[12] K. Siegbahn, U. Gelius, H. Siegbahn and E. Olsen, Phys. Lett. 32 A (1970) 221.

[13] C.S. Fadley and S.A.L. Bergstrom, Phys. Lett. 35 A (1971) 375.

[14] A. Liebsch, Phys. Rev. Lett. 32 (1974) 1203; A. Liebsch, Phys. Rev. B 13 (1976) 544.

[15] P.A. Lee, Phys. Rev. B 13 (1976) 5261.

[16] S. Kono, C.S. Fadley, N.F.T. Hall, and Z. Hussain, Phys. Rev. Lett. 41 (1978) 117.

[17] D.P. Woodruff, D. Norman, B.W. Holland, N.V. Smith, H.H. Farrel, and M.M. Traum, Phys. Rev. Let 41 (1978) 1130.

[18] S.D. Kevan, D.H. Rosenblatt, D. Denley, B.C. Lu, and D.A. Shirley, Phys. Rev. Lett. 41 (1978) 1505.

[19] P.J. Orders, R.E. Connelly, N.F.T. Hall, and C.S. Fadley, Phys. Rev. B 24 (1981) 6163.

[20] D.A. Wesner, F.P. Cohen, and H.P. Bonzel, Phys. Rev. Lett. 60 (1988) 1045; D.A. Wesner, F.P. Cohen, and H.P. Bonzel, Phys. Rev. B 39 (1989) 10770.

[21] S.D. Kevan, D.H. Rosenblatt, D.R. Denley, B.C. Lu, and D.A. Shirley, Phys. Rev. B 20 (1979) 4133; S.D. Kevan, R.F. Davis, D.H. Rosenblatt, J.G. Tobin, M.G. Mason, D.A. Shirley, C.H. Li, and S.Y. Tong, Phys. Rev. Lett. 46 (1981) 1629.

[22] S.Y. Tong, C.H. Li, and A.R. Lubinsky, Phys. Rev. Lett. 39 (1977) 498; C.H. Li, A.R. Lubinsky, and S.Y. Tong, Phys. Rev. B 17 (1978) 3128.

[23] J.J. Rehr, E.A. Stern, R.L. Martin, and E.R. Davidson, Phys. Rev. B 17 (1978) 560.

[24] M. Born and E. Wolf, *Principles of Optics* (Pergamon, Oxford, 1980).

[25] J.J. Barton and L.J. Terminello, in Structure of Surfaces III, Milwaukee, edited by S.Y. Tong, M.A. Van Hove, X. Xide, and K. Takayanagi (Springer-Verlag, Berlin, 1991) 107; J.J. Barton, Phys. Rev. Lett 67 (1991) 3106.

Figure Captions

Figure 1.1. *Optical and electron holography comparison.* This figure shows the relationship between optical and electron holography. a) In optical holography, the coherent photon wave reflects off an object and recombines at the detector with the source wave. b) In electron holography, the coherent wave is the emitted electron wave resulting from the photoemission process. Nearest neighbors act as the object which reflects this wave, and the interference pattern is collected with an electron detector.

Figure 1.2. *Ellipsoidal mirror display analyzer.* This is a schematic depicting the ellipsoidal mirror analyzer used in these experiments. This energy selective spectrometer measures electron intensity for all angular (momentum) directions in an ~85° cone.

Figure 1.3. *Geometric scattering relationships.* This schematic shows the geometric relationships between surface atoms and the experimental variables. The photons of a given polarization are impingent upon an emitter (E) which emits a photoelectron wave to scattering atoms (S) with a total path length to the detector determined by the distance r_j to the scattering center and the angle θ_j subtended around the emitter between the detector and this scattering center. The energy selective electron spectrometer can also be varied in angle and is shown here in the position normal to the surface.

a) **OPTICAL:**

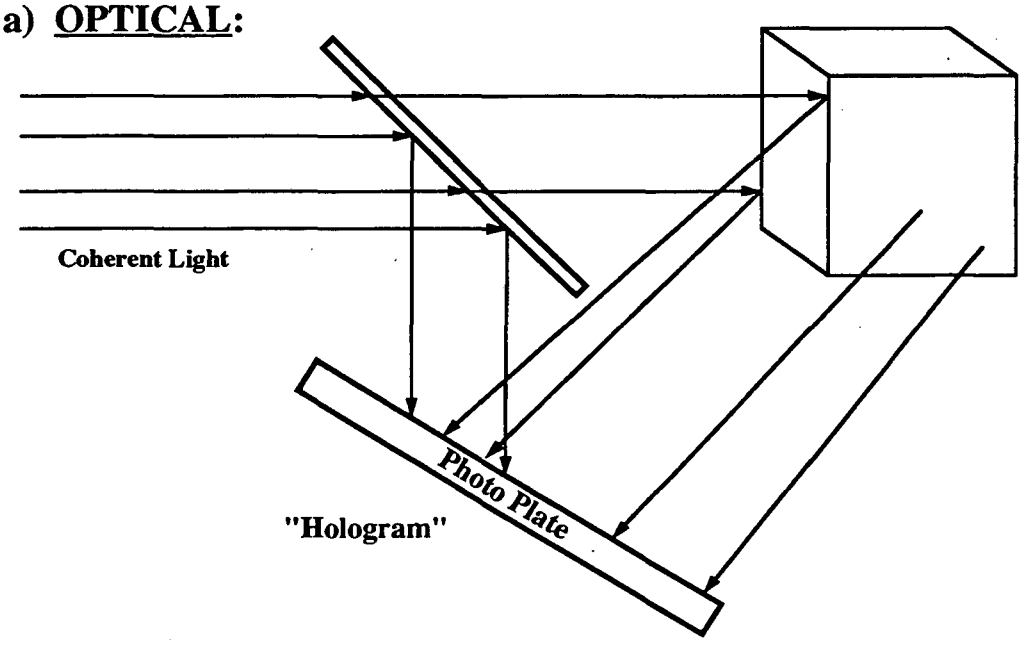

b) **ELECTRONS:**

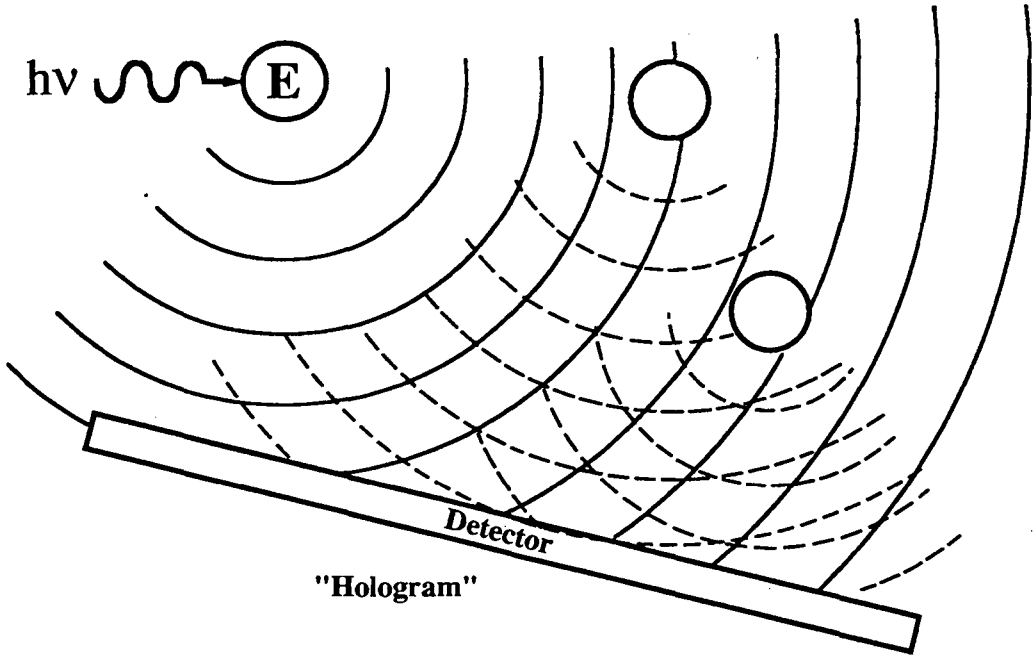

Figure 1.1

Ellipsoidal Mirror Display Analyzer

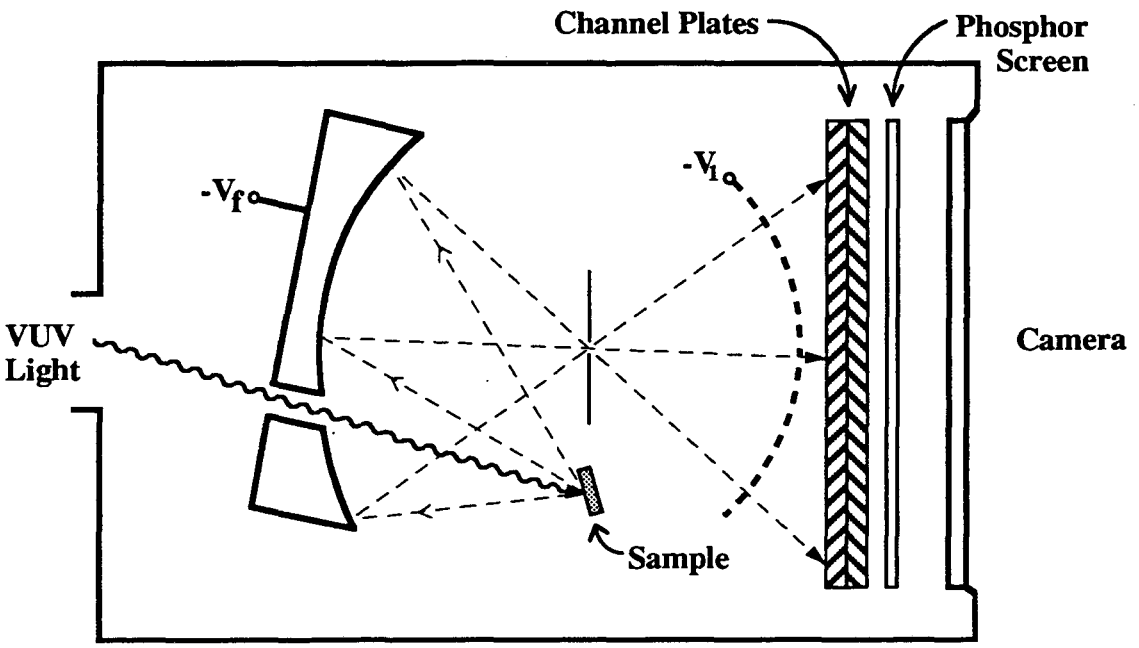

Figure 1.2

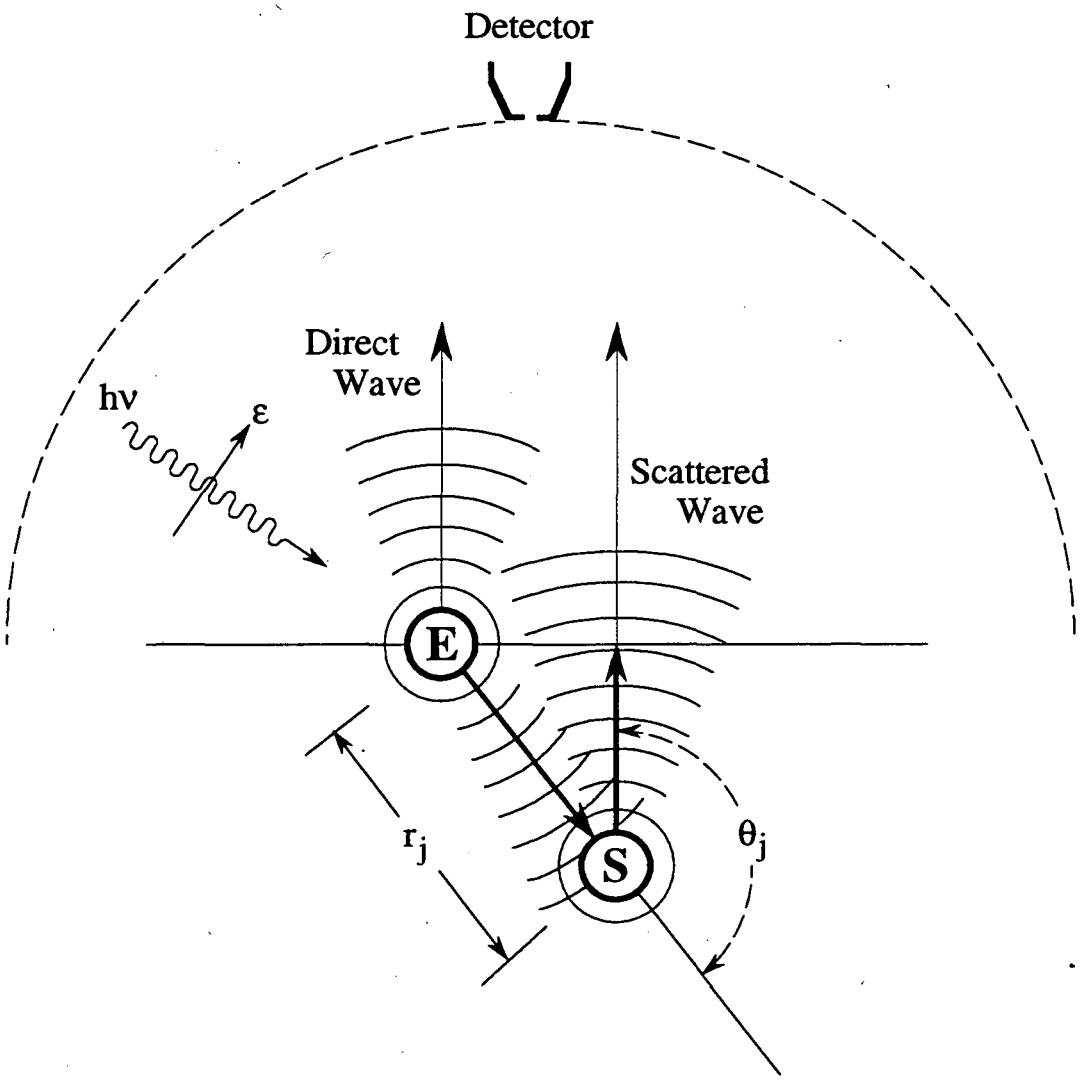

Figure 1.3

Chapter 2

PHOTOELECTRON HOLOGRAPHY OF PT(111) AT 351 eV

Abstract: A 351-eV photoelectron hologram of a Pt(111) surface was collected by detection of photoelectrons from the $4f_{5/2}$-subshell in a display analyzer, and was Fourier-analyzed. The real space image showed sensitivity to the fourth atomic layer, excellent reproduction of the fcc lattice, and sixteen source-atom neighbors. Transverse atomic positions were located to 0.1 Å. Photoelectron holography is thus shown to be capable of imaging lattices and interfaces, using low-energy electrons.

I. Introduction

Photoelectron holography was suggested by Szöke[1] and Barton[2] as a method for imaging atomic surface structures. The angular distribution of photoelectrons from a particular atomic core level in an atomic surface system is the electron hologram of the system at one electron energy. Fourier inversion can produce a real space image of the local atomic structure, with the source atom at the origin. While photoelectron holography derives from the process of photoelectron diffraction, it can in principle yield a structure explicitly, i.e., directly, rather than implicitly, by trial-and-error comparison of data with model structures.

In a number of reports on photoelectron holography during the past few years [3-9], the real space images have been rather distorted. This difficulty has been discussed by several authors, and multiple problems have been identified, with proposed solutions [10-

17]. In fact, however, the value of the method for determining unknown structures is still somewhat uncertain and perhaps controversial [18,19]. Accuracies in interatomic distances as poor as 0.3-0.5 Å have been quoted in some cases; in sharp contrast to the precisions of 0.01-0.02 Å reported for angle-resolved photoemission extended fine structure (ARPEFS) studies [20,21], which also employ photoelectron diffraction. While swept-angle, fixed-energy photoelectron diffraction data have been used directly to derive qualitative atomic structures, a holographic data set (which is equivalent to an ensemble of many fixed-angle data sets) can contain enough information to yield a more accurate structure, if certain experimental conditions are met. In this work, the observation and analysis of such a data set is reported for a Pt(111) crystal surface.

Two key features of our experiment were the choice of a photon energy that would produce medium-energy (351-eV) photoelectrons and the use of a relatively large solid-angle electron display analyzer. The electron energy was carefully chosen as high enough to avoid serious loss of resolution, but low enough to retain large photoelectron-diffraction and interference effects over relatively large scattering angles. At low electron energies (ca 100 eV and lower) $|k|$ is too small to give good image resolution, while at high energies (ca 1000 eV) Debye-Waller damping reduces the signal to noise ratio for a given counting time. Many ARPEFS results have consistently shown these two effects: the experimental diffraction curves become hard to simulate as the energy is lowered toward 100 eV, while the oscillatory amplitudes of ARPEFS curves decrease dramatically by 500 eV [20,21].

The use of a large-solid-angle display analyzer is advantageous, because the spatial resolution available in the real space image derived from a photoelectron hologram is "diffraction-limited" by the data range in the corresponding momentum variable. This is in turn determined by the solid angle of data collection. In this regard, the normal ("z") coordinate resolution is always at a disadvantage in a fixed-energy, scanned angle photoelectron holography experiment. Even if the display analyzer could cover a complete hemisphere, only an angular range of π could be covered in the z coordinate, in contrast to

2π for the x and y coordinates. In the present experiment, the relative resolution in the z coordinate is much lower because the collection angle covers a range of ca 1 radian centered at the pole of the hemisphere, where the variation in k_z is very small. For this reason we shall find that the atom images will be represented by cigar-shaped objects: i.e., rather small circular spots in the x-y plane, but elongated features in the z direction.

II. Experimental

The (111) surface of a platinum single-crystal was cleaned by argon sputtering at $1x10^{-5}$ torr of argon for one hour, followed by resistively annealing for three minutes at ca 850° C. The sample cleanliness was monitored by the photoelectron spectrum of platinum, which was taken repeatedly throughout the experiment and compared to the initial spectrum obtained immediately after sample preparation. The crystal was oriented so that the surface normal formed the central ray of the electron "cone" accepted in the display analyzer. The crystal position was fine-tuned by observing the symmetry of the Fermi-surface map obtained from angular distribution patterns from valence-band photoelectrons. The photon beam was incident upon the crystal at a 45° angle, and the electric polarization vector was therefore oriented at 45° relative to the surface normal. All measurements were made at room temperature.

The data were collected with the ellipsoidal mirror display analyzer [23] on the IBM U8 VUV beamline [24] at the National Synchrotron Radiation Source at Brookhaven National Laboratory. The acceptance angle of the analyzer is ca 84°, with a typical instrumental energy resolution of 0.3 eV while measuring holograms and an angular resolution of 1/4°. For the present measurements the analyzer was operated in the constant-final-state mode, in which electrons of a single energy are collected. The photon energy was changed when background electrons at the same wavenumber were desired, and the analyzer voltages were kept fixed.

A background spectrum taken on the high-energy side of the photoelectron peak was used for normalization. The measuring time was ca. 2 hours for the background and ca. 1 hour for the higher-signal photopeak. The results reported in this chapter were derived from a single-energy data set, at a kinetic energy of 351 eV. Chapter 3 will be based on the analyses of multiple-wavenumber data sets [25].

III. Data Analysis

The data were collected in arrays of 512 x 512 pixels, each containing a value proportional to the collected electron intensity in that particular angular position. In addition to the array of photoelectron peak intensities, another complete image representing the background was also taken for each photon (and photoelectron peak) energy, and the final photoelectron intensity image was normalized against the corresponding background image to give normalized images which were used in further data-reduction steps. Standard image processing steps were then applied: correction for the intensity "signature" of the apparatus, mapping from angular to momentum space, smoothing by employing a low-pass filter for removing forward diffraction peaks, and channel-summing to produce a conveniently transformable matrix [9]. In some trials a windowing function was used in the transform process. All of these steps are either essential mathematical transformations or techniques for eliminating artifacts in the raw data. These are all believed to be inert steps in the sense that they may (and do) reduce the desired information (resolution) in the raw data, but they do not create false images. The imaging integral transform is finally applied to the momentum-space data set to give the final image in real space. The steps are discussed further below.

The initial division by the background according to

$$\chi(\theta,\phi) = \frac{I(\theta,\phi)}{I_0(\theta,\phi)} - 1, \qquad (1)$$

isolates the diffraction where I refers to the peak intensity image and I_0 represents that of the background. This procedure is a method used successfully in the analysis of ARPEFS data [26]. It has the twofold effect of giving an estimate of the total intensity due to background electrons (mostly inelastically scattered within the sample), and normalizing out the angle-dependent transmission function of the analyzer. The background is measured at an iso-energetic kinetic energy just above that of the photoelectron peak, which has been moved by lowering the photon energy, to avoid inclusion of the elastic or inelastic tail of the peak in the background function.

The initial data were collected as a hemispherical pattern projected onto a flat surface, or an angular map. The pattern was then converted from the angular map to a momentum space (k_x, k_y) coordinate system. This required knowing the total energy of the outgoing electrons as well as geometric relationships among the coordinates. Corrections were also made at this stage to account for the analyzer angular transmission and the pixel aspect ratio of the original data.

Slow oscillations arising from the original (atomic) photoelectron final-state angular distribution, or the reference wave, and broad diffraction features often gave false intensities near the center of the transformed image in real space, which were troublesome for identifying near-neighbor atoms. This problem was overcome by convoluting the data with a Gaussian and subsequently removing the convoluted function, in effect Fourier-filtering the data to remove low frequencies. The convoluted function was removed by division and subsequent subtraction of a unit field, leaving a pattern which oscillates around zero and thereby reducing unwanted intensity at the origin after transformation. The final data were quite stable with respect to variations in the Gaussian width. Edge effects from the division were minimized by circular trimming of the pattern edges.

Finally, channels were summed, reducing the 512 x 512 pattern to 64 x 64. This serves two purposes: it increases the signal to noise ratio in each pixel and it provides a good matrix density for Fourier transformation to an appropriate real space density. At this

point the suitably processed data set was ready for application of the imaging integral transform. The relation governing this process is

$$U(r) = \frac{1}{2\pi R^2} \iint_s \chi(\hat{K}) e^{-ikr\cdot\hat{K}} d\sigma, \qquad (2)$$

where $U(r)$ is the wave field amplitude in real space, R is the distance from the source where the spherical pattern was obtained, and $\chi(\hat{K})$ is the hologram. To obtain the real space image, the transform integral was applied, conveniently expressed as a double Fourier integral:

$$U(r) = \frac{1}{2\pi R^2} \int_{-1}^{1} \int_{-1}^{1} \chi(\hat{K}) \exp[ikz(1-\hat{K}_x^2-\hat{K}_y^2)^{1/2}] \exp(ikx\hat{K}_x + iky\hat{K}_y) d\hat{K}_x d\hat{K}_y, \quad (3)$$

where z acts as a parameter in the propagation phase shift for the image's third dimension [2]. Three-dimensional real space images were created as a collection of two-dimensional "z-slices" which span the vertical range of interest.

IV. Results

The experimental electron hologram of 351-eV photoelectrons from the Pt $4f_{5/2}$ core level of the Pt(111) single crystal is shown in Fig. 2.1a. The data have been treated as described above, by background division and Gaussian convolution, to reduce intensity variations arising from artifacts and effects not associated with photoelectron diffraction, and by symmetry-averaging, through both threefold rotation and twofold reflection, to eliminate both the above effects and intensity variations associated the photoelectron distribution pattern relative to the photon polarization direction. The contrast ratio is dramatic, due in part to tuning the photon energy so that the photoelectrons would fall in a relatively low-energy range where the amplitude of oscillations due to photoelectron diffraction is typically quite large. The threefold symmetry of this pattern, though

guaranteed by the averaging process, was in fact evident in the raw data prior to symmetry-averaging. Such symmetry is expected for this two-dimensional electron-intensity *k*-space plot for electrons collected around the surface normal relative to the fcc Pt(111) surface. This hologram represents the sum of contributions from photoelectrons originating from core levels of *all* the Pt atoms in the near-surface region. Given the known attenuation length (before an inelastic scattering event) of ca. 10 Å for electrons of this energy in Pt, most of the signal in the hologram must originate from core levels of atoms in the first few atomic layers.

A sketch of the atomic positions in this lattice is shown in Fig. 2.1b. The ABCA.... repetitive pattern characteristic of a fcc lattice is depicted for three layers above an arbitrary source atom, shown in black in the bottom layer, from which the photoelectrons propagate upward to contribute to the hologram. The actual experimental hologram is of course the sum of contributions from this atom (and all other atoms in the fourth layer, which are symmetry-equivalent), plus contributions from atoms in other layers above and below the fourth layer. Photoelectrons originating from core levels in fourth-layer atoms and beyond may be elastically scattered, as they propagate upward, by atoms in the third, second, or first layer (B, C, or A in Fig. 2.1b): thus these layers all contribute to the hologram, and we would expect them to appear in its real space image transform. Fortunately, the crystal lattice symmetry ensures that laterally equivalent scattering atoms image at nearly the same position in real space.

Figure 2.1c shows the two-dimensional "*x*-*y*" intensity slice, taken from the rotationally symmetry-averaged data set parallel to the surface and above the emitter at $z =$ 2.2 Å. This is conceptually equivalent to producing a tomographic image of the layer above the source, albeit only in the sense of a superposition of signals from many equivalent scattering atoms, rather than in a truly microscopic sense (i.e., of showing the neighbors around a particular atom). In depicting atomic positions a choice must be made as to how to represent the intensity. Several well-known methods are available (contour

plots, false colors, arbitrary cut-offs, among others). The real space image intensity was squared to highlight clearly the atomic positions (not atoms) as bright spots. This image-processing technique suits our need: to locate the atoms. The real space slice shown in Fig. 2.1c is very close to plane B in Fig. 2.1b (at 2.26 Å), and the six bright spots are attributable to the six atoms shown in light gray in plane B. Small white crosses, at the known nuclear positions for the Pt lattice, are also shown in Fig. 2.1c. The mean deviation of the centroids of the spots and crosses is about 5% from the center in the *x-y* plane: phase shifts in the outgoing photoelectron waves can easily create deviations of this magnitude. In fact, in comparison with typical images in the electron holography literature, these deviations are gratifyingly small.

The fourth atomic layer above the source atom is evident in Fig. 2.1d, which shows a real space intensity slice at a distance of $z = 6.7$ Å above the source atom. Seven atomic positions are evident: a center atom directly above the source atom and its six nearest neighbors in the *x-y* plane, shown as (top) plane A in Fig. 2.1b. Again the hologram from which this transform was generated was first rotationally symmetry-averaged. The real space images generated from non-symmetry-averaged holograms tend to highlight some atoms over others which should be equivalent by lattice symmetry, because of the strong symmetry-breaking effects of photon polarization in the photoelectric process. The images are nearly symmetrical, and the intensity discrepancies are understood in principle (angle distortion from the display analyzer).

The data is shown using iso-density surfaces, where objects shown are three-dimensional surfaces of equal intensity taken at about 60% of the total intensity of the real space data set. These representations are called "volume" views, since they represent a volume with an associated height, width, and length. A "volume" top view of the real space transform of the 351-eV hologram is shown in Fig. 2.2a (unaveraged) and in Fig. 2.2b (rotationally symmetry-averaged). Fig. 2.2c shows a top view of an array of small spheres placed at the atomic positions of the Pt(111) lattice, included as a model.

The similarities of these three plots are striking, and the differences are also important. First, the atomic positions depicted in Fig. 2.2a and 2.2b are in excellent agreement with the expected positions for a Pt (111) structure, again within 5% or better of expected results, as in Figs. 2.1c and 2.1d. Moreover, integration of the real space intensity profiles over a distance effectively spanning several atomic layers in the z-direction does not smear the patterns out over a large area, showing that the x-y position of the brightest region of intensity for each layer does not vary strongly with the z-coordinate. To support this conclusion, it may be noted that the volume top views in Fig. 2.2 are effectively the sums of many of the 2D tomographic slices shown in Figs. 2.1c and 2.1d. We shall see below that the 3D image of each atom is an elongated "cigar" of intensity aligned along the z-direction. That each intensity spot in Fig. 2.2 is quite small implies that the 3D "cigars" are in fact aligned very well along z. The model atoms of Fig. 2.2c are coded to represent the source-atom layer (A in Fig. 2.1b) as six black spheres, the next layer (B) as gray, and the next above (C) as white spheres. The central black sphere represents the atom three layers directly above the source atom. The accurate trigonal registry from all three layers is even stronger evidence of the z-independence of the x-y positions. The intensity variations in Fig. 2.2a among atoms that would be equivalent in the lattice, but for which this equivalence is removed by the polarization vector, are evident, but are complicated by the fact that the angular distribution pattern from $4f_{5/2}$ photoelectron photoemission has mixed d-wave and g-wave character, with unknown relative phase. Superposition of this pattern on the Pt(111) lattice can produce large intensity variations among otherwise equivalent atoms, which are apparently evident in Fig. 2.2a.

Figure 2.3 shows two "volume" side views of the Pt(111) intensity plots in real space, using rotationally-averaged data. The advantages and the remaining weakness of this approach to photoelectron holography are both evident in the two panels of Fig. 2.3. Thirteen atoms, not including the source atom, are detected in the correct relative positions, and all are within 1Å of the actual positions. Atoms are depicted as far away as three

atomic layers, and our data indicate that more distant atoms could also be studied. All of these features are distinct advantages. The twin images that are well-known in photoelectron diffraction imaging are present, shown as an inverse image through the emitter on the lower side of the included mesh plane. This is a weakness which can in principle be remediated by multiple-wavenumber studies [17]. The "cigar" shape of the 3D images, owing to the diffraction limit of our photoelectrons, is another weakness which gives a large spread of the atomic image in the z-direction. The resolution expected in this direction is 2.7Å [27]. Multiple-wavenumber studies over the appropriate range should also decrease this elongation.

The volume side view shown in Fig. 2.3a is tilted to show a total of 14 separate real atoms in and above the plane of the source atom, plus seven "twin" images below the plane. With care, all 21 images can be distinguished, counting both the real-atom images and their corresponding twin images below the plane. The inward shifts of the centroids of the cigar-shaped images arise from phase shifts [2, 22]. There are ways to ameliorate this undesirable effect [2, 10, 16], but further discussion of this subject lies outside the scope of the present study.

After perusing the 2D tomographic slices in Fig. 2.1 and the z-integrated volume views in Fig. 2.2, the 3D volume views in Fig. 2.3 show a more complete representation of the transformed real space images from which Figs. 2.1 and 2.2 were derived. The degree to which x-y lattice positions of the images retain their fidelity as z is varied (alluded to in the discussion of Fig. 2.2) is tested in the perspective depicted in Fig. 2.3b, which emphasizes the positions of planes at the expense of resolving individual atoms. The planes are indeed very well aligned, and no distortions are apparent.

V. Discussion

Photoelectron diffraction and holography combine to form still-developing methodologies, in which imaging and structure determinations sometimes tend to merge

and even perhaps to become confused. On the experimental side, several methods are often compared simultaneously, and rather arcane distinctions can be made about their relative applicability. Taking a more holistic view of photoelectron-diffraction phenomena, these new results are discussed in this broader context. Therefore, photoelectron diffraction shall be described more generally before discussing the findings of this work. Given the detailed presentation of results above, the discussion will essentially take on the character of conclusions.

Let us imagine photoemission from a particular core level in a small, ordered solid source, which can be a spot on an ordered single-crystal surface that is illuminated by a well collimated monoenergetic photon beam. We further specify that only full-energy (i.e., unscattered and elastically-scattered) electrons are detected. We can then envision a three-dimensional momentum space, superimposed on the corresponding real space axes, with the source located at the origin, to describe the momenta of the full-energy photoelectrons. Using a spherical polar coordinate system in momentum space (k, $\theta = cos^{-1} k_Z/k$, $\phi = tan^{-1} k_Y/k_X$), a fixed-photon-energy experiment will yield photoelectrons of fixed (full) energy

$$\frac{\hbar^2 k^2}{2m} = h\nu - B \qquad (4)$$

emitted over a hemispherical shell of radius k. This is the hologram, which can be integral transformed to yield a real space image based on a single photon energy (and a single photoelectron energy)--i.e., the present experiment. Alternatively, an azimuthal or polar "sweep" in real space, usually called XPD or APD, can be described in this spherical-polar momentum space as a corresponding azimuthal or polar sweep on the surface of the hemispherical shell, in which either ϕ is varied while k and θ are held constant, or θ is varied with k and ϕ constant. Such a sweep is a partial hologram, however several slices may be combined to form more complete holograms [8].

Generally speaking, inversion of the hologram will give a three-dimensional real space image explicitly (directly), of a quality which improves with increasing solid angle sampled in k-space. Various experimental limitations will lead to corresponding distortions of the real space image. For example, dominant forward scattering will stretch atomic images along the electron propagation direction [3, 16]. In the present case, limited variation in the k_Z coordinate (in a k_X, k_Y, k_Z system) leads to elongation in the z-direction: i.e., the "cigar" shape, with all the cigars aligned along the z-direction. Additionally, the hologram is dependent on the scattering geometry and the light polarization vector, hence the region of k-space measured and the experimental geometry will determine the amount of information obtained from individual scattering atoms. Although often distorted and not necessarily capable of yielding an accurate structure, the hologram does provide an immediate image in real space without employing any structural assumptions. This image is correct as far as it goes: that is, only structures consistent with it are permissible.

Multiple-wavenumber photoelectron holograms will be mentioned briefly, although a complete discussion is beyond the scope of this work. Variation of the photon energy permits the observation of a series of holograms for different k-values (i.e., over the surfaces of hemispheres of different radius in momentum space). In this way k-space can be filled, sampling all photoelectron energies in all directions, forming a collection which shall be referred to as a "complete" photoelectron diffraction data set. All experimental photoelectron diffraction experiments reported to date have employed subsets of the complete data set. That they have yielded so much information is strong evidence for the intrinsic value of the method. Transformation of the complete data set would yield a real space image which, if free from distortions due to phase shifts, etc., would provide a complete structure with accurate distances. Alternatively, an ARPEFS, or swept-energy, curve can be generated by collecting photoelectrons at one angle while varying the photon energy: thus the magnitude k, but not the direction, of the momentum is varied. By itself, the ARPEFS method is quite complementary to the present work: ARPEFS data can yield

very accurate information about interatomic distances and they are, alternatively, amenable to (1D) Fourier transformation analyses to yield "fingerprints" of the local structure.

In the present experiment, the results show that this *single energy, substrate* experiment can be interpreted, without any other structural assumptions, to yield the local crystal structure of fcc platinum from a study of the Pt(111) face. To accomplish this, it was essential that the hologram be sensitive to atoms several atomic layers away, and strong signals were in fact registered from atoms in at least the fourth atomic layer from the surface. Because forward scattering amplitudes dominate over those due to backscattering in this energy range, forward scattering atoms lying between the emitter and detector were preferentially illuminated. While imaging the near-surface atoms of a well characterized structure is by itself of little value, it serves as an important demonstration of the extended range capability of the technique. Interface studies are clearly possible with this method.

Unlike some photoelectron holography experiments, there is no serious artifact problem in these results. The twin images are well understood, and in Chapter 3 it is shown how they may be eliminated [25]. Elongation of the atomic images in the z-direction is expected, as a simple diffraction limit imposed in that direction by the geometry of the collection angle, combined with a single photon energy. We note that the resolution in the x and y directions is excellent, because of the high sampling density and fairly large sampling range in k_x and k_y. It is particularly gratifying that the x and y positions of neighboring atoms for several atomic layers are accurate to within 0.1 Å or better, however, there is evidence that 0.1Å is better than one expects from this level of analysis.

The use of lower-energy electrons in this work was very important. The more isotropic scattering experienced by low-energy electrons, relative to ca 1 keV electrons, permits good imaging of both the emitter layer and, in the same data set, atoms up to 3-4 layers away. This result is in agreement with previous ARPEFS work which has shown high path-length sensitivity in the range from $|k| = 5$ to 12 $Å^{-1}$ [20, 28]. At higher energies Debye-Waller damping decreases signal-to-noise and forward-scattering becomes

appreciable. Zero-order "forward scattering" features do not contain any holographic structural information per se, although higher frequency interference oscillations may reside on the peak's fringe [12].

Disadvantages of using lower-energy electrons include the intrinsically lower spatial resolution accompanying longer electron wavelengths and the increase of multiple scattering effects at lower energies, which can potentially cause problems for single-energy studies. The relative importance of these advantages and disadvantages must be assessed in detail by further work. The tentative conclusion from this study is that the advantages outweigh the disadvantages for electron energies in the few-hundred eV range: the spatial resolution is adequate for structural studies, the wide angular range of scattering is very helpful, and multiple scattering effects are not strongly evident.

Finally, the display analyzer was very important in this study, affording rapid and straightforward measurements of holograms. Especially helpful was the large solid angle, which permitted the excellent spatial resolution in the *x*-*y* planes.

In conclusion, these data demonstrate the practical potential of photoelectron holography for determining atomic structures in ordered crystals to a depth of at least four atomic layers, free of some of the artifacts of early photoelectron holography work. Key to this result are the combination of a large solid-angle analyzer and the use of relatively low-energy photoelectrons. This work demonstrates the practical application of using photoelectron holography to determine the atomic structure of ordered interfaces. The bulk of this work has been published previously in Reference 29.

References

[1] A. Szöke, in *Short Wavelength Coherent Radiation: Generation and Applications*, edited by D.T. Atwood and J. Bokor (AIP Conf. Proc. 146, New York, 1986).

[2] J.J. Barton, Phys. Rev. Lett. 61 (1988) 1356.

[3] G.R. Harp, D.K. Saldin and B.P. Tonner, Phys. Rev. Lett. 65 (1990) 1012.

[4] G.R. Harp, D.K. Saldin and B.P. Tonner, Phys. Rev. B. 42 (1990) 9199.

[5] Z.L. Han, S. Hardcastle, G.R. Harp, H. Li, X.D. Wang, J. Zhang and B.P. Tonner, Surf. Sci. 258 (1991) 313.

[6] P. Hu and D.A. King, Nature 353 (1991) 831.

[7] G.S. Herman, S. Thevuthasan, T.T. Tran, Y.J. Kim and C.S. Fadley, Phys. Rev. Lett. 68 (1992) 650.

[8] S. Thevuthasan, R.X. Ynzunza, E.D. Tober and C.S. Fadley, Phys. Rev. Lett. 70 (1993) 595.

[9] L.J. Terminello, J.J. Barton and D.A. Lapiano-Smith, Phys. Rev. Lett. 70 (1993) 599; J. Vac. Sci. Technol. B 10 (1992) 2088.

[10] B. P. Tonner, Z.L. Han, G.R. Harp and D.K. Saldin, Phys. Rev. B 43 (1991) 14423.

[11] S.Y. Tong, C. Wei, T. Zhao, H. Huang and H. Li, Phys. Rev. Lett. 66 (1991) 60.

[12] S. Thevuthasan, G.S. Herman, A.P. Kaduwela, R.S. Saiki, Y.J. Kim, W. Niemczura, M. Burger and C.S. Fadley, Phys. Rev. Lett. 67 (1991) 469.

[13] S. Hardcastle, Z.-L. Han, G.R. Harp, J. Zhang, B.L. Chen, D.K. Saldin and B.P. Tonner, Surf. Sci. Lett. 245 (1991) L190.

[14] D.K. Saldin, G.R. Harp, B.L. Chen and B.P. Tonner, Phys. Rev. B 44 (1991) 2480.

[15] G.R. Harp, D.K. Saldin, X. Chen, Z.-L. Han and B.P Tonner, J. Electr. Spectros. Relat. Phenom. 57 (1991) 331.

[16] H. Huang, H. Li and S.Y. Tong, Phys. Rev. B 44 (1990) 3240.

[17] J.J. Barton, Phys. Rev. Lett. 67 (1991) 3106.

[18] A.Stuck, D. Naumović, H.A. Aebischer, T. Greber, J.Osterwalder and L. Schlapbach, Surf. Sci. 264 (1992) 380; Surf. Sci. 274 (1992) 441.

[19] R. Dippel, D.P. Woodruff, X.-M. Hu, M.C. Asensio, A.W. Robinson, K.-M. Schindler, K.-U. Weiss, P. Gardner and A.M. Bradshaw, Phys. Rev. Lett. 68 (1992) 1543.

[20] L.-Q. Wang, A.E. Schach von Wittenau, Z.G. Ji, L.S. Wang, Z.Q. Huang and D.A. Shirley, Phys. Rev. B. 45 (1992) 13614.

[21] A.E. Schach von Wittenau, Z. Hussain, L.-Q. Wang, Z.Q. Huang, Z.G. Li and D.A. Shirley, Phys. Rev. B. 45 (1992) 13614.

[22] J.J. Barton, C.C. Bahr, S.W. Robey, Z. Hussain, E. Umbach and D.A.Shirley, Phys. Rev. B 34 (1986) 3807.

[23] D.E. Eastman, J.J. Donelon, N.C. Hien and F.J. Himpsel, Nucl. Instrum. Methods 172 (1980) 327.

[24] F.J. Himpsel, Y. Jugnet, D.E. Eastman, J.J. Donelon, D. Grimm, G. Landgren, A. Marx, J.F. Morar, C. Oden, R.A. Pollack, J.Schneir and C. Crider, Nucl. Instrum. Methods Phys. Res. 222 (1984) 107.

[25] B.L. Petersen, L.J. Terminello, J.J. Barton and D.A. Shirley (to be published).

[26] J.J. Barton, C.C. Bahr, Z. Hussain, S.W. Robey, J.G. Tobin, L.E. Klebanoff and D. A. Shirley, Phys. Rev. Lett. 51 (1983) 272.

[27] J.J. Barton, J. Electron Spectrosc. 51 (1990) 37.

[28] L.J. Terminello, X.S. Zhang, Z.Q. Huang, S. Kim, A.E. Schach von Wittenau, K.T. Leung and D.A. Shirley, Phys. Rev. B. 38 (1988) 3879.

[29] B.L. Petersen, L.J. Terminello, J.J. Barton and D.A. Shirley, Chem. Phys. Lett. 213 (1993) 412.

Figure Captions

Figure 2.1. *Experimental $\chi(k_x, k_y)$ pattern and two-dimensional analysis.* Panel (a) shows the symmetry-averaged platinum $4f_{5/2}$ data of electron intensity, taken with a kinetic energy of 351 eV, after background removal and Fourier filtering. Panel (c) shows the ABCA... fcc crystal stacking pattern of platinum with x-y slices taken through the first and third layers above the emitter, the results of which are shown in panels (c), taken at z = 2.2Å, and (d), taken at z = 6.7Å above the emitter in the experimental data set. Crosses mark the expected bulk lattice positions for platinum.

Figure 2.2. *Three-dimensional volume views from above.* a) Unaveraged and b) symmetry averaged iso-density real space intensity plots of the most intense features in the three-dimensional transformed Pt $4f_{5/2}$ 351 eV data set, looking normal to the (111) surface. Atoms are shaded darker with increasing distance from the top. These images may be compared to the ideal version shown in panel (c), in which positions of the emitter layer atoms and the central atom three layers above are shown in black, those one layer above are grey, and those two layers above are white.

Figure 2.3. *Three-dimensional volume side views.* These are iso-density real space three-dimensional images taken from the side of the reconstructed rotationally symmetry-averaged Pt $4f_{5/2}$ 351 eV data set compared with ideal versions. Panel (a) shows the different atoms, while (b), rotated ~30° from (a) along the Z-axis, sacrifices some of the vertical atomic distinction to show the layering of the planes. The mesh plane separates real from twin images, and the ellipsoidal shapes of the images result from the diffraction limit of this particular experiment.

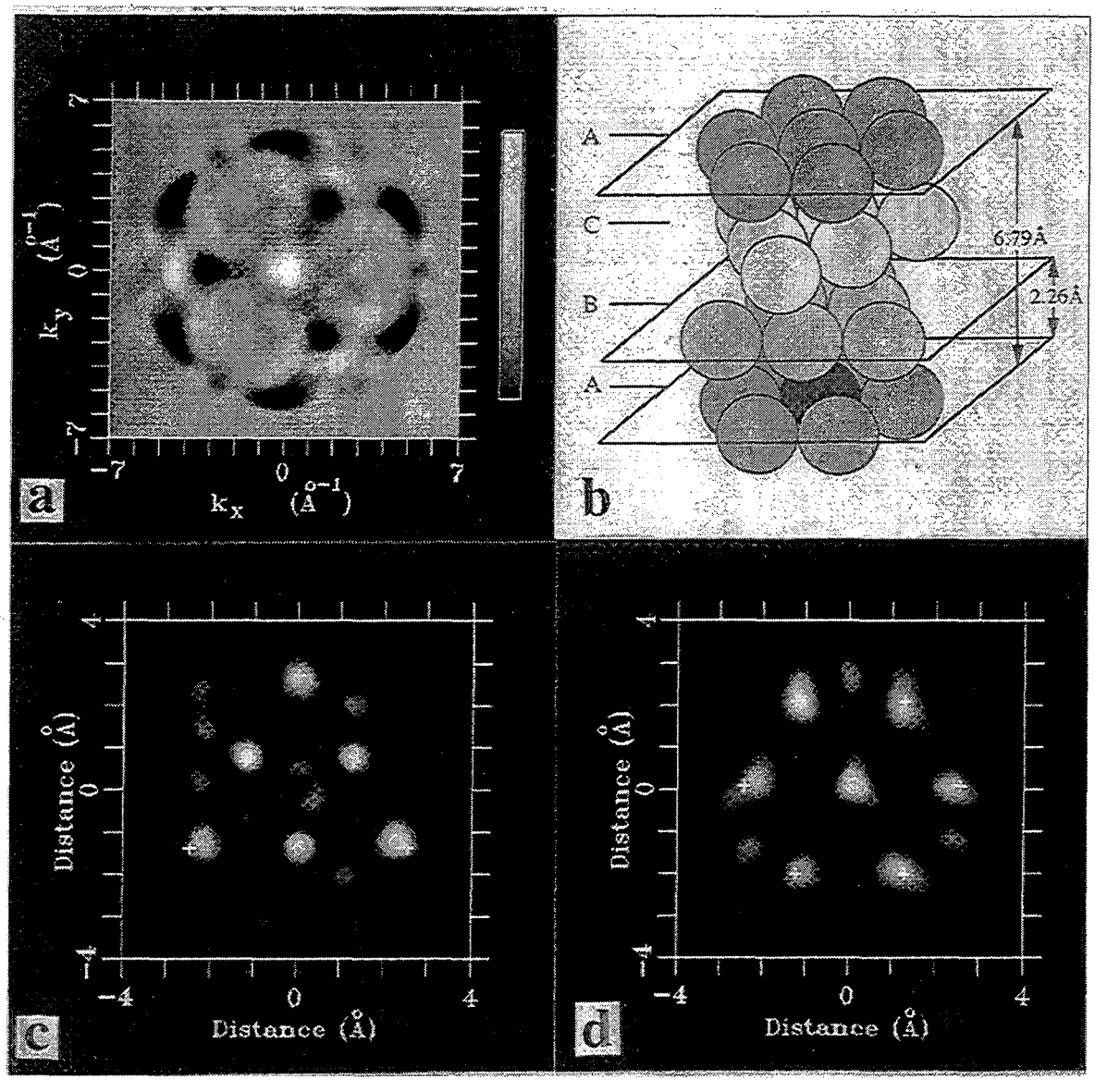
a
b
c
d
A
C
B
A
6.79Å
2.26Å
k_y (Å^{-1})
k_x (Å^{-1})
Distance (Å)
Distance (Å)
Distance (Å)
Distance (Å)

Figure 2.1

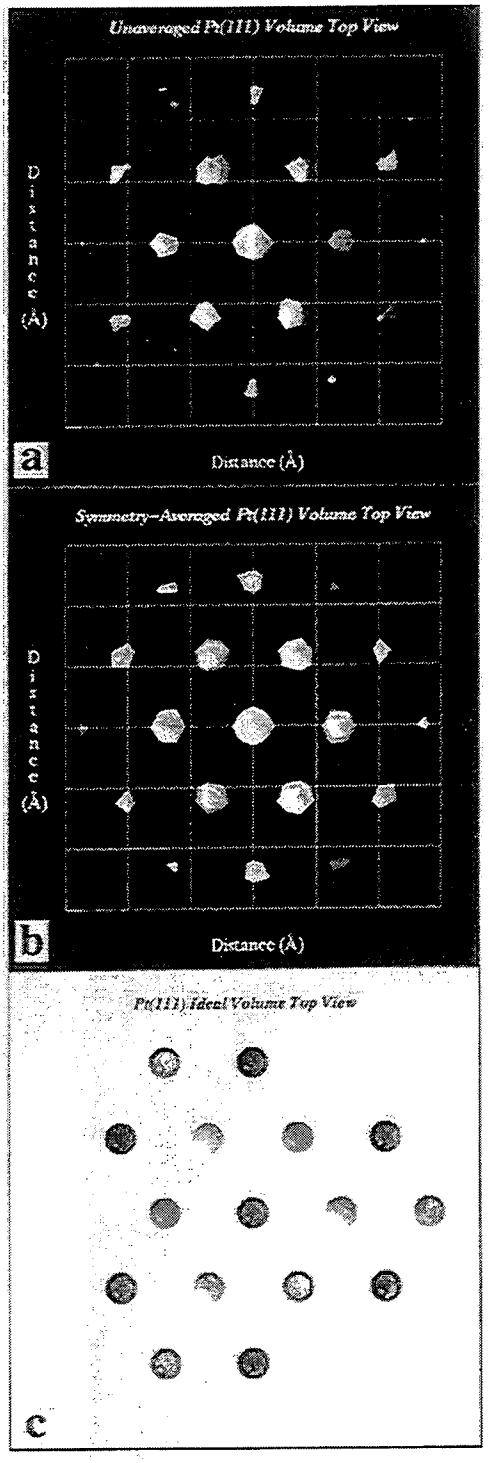
Unaveraged Pt(111) Volume Top View
Distance (Å)
Distance (Å)
a
Symmetry-Averaged Pt(111) Volume Top View
Distance (Å)
Distance (Å)
b
Pt(111) Ideal Volume Top View
c

Figure 2.2

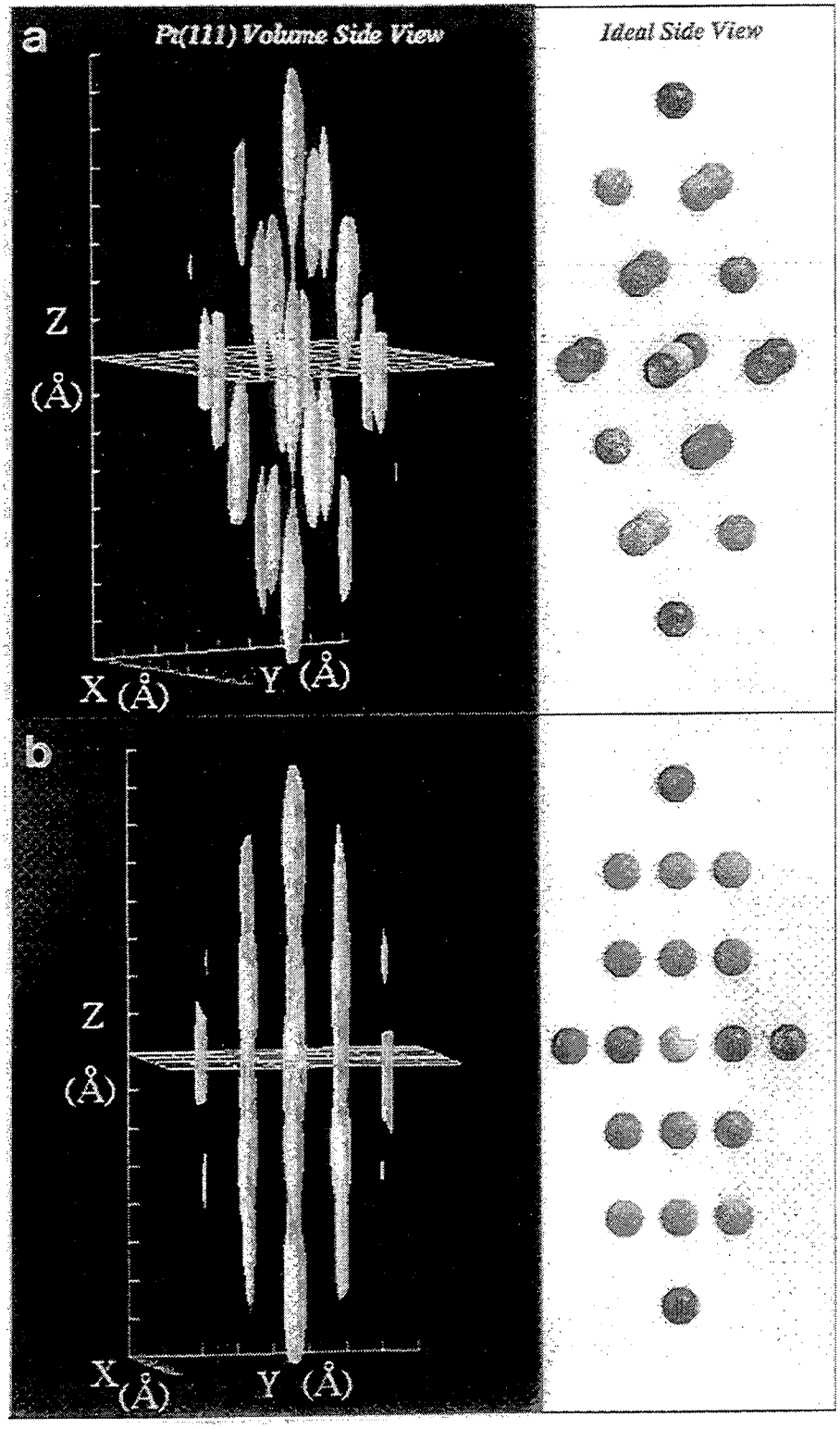

Figure 2.3

Chapter 3

MULTIPLE-WAVENUMBER PHOTOELECTRON HOLOGRAPHY OF PT(111)

Abstract: A multiple-wavenumber photoelectron holographic study of a Pt(111) surface, based on the $4f_{5/2}$ peak, demonstrates the capability of imaging atomic positions up to three layers above the emitter, with twin images removed by phase-summing over the carefully-selected wavenumber range k = 8.8 - 10.2 $Å^{-1}$. Photoelectron holography based on synchrotron radiation and *forward* scattering should be directly applicable to surface and near-surface interface systems.

I. Introduction

Photoelectron holography was described by Szöke [1] and Barton [2] as a direct method for obtaining three-dimensional images of the local atomic structure around selected photoemitting atoms on, or within a few atomic layers of, a crystal surface. These real-space images are derived, through integral transformations, from the angular distributions of photoelectron intensity at particular kinetic energies which are chosen to select the atoms of interest. As in other forms of photoelectron spectroscopy, photoelectron holography is chemically specific. It requires a coherent superposition of photoelectron intensity patterns from source atoms, but does not require long-range order per se, in the sense of a large domain size. Structural information can be derived without employing iterative fitting or making structural assumptions. In applications to an unknown system, subject only the

requirement of an ordered substrate, photoelectron holography should be capable of determining the adsorbate overlayer structure through backscattering, or deeper surface and interface structure through forward scattering. The latter is emphasized in this chapter.

In the course of the development of the method, photoelectron holography has yielded promising experimental [3-11] and theoretical [12-19] results in spite of problem areas which include atom-image distortions, position shifts, low spatial resolution, and unphysical artifacts. Distortions and position inaccuracies have been successfully reduced using amplitude- and phase-compensation schemes which include terms in the transform that account for expected differences between derived atom images and known structures [12,13]. However, these corrections can only be semi-empirical, as they require prior knowledge of the system being studied, specifically the atom-dependent scattering factors. Alternatively, methods of window restriction require estimates of atomic positions [18]. Corrections of this nature, based on additional knowledge of the system, may reduce the applicability of the method to unknown systems.

Fourier-filtering techniques have diminished some of the often-dominant central artifacts arising from forward-scattering events [7,17], and false intensities at the origins of the transformed images have also been reduced by insuring that the pattern oscillates around zero prior to application of the integral transform [2]. Other unphysical intensities apparent in the transformed data sets, which result from twin images and spurious or multiple-scattering artifacts, can be reduced or eliminated by application of a multiple-wavenumber analysis scheme, as suggested by Barton [19] and shown to be feasible by Terminello and Barton in preliminary experiments [9]. In this scheme for improving the images, no additional information about the system is needed beyond the experimentally determined diffraction pattern and the measured electron kinetic energy.

In this chapter the ability of holography to determine local surface structure directly is further evaluated, by applying a multiple-wavenumber analysis to Pt($4f_{5/2}$) photoelectron data obtained from a Pt (111) single-crystal face. By establishing the quality of images

measured at each of several single wavenumbers, and selecting an appropriate energy range, it was possible to achieve a significant reduction of the twin images apparent in a single-wavenumber study. In addition, a longer field of view was achieved with this system compared to previous studies with copper [9]. It was also possible to compare the images obtained with and without symmetry averaging. The derived real-space images allowed an assessment of the effects of phase shifts and polarization, establishing a firmer basis for application of holography to unknown systems.

II. Experimental

The (111) face of a Pt single crystal, characterized by LEED and oriented by Laue diffraction, was sputtered for one hour in argon at a pressure of 10^{-5} torr, followed by resistive annealing at 850° C for three minutes. This produced a clean surface, as determined by XPS. An energy-selective ellipsoidal mirror analyzer [20] was used for all spectra taken in this study, which was conducted on the IBM U8 beam line [21] at the National Synchrotron Light Source. Orientation of the crystal with respect to the analyzer was established by measuring valence-band photoemission features. The detector consisted of a video camera arranged behind microchannel plates and a phosphor screen, collecting data at a rate of 30 frames per second in a 512 x 512 pixel array. The angular acceptance of the analyzer was ca. 84°, with a typical energy resolution of 0.3 eV and angular resolution of 1/4°. Radiation in the range 200-600 eV from the U8 monochromator was used in this work.

The intensity of the Pt $4f_{5/2}$ electron peak was measured for each photon energy selected. Electron intensity at kinetic energies just above the peak energy was used for background normalization and correction for the analyzer throughput, or "signature" function. Nine patterns from k = 7.8 to 12.0 $Å^{-1}$ with wavenumber separation 0.6 $Å^{-1}$ were taken in the first run. The sample was then removed, cleaned, and returned to the same position, where 24 additional patterns were measured, yielding a total of 33 patterns

with wave numbers through the range 6 - 12 $Å^{-1}$, spaced by 0.2 $Å^{-1}$. Typical measurement times were 1 hour for the photopeak and 2 hours for the background. Later analysis showed the background patterns to be essentially interchangeable, potentially reducing the measurement time considerably.

III. Data Analysis

Of all the information collected in the electron intensity distribution patterns, only the intensity variation resulting from interference between the source and primary scattered waves is useful for holographic reconstruction of the local atomic structure around the source atom. The first objective in data reduction is therefore to isolate the interference pattern to the extent feasible, given that the rest of the signal can lead to artifacts. Various data extraction processes have been described previously [11]: they include background removal in conjunction with analyzer "signature" corrections, angular- to momentum-space mapping with optional analyzer angular corrections, Fourier filtration (or application of a low-pass filter) for removal of broad diffraction features, and finally, circular trimming of the pattern edges to reduce edge-effect artifacts from the preceding division (reducing "Fourier ringing"). All of these processes were non-invasive, as they only reduced undesirable artifact-producing features while adding no new artifacts. The resulting two-dimensional intensity patterns in *k*-space were used for the holographic inversions.

Real-space images were obtained from these reduced two-dimensional *k*-space $\chi(k)$ patterns of NxN points by multiplying them by a phasing term (to select the appropriate position in z) and then applying a two-dimensional image integral transform, digitized for use according to:

$$U_{p,q}(z) = \frac{4}{N^2} e^{-i\pi p - i\pi q} \sum_{m=0}^{N-1} \sum_{n=0}^{N-1} \chi_{m,n} e^{ikz\sqrt{1-k_x(n)-k_y(m)}} e^{i2\pi qm/N} e^{i2\pi pn/N} \quad (1)$$

where p and q are lateral x and y indices in the image [22]. This transformation yields a two-dimensional real-space slice of intensity at the selected z position. The most intense features in these slices should be centered around the x, y coordinates of atomic positions. Three-dimensional images can be constructed by stacking the slices taken at appropriate step sizes, to form a volume set. This procedure has been used to analyze data taken at a single wavenumber, giving excellent results at $k = 9.6$ Å^{-1} (351 eV) [11].

In the present work, a multiple-wavenumber analysis method has been employed to reduce multiple-scattering artifacts and twin images. Transformed images, obtained from electron intensity patterns taken with varying kinetic energies, were combined. By thus effectively stepping through k_Z as well as k_X and k_Y, it was possible to approximate a complete three-dimensional image integral transformation, expressed as:

$$M(\vec{r}) = \sum_i F_i(k_i, \chi_i, \vec{r}) e^{-ik_i\vec{r}} \qquad (2)$$

which is a sum over each image reconstruction, $F_i(k_i, \chi_i, \vec{r})$, computed from the individual patterns $\chi(k_i)$ measured at wave vector k_i, multiplied by $\exp(-ik_i\vec{r})$, the phase term that draws out the real, single-scattering contribution to the reconstruction as outlined in reference 19. After proper phasing and summation of the complex real-space intensities of single-wavenumber patterns transformed to a common three-dimensional real space, the absolute square of the resulting wave field was taken. As the peak intensities formed by integrating over angle and those created by summing over wavenumber did not coincide, this procedure suppressed multiple scattering, twin images, and most of the self-interference terms. In this way, some of the problems associated with single-wavenumber reconstruction were either eliminated or greatly reduced.

IV. Results

Of the 33 interference patterns measured over a k range of 6 - 12 $Å^{-1}$, only eight were selected, spanning the range k = 8.8 - 10.2 $Å^{-1}$, for the analysis presented below. Inclusion of the patterns collected at kinetic energies much below ca. 300 eV added little or no improvement to the final reconstructed images. This is attributed to a decrease in forward scattering at these low energies [23], and the lower spatial resolution associated with lower-energy electrons. Patterns collected with electron kinetic energies much above 400 eV had unacceptable signal/noise ratios after data reduction, because of lower photon fluxes at these higher energies on this particular beamline. Again, inclusion of these higher-energy patterns did not improve the apparent quality of the final summed image. The decision to use only the higher quality patterns over the middle of the energy range was based on the observation that these patterns suffice to demonstrate the effectiveness of the multiple-k algorithm, and the fact that adding poorer-quality patterns at either end would give an inaccurate impression of the quality of image that could be recovered if higher-quality data were collected throughout the range. Such an experiment should be easily feasible with a better photon source.

Figure 3.1 shows a representative sample (3 of 8) of the electron angular intensity patterns used in the reconstruction, taken at k = 9.0, 9.8, and 10.2 $Å^{-1}$, respectively (kinetic energies of 309, 366, and 396 eV), shown in panels A, C, and E. These patterns have been three-fold rotationally symmetry-averaged; a less distinctive threefold pattern was evident before averaging. Opposite each intensity pattern is the corresponding real-space x-y slice evaluated at z = 2.26 Å (panels B, D, and F), in which the most intense features represent the (centroids of) positions of nearest neighbor atoms in the planes directly above the source atoms. The features are not atomic "images" per se; they represent the location of the scattering center. Each panel shows three bright features at approximately the same positions, as expected, representing the only three atoms in this

layer that stand out above the background noise. The relatively small variation in their positions in the three panels is attributed to atomic scattering phase shifts [2].

Three-dimensional iso-density real-space volumes of the reconstructed images are shown in Figure 3.2. Panel 3.2A depicts the image obtained from an averaged pattern taken at 366 eV, cut off at 30% of the highest intensity, with twin images below the mesh plane of the emitter. Moving up from the emitter, three atoms positions are recorded in the plane directly above, three in the next layer, and one three layers directly above, consistent with the abca... pattern of the fcc lattice along [111]. The twin images are suppressed in panel 3.2B, which shows the eight-wavenumber phase-summed image, also at 30% of the highest intensity. Panel 3.2C shows the image obtained from non-symmetry-averaged patterns, at 50% of the highest intensity. One atom in the second layer above the emitter is missing altogether at this intensity cutoff, and another is very weak, because of the electron angular distribution, which is peaked along the photon electric vector, 45° from the surface normal. This effect leads to the weak second-layer intensities in the averaged pattern, 3.2B, and serves to highlight that these intensities only indicate atomic positions (at or near their centroids) rather than imaging the whole atoms. Intensities at the source-atom position arise from residual DC noise of the reduced data set. Panel 3.2D shows a model image of the same system which may be compared to the other images.

For the multiple-wavenumber image of Figure 3.2B, the pixel resolution was 0.26 Å along the x-y direction and 0.28 Å along the z direction. The standard deviations of atom centroid positions was ± 0.3 Å with FWHM = 0.7 ± 0.1 Å in the x and y directions and ± 1.5 Å with FWHM = 3.6 ± 0.2 Å in the z direction, as compared to the average diffraction limited theoretical values of $\Delta x,y = 0.7$ Å and $\Delta z = 3.3$ Å [22]. The standard deviation of the radial positions of the centroids of the atoms from their bulk lattice positions was ± 0.3 Å. Twin images were suppressed to 10% of their corresponding real image intensity in this example.

V. Discussion

This experiment required an efficient means of data acquisition, synchrotron radiation, and a carefully selected range of photoelectron energy. The two-dimensional analyzer facilitated rapid collection of the intensity patterns over a wide angular range with good angular resolution and at selected energies. The 300-500 eV energy range was high enough to provide good overall position resolution while utilizing stronger forward scattering and good oscillatory amplitude at slightly higher energies without strong scattering features which could dominate the transforms if not adequately removed. Synchrotron radiation provides the capability to select the energy range, which appears to hold real advantages.

The earlier single-wavenumber study of this system in Chapter 2 established that the local atomic structure can be deduced from an intensity pattern measured at only one kinetic energy [11]. However, multiple-energy data can be used to suppress the twin images, leaving no doubt about the true structure. Phase-summing also reduces multiple-scattering and other spurious artifacts that commonly arise in single-wavenumber measurements. The z resolution, limited by the experimental geometry and inherent scattering factor distortions, can potentially be improved as $\Delta r = 2\pi/\Delta k$ by phase-summing in some cases where the analyzer opening angle is less than π [19]. Because the Δk spanned in the present experiment was only 1.4 $Å^{-1}$, the resolution in the direction normal to the crystal surface did not improve beyond the diffraction limited value of about 3 Å set by the opening angle [22]. However, by including holograms from a wider range in *k*-space, the resolution could improve beyond this limit. Patterns could also, of course, be collected over a larger opening angle, thereby improving the diffraction limit of the experiment and the corresponding z resolution.

In this work, position displacements were attributed to scattering phase shifts, which were not considered in the analysis. Small shifts are expected with this method, along with scattering factor distortions and effects arising from the light polarization, but

none of these factors should limit the application of this technique in this energy range. The images obtained should suffice to determine an atom's bonding configuration without other structural or chemical input.

VI. Conclusions

Using a Pt (111) surface as a test case, it has been shown that artifact-free three-dimensional images which qualitatively agree with the known crystal structure can be obtained *directly* from experimental photoelectron intensity patterns. Phase-summing over eight intensity patterns through a range of k = 8.8 - 10.2 $Å^{-1}$ has yielded a substantial reduction in conjugate image intensity relative to images taken at single wavenumbers. False intensities from multiple scattering and transform artifacts were also reduced in the process. With careful data reduction of individual holograms and the selection of an appropriate energy range, locations of atoms beyond nearest neighbors were obtained without extensive distortions. Of major importance, this approach to photoelectron holography is based on *forward* scattering, and is thus applicable to interface and deep-surface systems, not just the first layer or two. When applied in a suitable way to unknown bulk, adsorbate, or interfacial systems, it should be capable of elucidating local atomic structure directly. The bulk of this work was previously reported in Reference 24.

References

[1] A. Szöke, in *Short Wavelength Coherent Radiation: Generation and Applications*, edited by D.T. Atwood and J. Bokor (AIP Conf. Proc. 146, New York, 1986).

[2] J.J. Barton, Phys. Rev. Lett. 61 (1988) 1356.

[3] G.R. Harp, D.K. Saldin and B.P. Tonner, Phys. Rev. Lett. 65 (1990) 1012.

[4] G.R. Harp, D.K. Saldin and B.P. Tonner, Phys. Rev. B. 42 (1990) 9199.

[5] Z.L. Han, S. Hardcastle, G.R. Harp, H. Li, X.D. Wang, J. Zhang and B.P. Tonner, Surf. Sci. 258 (1991) 313.

[6] P. Hu and D.A. King, Nature 353 (1991) 831.

[7] G.S. Herman, S. Thevuthasan, T.T. Tran, Y.J. Kim and C.S. Fadley, Phys. Rev. Lett. 68 (1992) 650.

[8] S. Thevuthasan, R.X. Ynzunza, E.D. Tober and C.S. Fadley, Phys. Rev. Lett. 70 (1993) 595.

[9] L.J. Terminello, J.J. Barton and D.A. Lapiano-Smith, Phys. Rev. Lett. 70 (1993) 599; J. Vac. Sci. Technol. B 10 (1992) 2088.

[10] H. Li, S.Y. Tong, D. Naumovic, A. Stuck, and J. Osterwalder, Phys. Rev. B. 47 (1993) 10036.

[11] B.L. Petersen, L.J. Terminello, J.J. Barton and D.A. Shirley, Chem. Phys. Lett. 213 (1993) 412. (See Chapter 2)

[12] B. P. Tonner, Z.L. Han, G.R. Harp and D.K. Saldin, Phys. Rev. B 43 (1991) 14423.

[13] S.Y. Tong, C.M. Wei, T.C. Zhao, H. Huang and H. Li, Phys. Rev. Lett. 66 (1991) 60.

[14] S. Thevuthasan, G.S. Herman, A.P. Kaduwela, R.S. Saiki, Y.J. Kim, W. Niemczura, M. Burger and C.S. Fadley, Phys. Rev. Lett. 67 (1991) 469.

[15] S. Hardcastle, Z.-L. Han, G.R. Harp, J. Zhang, B.L. Chen, D.K. Saldin and B.P. Tonner, Surf. Sci. Lett. 245 (1991) L190.

[16] D.K. Saldin, G.R. Harp, B.L. Chen and B.P. Tonner, Phys. Rev. B 44 (1991) 2480.

[17] G.R. Harp, D.K. Saldin, X. Chen, Z.-L. Han and B.P Tonner, J. Electr. Spectros. Relat. Phenom. 57 (1991) 331.

[18] H. Huang, H. Li and S.Y. Tong, Phys. Rev. B 44 (1990) 3240.

[19] J.J. Barton, Phys. Rev. Lett. 67 (1991) 3106.

[20] D.E. Eastman, J.J. Donelon, N.C. Hien and F.J. Himpsel, Nucl. Instrum. Methods 172 (1980) 327.

[21] F.J. Himpsel, Y. Jugnet, D.E. Eastman, J.J. Donelon, D. Grimm, G. Landgren, A. Marx, J.F. Morar, C. Oden, R.A. Pollack, J.Schneir and C. Crider, Nucl. Instrum. Methods Phys. Res. 222 (1984) 107.

[22] J.J. Barton, J. Electron Spectrosc. 51 (1990) 37.

[23] D.J. Friedman and C.S. Fadley, J. Electron Spectrosc. Relat. Phenom. 51 (1990) 689.

[24] B.L. Petersen, L.J. Terminello, J.J. Barton and D.A. Shirley, Chem. Phys Lett 220 (1994) 46.

Figure Captions

Figure 3.1. *Comparison of single-wavenumber $\chi(k_x, k_y)$ patterns and corresponding real space x-y slices.* Panels A, C, and E show symmetry-averaged emission patterns of platinum $4f_{5/2}$ photoelectron intensity after background removal and Fourier filtering, measured at k = 9.0, 9.8, and 10.2 $Å^{-1}$ (309, 366, and 396 eV), respectively. Opposite, panels B, D, and F show the corresponding real-space x-y slices taken from each through z = 2.26 Å, the position of the three nearest neighbors directly above the emitter. The real space images have been squared to highlight atom locations. The bulk distance between adjacent atoms in this layer is 2.77 Å. On the left, the scale represents 2.5 $Å^{-1}$ per division, and on the right, 1 Å per division.

Figure 3.2. *Reduction of conjugate images.* These are iso-density real space three-dimensional images showing side views of the reconstructed Pt $4f_{5/2}$ data sets. Panel (A) shows a volume-rendering of a symmetry-averaged transformed $\chi(k_x, k_y)$ pattern at k = 9.8 $Å^{-1}$ (366 eV), complete with equal-intensity conjugate images below the plane of the emitter, taken at 30% of the highest intensity. Panel (B) shows the result after phase-summing eight symmetry-averaged patterns with k = 8.8 to 10.2 $Å^{-1}$, with significant twin image reduction, also taken at 30% of the highest intensity. The same patterns, unaveraged for symmetry, produced panel (C), taken at 50% of the highest intensity. Panel (D) represents a model showing the same atoms as expected in bulk positions, included for comparison.

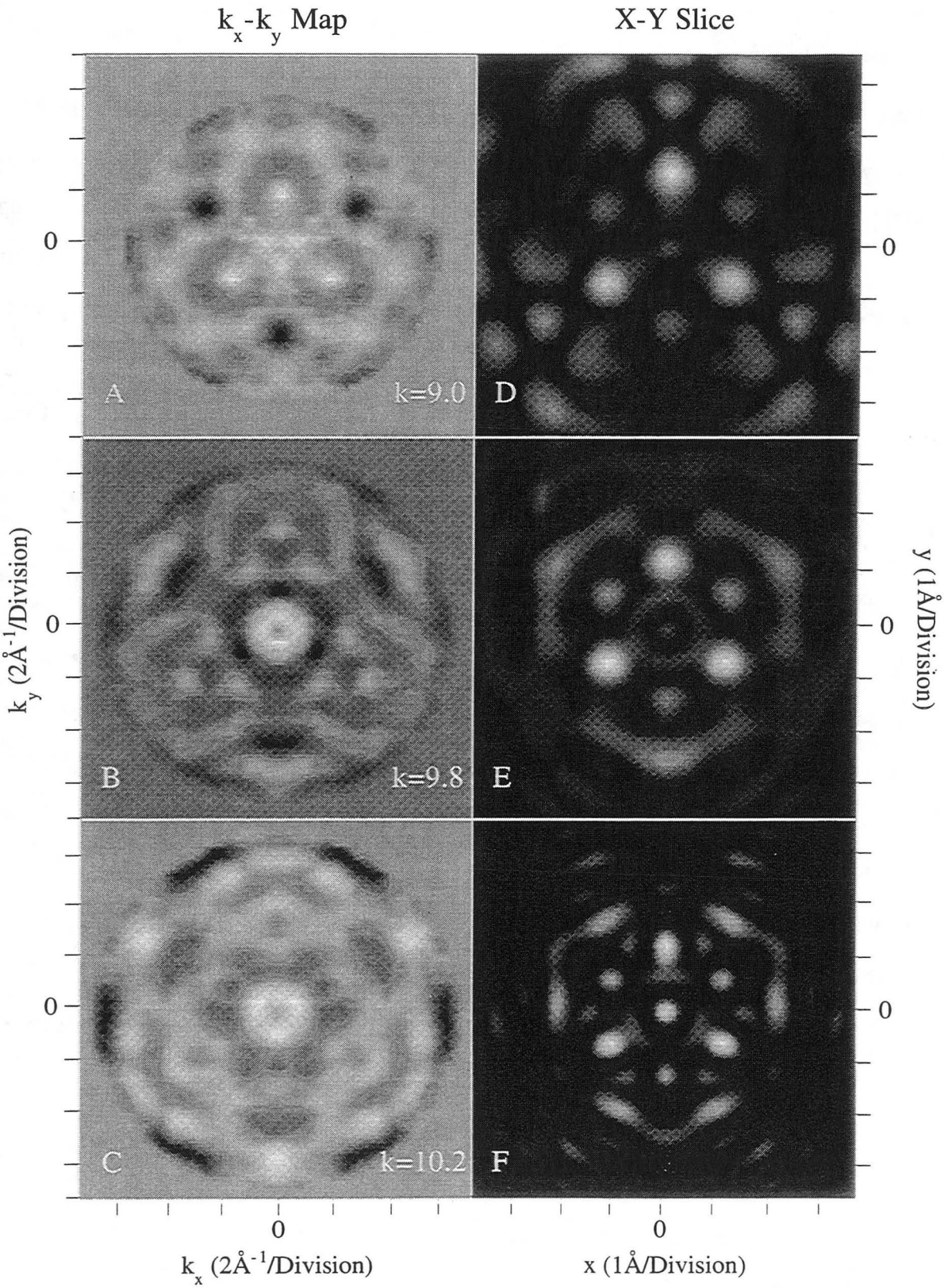
k_x-k_y Map
X-Y Slice
A
k=9.0
D
B
k=9.8
E
C
k=10.2
F
0
0
0
0
0
0
k_y (2Å^-1/Division)
y (1Å/Division)
k_x (2Å^-1/Division)
x (1Å/Division)

Figure 3.1

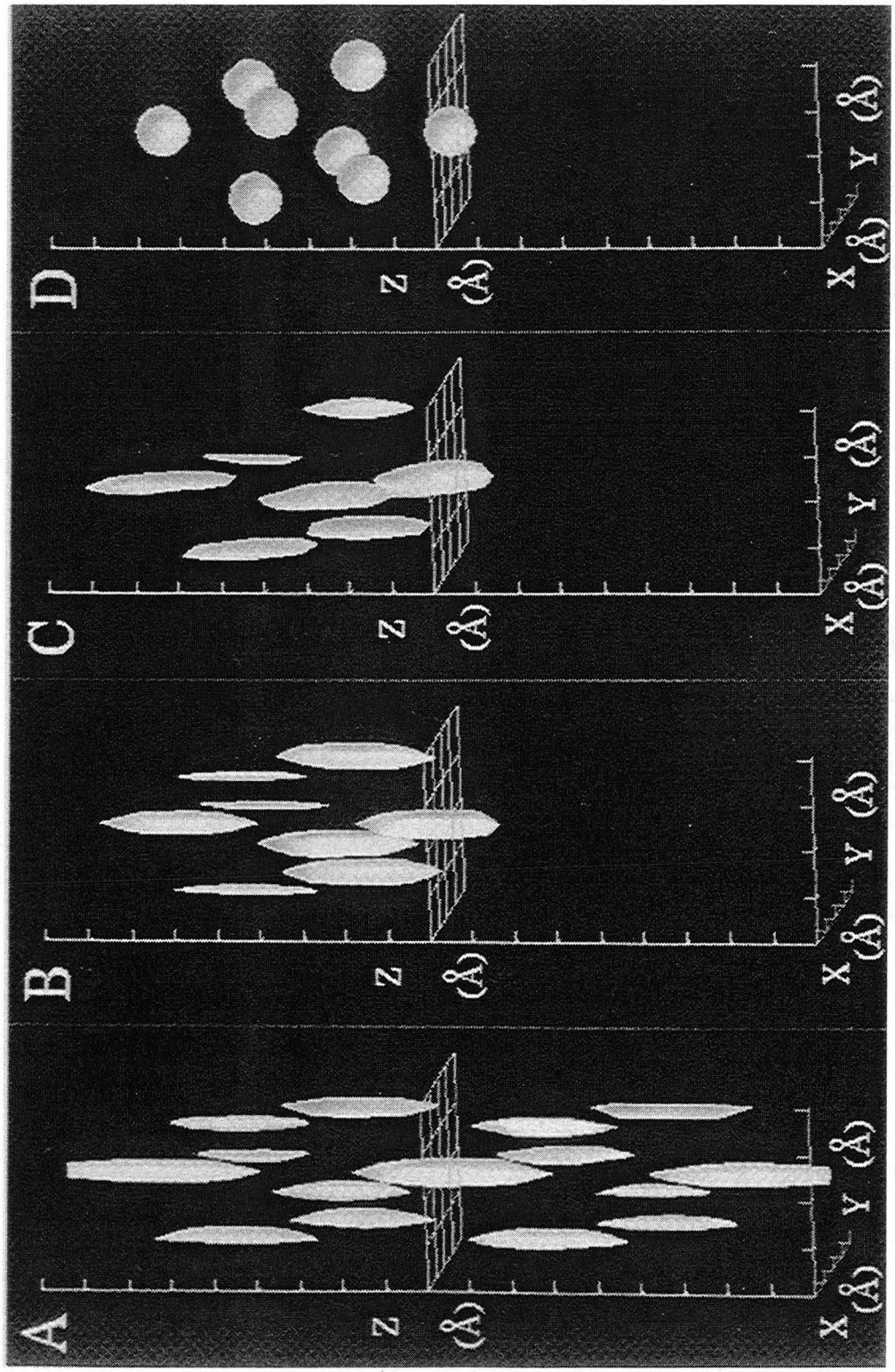

Figure 3.2

Chapter 4

ATOM INTENSITY VARIATION IN LOCALIZED-EMISSION ELECTRON HOLOGRAPHY

Abstract: A comparison of familiar slit-type interference with electron interference is used to explore the fundamental processes governing the interference process. Variation in intensity of atoms images resulting from holographic transformations of electron interference patterns measured at different wavenumbers is described as a result of cancellation of intensity in the measured interference pattern, independent of scattering factor or reference wave of the particular system studied. The cancellation is attributed to the imaging integral employed, which considers only a single emitter-scatterer event. A simple model of a forward scattering system is used to show how this geometry-related effect is manifested in the final result.

I. Introduction

Electron holography using localized emission, as suggested by Szöke [1] and formulated by Barton [2], has been presented as a direct method of obtaining three-dimensional surface structures through integral transformation of measured electron intensity maps. Experiments have been performed which have validated this premise [3-8], and suggest great promise for the future application of the technique. Nonetheless, some of these same experiments, and others employing this technique, have been plagued with inconsistencies and unverifiable results [9,10] which lower the confidence and the

reliability of such an experiment. If any form of localized-emission electron holography is to be used regularly for direct surface structural determination, it will be necessary to understand the fundamental processes in an interference experiment, and the relationship of electron holography to these processes.

A simple description of electron scattering in solids is as follows: an incident photon excites an electron in an atom into an outgoing electron wave, which then propagates to surrounding ion cores or out of the crystal. The atomic core potentials of the surrounding atoms scatter the wave, with a new propagation direction dependent on scattering factors and the phase and amplitude of the of the source wave. These scattered waves may scatter from other atoms, leading to the multiple scattering condition. The angle-dependent electron intensity pattern collected above the crystal results from the combination of the original and scattered electron waves at the detector.

The description above includes some of the main elements of the scattering physics which produce the structural information sought in a localized-emission electron holography experiment. However, not all of the recorded information is valuable for structural determination. Scattering factors also cause distortions and shifts of the centroids of atom intensity from their expected position [11]. The angular momentum character of the reference waves change the measured intensity patterns, both in terms of Legendre polynomial based distortion of separate interferences [12], or also in terms of a generalized modification of an s-wave by a centrifugal potential [13]. Additionally, multiple scattering can lead to unphysical artifacts [2]. Each element causes specific changes to the 'pure' interference pattern and, after application of the imaging integral, causes corresponding changes to the final result.

Fortunately, the problems caused by complex scattering factors may be diminished using algorithms that calculate and divide out generalized scattering factors (however this often requires prior knowledge of the system being studied) [14,15], or by using filtration techniques which reduce strong anisotropies in the diffraction pattern prior to

transformation [6,16]. One of these methods, employing a scattered-wave integral Fourier transform technique (SWIFT) [15], has also shown some success in removing reference wave effects in spherically symmetric emission [12]. Additionally, iterative applications of the SWIFT algorithm has show potential for improvement of patterns at a single wavenumber [17]. Multiple-scattering effects can be diminished by combining patterns measured at more than one wavenumber, which also helps reduce the confusing "twin" images [18]. The goal is to selectively remove the non-structural information from the patterns in order to obtain a more ideal hologram without affecting the original data.

If all of these corrections worked perfectly, we would be left with an ideal interference pattern resulting from an emitted isotropic l=0 spherical wave which scatters elastically off neighboring atoms that act as secondary origins of spherical waves. The original emitted wave would interfere with the scattered waves at the detector to give a final pattern consisting only of the structural information of the atoms around the emitter. Upon application of an image integral transformation to this ideal pattern, one should get an ideal real space image of the system under investigation.

In this chapter, we start with the premise of an ideal electron intensity pattern and show that under certain circumstances intensity variation of the atom images may be obtained even in the best cases of localized-emission electron holography due to primary scattered wave interferences. It is possible to understand the cause of these 'surprising' results from some of the fundamental principles of interference. Starting from the simplest case of two-slit interference (two point sources), we will explore the special condition of the emitter-scatterer wave interference. By adding a second scatterer to the system, we identify significant changes to the measured interferogram as compared to both the single-scatterer and the two- and three-slit interference cases. The changes to the pattern lead to predictable deviations from the expected transform result. As more scatterers are added to the system, such as in an actual experiment, the effect is compounded and the transforms are again not as we would expect or hope ideally. We give such an example, and then

proceed to suggest conditions which may minimize these effects. The goal is to understand how geometric considerations relate to the results obtained from localized-emission electron holography.

II. Comparison to Slit Interference

To better understand electron scattering in ordered solids, it is helpful to draw the analogy between electron interference and multiple-slit interference. The ideal electron two-slit problem can be represented as two point sources separated by a distance d which produce coherent electron waves independently as in Figure 4.1a, in which the point sources are shown as slits which are coherently illuminated. This is the same as having two displaced independent zero-order source waves. The waves meet in the far field region, where they are collected as an interference pattern. These waves may be expressed as:

$$\psi_0(\boldsymbol{R}) = \frac{e^{ikR}}{ikR} \qquad (1)$$

and

$$\psi_{0_d}(\boldsymbol{R}) = \frac{e^{i(kR+\phi)}}{ikR}, \qquad (2)$$

where the phase difference ϕ, which accounts for the extra distance the second wave must travel to get to the detector at some point P, can be written as $\phi = (2\pi/\lambda)d\sin\theta = kd\sin\theta$, where θ is the angle between the normal and $\boldsymbol{R}$, the vector from the emitter directly to the detector at P. This expression assumes the far field condition $R>>d$, where the emission vectors to the detector are essentially parallel, and in this sense Figure 4.1a may be somewhat misleading. The intensity at the detector for a given wavenumber will be given

as:

$$I_T(\boldsymbol{R}) = \left|\psi_0(\boldsymbol{R}) + \psi_{0_d}(\boldsymbol{R})\right|^2 = \psi_0^*\psi_0 + \psi_{0_d}^*\psi_0 + \psi_0^*\psi_{0_d} + \psi_{0_d}^*\psi_{0_d} \quad (3)$$

and the interference terms, $\chi(\boldsymbol{R})$, will be

$$\chi(\boldsymbol{R}) = \psi_{0_d}^*\psi_0 + \psi_0^*\psi_{0_d}, \quad (4)$$

$$= \frac{I_T(\boldsymbol{R}) - I_0(\boldsymbol{R}) - I_{0_d}(\boldsymbol{R})}{I_0(\boldsymbol{R})} \quad (5)$$

where we have used the convenient notation, $I_0(\boldsymbol{R}) = \psi_0^*\psi_0$ and $I_{0_d}(\boldsymbol{R}) = \psi_{0_d}^*\psi_{0_d}$, and this interference term reduces to:

$$\chi(\boldsymbol{R}) = 2\cos\phi, \quad (6)$$

which is the well known result of the two-slit problem. From this interference expression it can be seen that there will always be a maximum at $\theta = 0°$, and that changing the wavelength, or kinetic energy of the electrons, only has the effect of spreading the spacing of interference lines about the central peak. See Figures 4.2a and 4.2b, in which the left side shows χ as a function of angle, with the full 2π momentum space two-dimensional interference pattern shown on the right for direct comparison.

In the localized-emission electron interference case as depicted in Figure 4.1 panels (b) and (d), the complete scattering problem is divided into two parts [19]. The first portion is the zero-order dynamical problem, and the second represents the scattering from ion cores as a perturbation on the zero-order wave function. In the simplest l=0 spherical approximation, the zero-order source wave emanating from the emitting atom can be

considered to have the same form as in equation (1):

$$\psi_0(\boldsymbol{R}) = \frac{e^{ikR}}{ikR}. \tag{7}$$

The first order (single-scattered) wave function has $l=0$ spherical waves emanating from the ion core at $\boldsymbol{r}$:

$$\psi_1(\boldsymbol{R}) = \sum_{r_j} \frac{e^{ik|\boldsymbol{R}-\boldsymbol{r}_j|}}{ik|\boldsymbol{R}-\boldsymbol{r}_j|} \cdot \frac{e^{ikr_j}}{ikr_j}. \tag{8}$$

Expanding for $R>>r_j$ gives

$$|\boldsymbol{R}-\boldsymbol{r}_j| \approx R\left[1-\frac{r_j}{R}\cos\theta_{r_jR}+\ldots\right]$$

$$\approx R - r_j\cos\theta_{r_jR}, \tag{9}$$

and using this expression in (8),

$$\psi_1(\boldsymbol{R}) = \sum_{r_j} \frac{e^{ikR}}{ikR} \cdot \frac{e^{ikr_j(1-\cos\theta_{r_jR})}}{ikr_j}. \tag{10}$$

Equation (10) accounts for the phase and amplitude of the zero-order reference wave at the center of the scattering potential at r_j. The scattering factor, which gives the phase and amplitude of the scattered wave in the direction of the detector, has been intentionally neglected in this expression because we wish to observe unaffected spherical waves in order to isolate the geometric component. This would be equivalent to the type of

scattering which would be present in an *ideal* holography experiment.

For the two-atom case depicted in Figure 4.1 panel (a), we choose a single atom at $r_j = a$ to obtain:

$$\psi_{1_a}(\boldsymbol{R}) = \frac{e^{ikR}}{ikR} \cdot \frac{e^{ika(1-\cos\theta_{aR})}}{ika}. \qquad (11)$$

The total intensity in this case becomes

$$I_T(\boldsymbol{R}) = \left|\psi_0(\boldsymbol{R}) + \psi_{1_a}(\boldsymbol{R})\right|^2 = \psi_0^*\psi_0 + \psi_{1_a}^*\psi_0 + \psi_0^*\psi_{1_a} + \psi_{1_a}^*\psi_{1_a} \qquad (12)$$

and the corresponding interference, computed similarly to (5) is

$$\chi(\boldsymbol{R}) = \frac{2}{ka}\sin(ka(1-\cos\theta_{aR})). \qquad (13)$$

As can be seen in Figure 4.2 panels (c), (d), and (e), the effect of this type of scattering as compared to the two-slit example is that the interference pattern does not necessarily have to have a maximum at $\theta = 0°$ (Again, θ refers to the angle between the surface normal and $\boldsymbol{R}$). In fact, the maxima and minima vary with both k and a, with the maximum at $\theta = 0°$ occurring only when there is no phase difference at the detector between the two waves, when $k = (2n\text{-}1)\pi/2a$ (n is any integer). This means that for any emitter and a single scattering atom, the position of maxima and minima in the measured intensity pattern will change with energy for a fixed geometry, without a fiducial maximum at $\theta = 0°$.

Now we observe the effect of additional point sources. In the three-slit or three-atom case we can imagine three slits or atoms aligned in a plane perpendicular to the surface normal as shown in Figure 4.1, panels (c) and (d). The electron wave analog to the three-

slit problem, as shown in Figure 4.1 panel (c), is obtained using three equivalent zero-order spherical source waves with different origins and a corresponding phase difference:

$$\psi_0(\boldsymbol{R}) = \frac{e^{ikR}}{ikR}, \tag{14}$$

$$\psi_{0_d}(\boldsymbol{R}) = \frac{e^{i(kR+\phi_d)}}{ikR}, \tag{15}$$

and

$$\psi_{0_{-d}}(\boldsymbol{R}) = \frac{e^{i(kR+\phi_{-d})}}{ikR}. \tag{16}$$

The intensity at the detector is given by:

$$I_T(\boldsymbol{R}) = \left| \psi_0 + \psi_{0_d} + \psi_{0_{-d}} \right|^2$$

$$= \psi_0^* \psi_0 + \psi_{0_d}^* \psi_{0_d} + \psi_{0_{-d}}^* \psi_{0_{-d}}$$

$$+ \psi_{0_d}^* \psi_0 + \psi_0^* \psi_{0_d} + \psi_{0_{-d}}^* \psi_0 + \psi_0^* \psi_{0_{-d}} + \psi_{0_{-d}}^* \psi_{0_d} + \psi_{0_d}^* \psi_{0_{-d}} \tag{17}$$

and the interference terms reduce to:

$$\chi(\boldsymbol{R}) = 2\,(\cos\phi_d + \cos\phi_{-d} + \cos(\phi_d - \phi_{-d}))$$

$$= 4\cos\left(\frac{\phi_d + \phi_{-d}}{2}\right)\cos\left(\frac{\phi_d - \phi_{-d}}{2}\right) + 2\cos(\phi_d - \phi_{-d}) \tag{18}$$

where $\phi_d = kd\sin\theta$ and $\phi_{-d} = -kd\sin\theta$. This is essentially the result expected for a

diffraction grating, with the maxima of the two slit case intensified, again with the central maximum at θ=0° for all electron wavenumbers as shown in Figure 4.3, panels (a) and (b). Additionally, the last term in the expression above arises from the lower intensity two-slit result of the two coherent sources furthest apart.

In the case of three-atom electron interference, Figure 4.1d, there is again only one source wave, but now two first order single scattered waves at $\boldsymbol{r} = \pm\boldsymbol{a}$, given by:

$$\psi_0(\boldsymbol{R}) = \frac{e^{ikR}}{ikR}, \tag{19}$$

$$\psi_{1_a}(\boldsymbol{R}) = \frac{e^{ikR}}{ikR}\cdot\frac{e^{i\phi_a}}{ika}, \tag{20}$$

and

$$\psi_{1_{-a}}(\boldsymbol{R}) = \frac{e^{ikR}}{ikR}\cdot\frac{e^{i\phi_{-a}}}{ika} \tag{21}$$

where in this case, $\phi_a = ka(1-\cos\theta_{aR})$ and $\phi_{-a} = ka(1-\cos\theta_{-aR})$. The interference terms are similar to (17), given as:

$$I_T(\boldsymbol{R}) = \left| \psi_0 + \psi_{1_a} + \psi_{1_{-a}} \right|^2$$

$$= \psi_0^*\psi_0 + \psi_{1_a}^*\psi_{1_a} + \psi_{1_{-a}}^*\psi_{1_{-a}}$$

$$+\psi_{1_a}^*\psi_0 + \psi_0^*\psi_{1_a} + \psi_{1_{-a}}^*\psi_0 + \psi_0^*\psi_{1_{-a}} + \psi_{1_{-a}}^*\psi_{1_a} + \psi_{1_a}^*\psi_{1_{-a}} \tag{22}$$

and the corresponding interference terms are

$$\chi(\boldsymbol{R}) = \frac{2}{ka}(\sin\phi_a + \sin\phi_{-a}) + \frac{2}{k^2a^2}\cos(\phi_a - \phi_{-a})$$

$$= \frac{4}{ka}\left[\sin\left(\frac{\phi_a + \phi_{-a}}{2}\right)\cos\left(\frac{\phi_a - \phi_{-a}}{2}\right)\right] + \frac{2}{k^2a^2}\cos(\phi_a - \phi_{-a}). \quad (23)$$

This result is the same as the sum of two two-atom cases, or effectively two separate holograms, with an additional term for interaction of the two coherent scattering atoms. Each two-atom interference pattern changes independently with wavenumber and their sum gives the final result. At some wavenumbers complete constructive interference occurs, either with a maximum or minimum at $\theta = 0^\circ$ as shown in panels (c) and (e) of Figure 4.3, or complete destructive interference, leaving only the two-slit result from the two coherent atoms at $\boldsymbol{r} = \pm\boldsymbol{a}$, as in Figure 4.3d. The predictable wavenumbers of when this constructive or destructive interference will occur can be directly obtained for all $\boldsymbol{R}$ from the maxima and minima of the sine term (and the special case $\theta_{\boldsymbol{aR}} + \theta_{-\boldsymbol{aR}} = \pi$), giving:

$$\text{maxima}: k = \frac{\pi}{2a}(2n-1) \quad (25)$$

$$\text{minima}: k = \frac{n\pi}{a} \quad (26)$$

where n is any integer.

With this comparison, an attempt has been made to show how interference patterns are produced in electron experiments with localized emission and clarify the difference between this and the more well-known slit interference. The main differences arise due to the first order *scattered* waves which alter the location of the intensity maxima and minima

within the pattern as the wavenumber of the emitted electrons is varied. When a second scatterer is included, interference patterns from the two individual scatterers can add constructively or completely cancel. The different scattering atoms can therefore influence each other in the measuring process, modifying the recorded structural information of the system as a whole.

III. Holography

In localized-emission electron holography, the collected electron interference patterns are transformed to give three-dimensional real space images. However, we see from the last section that in certain cases the interference intensities due to a particular atom or atoms may be partially or completely eliminated by other superimposed patterns. In these cases, holographic transformations will fail to image that particular atom, since the image integral transform requires sufficient information to generate the intensity associated with that atom.

The effect is illustrated in a simple forward scattering cluster model used here as an example. The experimental system of Chapters 2 and 3 is used as a model [8]. We consider an emitting atom buried three layers below the surface of an 80 atom bulk hcp lattice with the lattice parameter of bulk platinum. The changes of real space atom intensity are monitored as we step through wavenumber of the outgoing electron. The single-scattering model is as ideal as possible -- plane wave emitters and scatterers according to:

$$\psi(\boldsymbol{R}) = \sum_{j=1}^{n} \frac{e^{ikR}}{ikR} \cdot \left(1 + \frac{e^{ikr_j}}{ikr_j} \cdot e^{-i\boldsymbol{k}\cdot\boldsymbol{r}_j} \right), \qquad (27)$$

which is a modified combined form of equations (7) and (10).

Figure 4.4 shows the relative real space intensities of the center of one atom in each of the four layers of atoms used in the calculation. The wavenumber range spanned was k

= 5Å^{-1} to 15Å^{-1} (95 to 957eV). They were obtained from the integral transform of the individual interference patterns, using an 84° opening angle mapped into a 64x64 matrix with dimension corresponding to the full width of the k = 15Å^{-1} pattern, which is approximately an angular resolution of 1°. Note, only slight differences were noted for full π opening angle patterns. Figure 4.4a is the result from one of the six nearest neighbors in the emitter layer, at z = 0.00Å. Figure 4.4b shows the same result from the three nearest neighbor atoms in the layer above at z = 2.26Å, 4.4c represents the nearest atomic neighbors in the next layer at z = 4.52Å, and 4.4d is the result from the single atom three layers directly above the emitter, at z = 6.79Å. Figure 4.4e is the simple result of a single atom alone in the same location as one of the three atoms in Figure 4.4b, included for comparison.

As we can see from this figure, the intensities of any given atom in the cluster will vary as the energy is changed. This is quite different from the slowly increasing intensity of the single atom case of Figure 4.4e. Although only the forward scattering cases have been shown, the same effect is apparent for atoms in the backscattering direction, however the frequency of oscillations are much higher due to the longer path length differences of the atoms from the emitter to the detector. Adsorbate studies will be most sensitive in these studies.

Since the intensity variation is dependent on the geometry, changing the lattice parameter will cause these oscillations to shift. In Figure 4.5a, the result from Figure 4.4b is compared to the same result from a cluster 5% smaller. As expected, the features move toward a higher wavenumber. Additionally, by observing the patterns from a different face of the same crystal, the basic oscillation result for a given atom should be the same, although this will depend on the distance from the emitter and size of the opening angle measured. An example is shown in Figure 4.5b, where the same atom as in Figure 4.4b is measured, now at z = 1.96Å in the 4-fold (110) surface. The broader envelope around the oscillation is dependent on the size of the window measured and the direction.

IV. Discussion

According to the original derivation of the imaging integral established by Barton employing the Helmholtz-Kirchoff equation [2], the location of a single point source emitting a plane wave at some distance from the emitter may be identified from the diffraction pattern formed from the combination of the emitter's outgoing "reference" wave and this "scattered" wave. This is certainly the case for a single emitter-scatterer pair over a continuous range of electron wavenumber. However, if more than one scattering center is present, the interference pattern collected at a given wavenumber will contain a combination of individually scattered waves. These scattered waves can also interfere, and may greatly affect and/or change the information due to other scattering ion cores. This pattern distortion will be reflected in the real-space image obtained upon application of the imaging integral transformation, which may or may not agree with the reality of the system under investigation. This problem occurs because the imaging integral itself is designed around a single emitter-scatterer pair, and does not intrinsically account for the presence of additional scatterers. Using the example of slit interference for comparison to electron interference, the interaction of two and three equal sources has been compared to that of a source and scattered wave to identify how both the kinetic energy of the electrons and the geometry of the near-surface atoms (k and r) cause changes in the patterns. The changes in the patterns of the individual atoms consequently affect the information contained therein.

This study does not involve itself with the atomic scattering physics beyond the purely geometrical relationships and *ideal* localized-emission electron holography. The goal is to isolate the tractable structural information inherent in this method of holographic reconstruction, which is fundamentally based on a point source model. At this point we break from optical holography, in which the objects being imaged are usually much larger than the wavelength of light used and generally less symmetric. The comparative size of our interference lines is enough to largely affect others over the complete range of measurement, and periodic and symmetric structures are prone to give substantial overlap.

This problem is greatest in systems where there is complete inversion symmetry. The effect of image intensity variation with atoms at $\pm \boldsymbol{r}$ in photoelectron holography has been predicted previously by Len and co-workers [20], and in these studies it is attributed to twin image cancellation upon application of the transformation, instead of fundamentally related to the interference itself. By taking another look at the process, we can understand how all atoms depend on the others, not just on their inverses. It is a phase relationship between all the waves, all of the scattered emission from atoms can and will affect each other, especially in the total interference pattern.

If the goal of the technique is to directly determine a crystal structure using localized-emission electron holography, this idea needs to be understood prior to making measurements. From these simple calculations, it has been shown that even in ideal conditions atoms in different layers may essentially disappear. Although atom intensity variations will be further compounded by the atomic scattering physics of the system, understanding of pattern cancellation or partial cancellation due to multiple interference sources related to the energy (k) and geometry (r) helps in the interpretation of results. This also means that the previously mentioned corrective methods which attempt to address the effects of the scattering physics will not apply in these cases. Since the structural information is not recorded, it is not stored in any form which may be retrieved.

Certain factors will aid in improving the structural content of the interference patterns to make their transformations more reliable. First, anything that breaks the inherent symmetry of the system will help. This could include the study of unsymmetric or low symmetry systems. Scattering factors could potentially help, since they provide anisotropic intensity to the atomic Gabor zone plate [11] with variation in angle. In this way, destructive tendencies in different areas of the pattern may be reduced, leaving strong information from only one scattering center in a given region of the pattern. Such patterns can be interpreted more directly, assuming the forward focusing is not strong enough to eliminate the majority of the interference. Polarized reference waves in photoemission will

also help, since higher angular momentum emission is rarely spherically symmetric. Finally, the type of analyzer used will determine the reliability of images. A display-type analyzer (moveable with respect to ε) will not have the forced symmetry of a fixed analyzer with a moveable crystal.

Another factor that must be considered is the wavenumber of the outgoing electrons used. Obviously this will be difficult to predict with unknown systems, since the geometry of the system will determine at which energy the best images should appear. However, by measuring a number of different patterns at different wavenumbers one may be able to compare transformed results to determine which intensities agree in a majority of the patterns. Alternatively, or in conjunction, calculations could be made to give an approximation of the best range to explore. A multiple-wavenumber phased-sum approach [18] may further aid in image interpretation, since there will be wavenumbers at which any particular atom should have significant intensity if the stepping is appropriate over a wide enough range. In fact, for a completely unknown system, this is our best hope. Even this method will not always work as we can see from the example of Figure 4.4, since there are sometimes large spans of wavenumber where little or no intensity is present for certain atoms within the system being studied. In these cases, even the multiple-wavenumber sum result will contain very weak or missing atoms. Special care must be taken to make sure a wide enough range is measured, and/or we must look for atoms at different locations in different wavenumber ranges. In all these cases, undesirable origin intensity should always be expected, as well as atom images appearing with variable intensities.

V. Photoelectron *Diffraction*/Interference

The types of patterns we measure are essentially due to interference. To obtain diffraction we would need atoms spaced much more closely or a much lower kinetic energy of the electrons, with all emitting simultaneously with equal strength. One could create a *diffraction* effect in calculation by closely spacing atoms in a line perpendicular to the

normal and having them all emit together. A diffraction/interference combination, which happens in visible light 2-slit diffraction, could be created by placing a similar set of closely spaced atoms further away at a larger spacing *d*. Something interesting to note is that although we would expect strong zero-order interference from the large number of identical adjacent emitters in a crystal, we observe instead primarily scattering interference. In our true dynamical system, all atoms in a crystal do not emit at the same time or from the same place (due to the incoming photon flux and small atomic cross sections) while all of the emitted electrons do scatter and interfere similarly.

VI. Conclusion

Conditions which lead to apparent 'missing' atom intensity in holographic reconstructions have been described starting from the basic principles of scattering -- and the specificity of the holographic transformation applied. The measured interference patterns deviate from an absolutely ideal case due to the combination of the patterns from all of the individual scattering atoms. This effect is purely geometric, involving no detailed atomic scattering physics. Inclusions of the latter may counter some of the effects addressed here, however they may also give rise to other related problems which must be considered individually. This study should help in better understanding some of the fundamental idiosyncracies of the technique of localized-emission electron holography for proper and accurate future applications.

References

[1] A. Szoke, in *Short Wavelength Coherent Radiation: Generation and Applications*, edited by D.T. Atwood and J. Bokor (AIP Conf. Proc. 146, New York, 1986).

[2] J.J. Barton, Phys. Rev. Lett. 61 (1988) 1356; J. Electron Spectrosc. 51 (1990) 37.

[3] G.R. Harp, D.K. Saldin and B.P. Tonner, Phys. Rev. Lett. 65 (1990) 1012; Phys. Rev. B. 42 (1990) 9199.

[4] D.K. Saldin, P.L. De Andres, Phys. Rev. Lett. 64 (1990) 1270.

[5] C.M. Wei, T.C. Zhao, and S.Y. Tong, Phys. Rev. Lett. 65 (1990) 2278.

[6] G.S. Herman, S. Thevuthasan, T.T. Tran, Y.J. Kim and C.S. Fadley, Phys. Rev. Lett. 68 (1992) 650.

[7] L.J. Terminello, J.J. Barton and D.A. Lapiano-Smith, Phys. Rev. Lett. 70 (1993) 599; J. Vac. Sci. Technol. B 10 (1992) 2088.

[8] B.L. Petersen, L.J. Terminello, J.J. Barton and D.A. Shirley, Chem. Phys. Lett. 213 (1993) 412; Chem. Phys Lett 220 (1994) 46. (See Chapters 2 and 3)

[9] A.Stuck, D. Naumović, H.A. Aebischer, T. Greber, J.Osterwalder and L. Schlapbach, Surf. Sci. 264 (1992) 380; Surf. Sci. 274 (1992) 441.

[10] J. Osterwalder, R. Fasel, A. Stuck, P. Aebi, L. Schlapbach, J. Electr. Spectros. in press.

[11] D.K. Saldin, G.R. Harp, B.L. Chen and B.P. Tonner, Phys. Rev. B 44 (1991) 2480.

[12] D.K. Saldin, G.R. Harp, and B.P. Tonner. Phys. Rev. B 45 (1992) 9629.

[13] J.J. Barton and L.J. Terminello, Phys. Rev. B 46 (1992) 13548.

[14] S.Y. Tong, C.M. Wei, T.C. Zhao, H. Huang and H. Li, Phys. Rev. Lett. 66 (1991) 60.

[15] G.R. Harp, D.K. Saldin, X. Chen, Z.-L. Han and B.P Tonner, J. Electr. Spectros. Relat. Phenom. 57 (1991) 331.

[16] G.R. Harp, D.K. Saldin, X. Chen, Z.-L. Han and B.P Tonner, J. Electr. Spectros. Relat. Phenom. 57 (1991) 331.

[17] D.K. Saldin, X. Chen, N.C. Kothari, and M.H. Patel, Phys. Rev. Lett. 70 (1993) 1112.

[18] J.J. Barton, Phys. Rev. Lett. 67 (1991) 3106.

[19] J.J. Barton, S.W. Robey, and D.A. Shirley, Phys. Rev. B. 34 (1986) 778.

[20] P. M. Len, S. Thevuthasan, C.S. Fadley, A.P. Kaduwela, and M.A. Van Hove, Phys. Rev. B. 50 (1994) 11275.

Figure Captions

Figure 4.1. *Slit vs. photoelectron interference.* Panels (a) and (c) show the two- and three-slit experimental configuration, where the coherent source waves are shown as slits illuminated simultaneously. These may be directly compared to the photoelectron interference cases of panels (b) and (d), respectively, where there is only one source wave which generates secondary waves at the scattering atoms.

Figure 4.2. *Two-slit/two-atom $\chi(k)$ comparison.* Panels (a) and (b) show the $\chi(k)$ intensity variation vs. θ for a two-slit experiment at two different wavenumbers. On the right, the corresponding two dimensional full 2π k-space pattern is shown. In the slit experiment, there will always be a maximum at θ=0°. Panels (c), (d), and (e) present the $\chi(k)$ result for a two-atom case over the same wavenumber range, but now the intensity at θ=0° varies with the energy.

Figure 4.3. *Three-slit/three-atom $\chi(k)$ comparison.* Panels (a) and (b) show the $\chi(k)$ intensity variation vs. θ for a three-slit experiment at two different wavenumbers. On the right, the corresponding two dimensional full 2π k-space pattern is shown. In the slit experiment, there will always be a maximum at θ=0°. Panels (c), (d), and (e) present the $\chi(k)$ result for a two-atom case over the same wavenumber range, but now the intensity due to each of the separate scattering atoms can add constructively (panels (c) and (e)) or destructively (panel (d)), leaving only the two-slit interference result from the two coherent scatterers.

Figure 4.4. *Three-dimensional holography layer comparison.* Panels (a) through (d) show how the real space intensities of nearest neighbor atoms in four different layers (at z = 0.00, 2.26, 4.52, and 6.79Å) vary with wavenumber. The (111) surface of an hcp

lattice in a forward scattering geometry was employed in the calculation, using an 80 atom cluster and the lattice parameter of bulk platinum. Patterns were measured over an 84° opening angle into the same k-space range for all wavenumbers. Panel (e) shows the same result for a single scattering atom (2 atom cluster) in the same location as panel (b), included for comparison.

Figure 4.5. *Geometry comparison.* Panel (a) shows how the result of Figure 4b is changed using a 5% smaller lattice parameter. Panel (b) shows the intensity of the same atom at z = 1.86Å in the (100) surface.

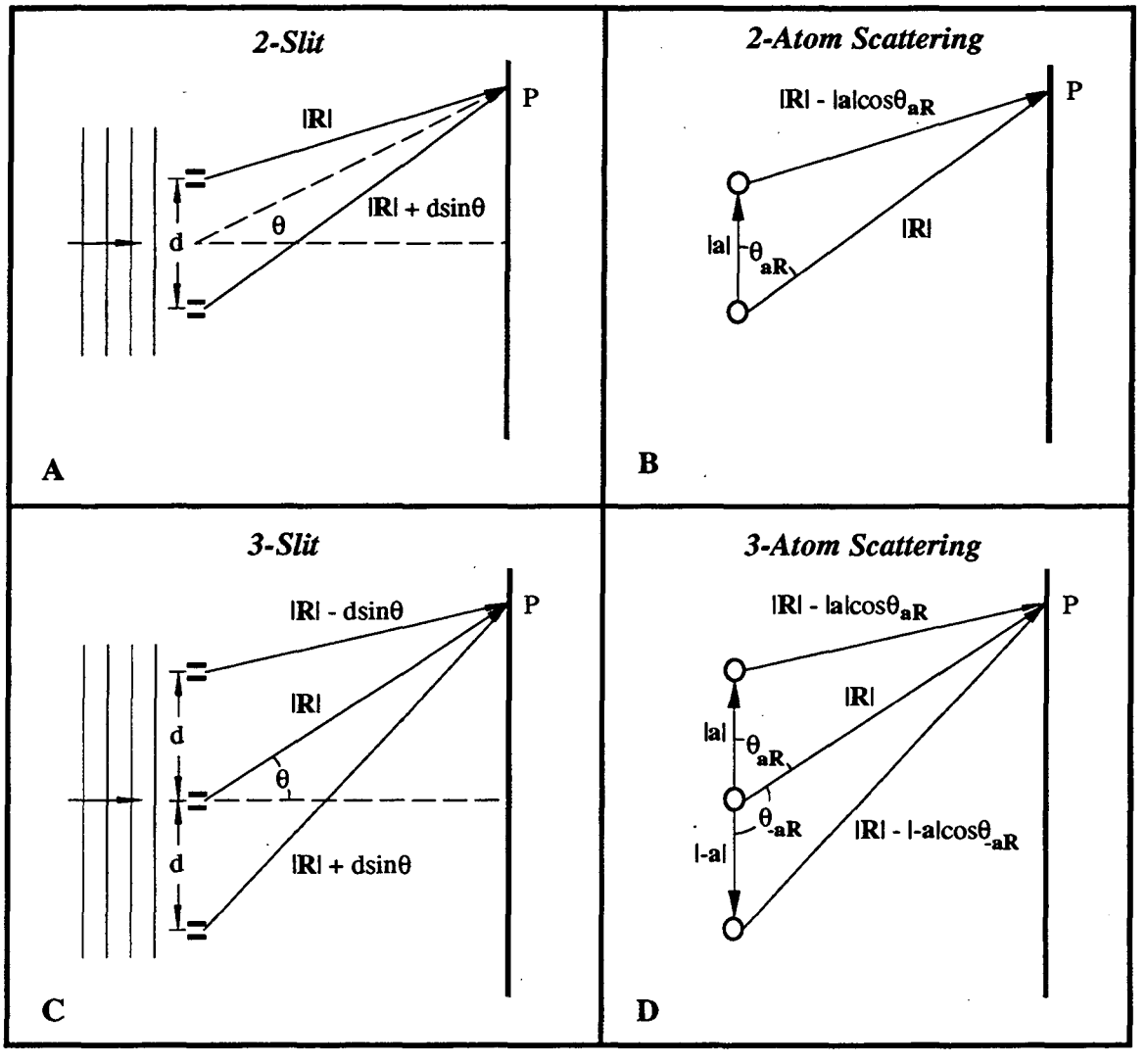
2-Slit
|R|
P
|R| + dsinθ
θ
d
A
2-Atom Scattering
|R| - |a|cosθaR
P
|a|
θaR
|R|
B
3-Slit
|R| - dsinθ
P
|R|
d
θ
d
|R| + dsinθ
C
3-Atom Scattering
|R| - |a|cosθaR
P
|R|
|a|
θaR
θ-aR
|-a|
|R| - |-a|cosθ-aR
D

Figure 4.1

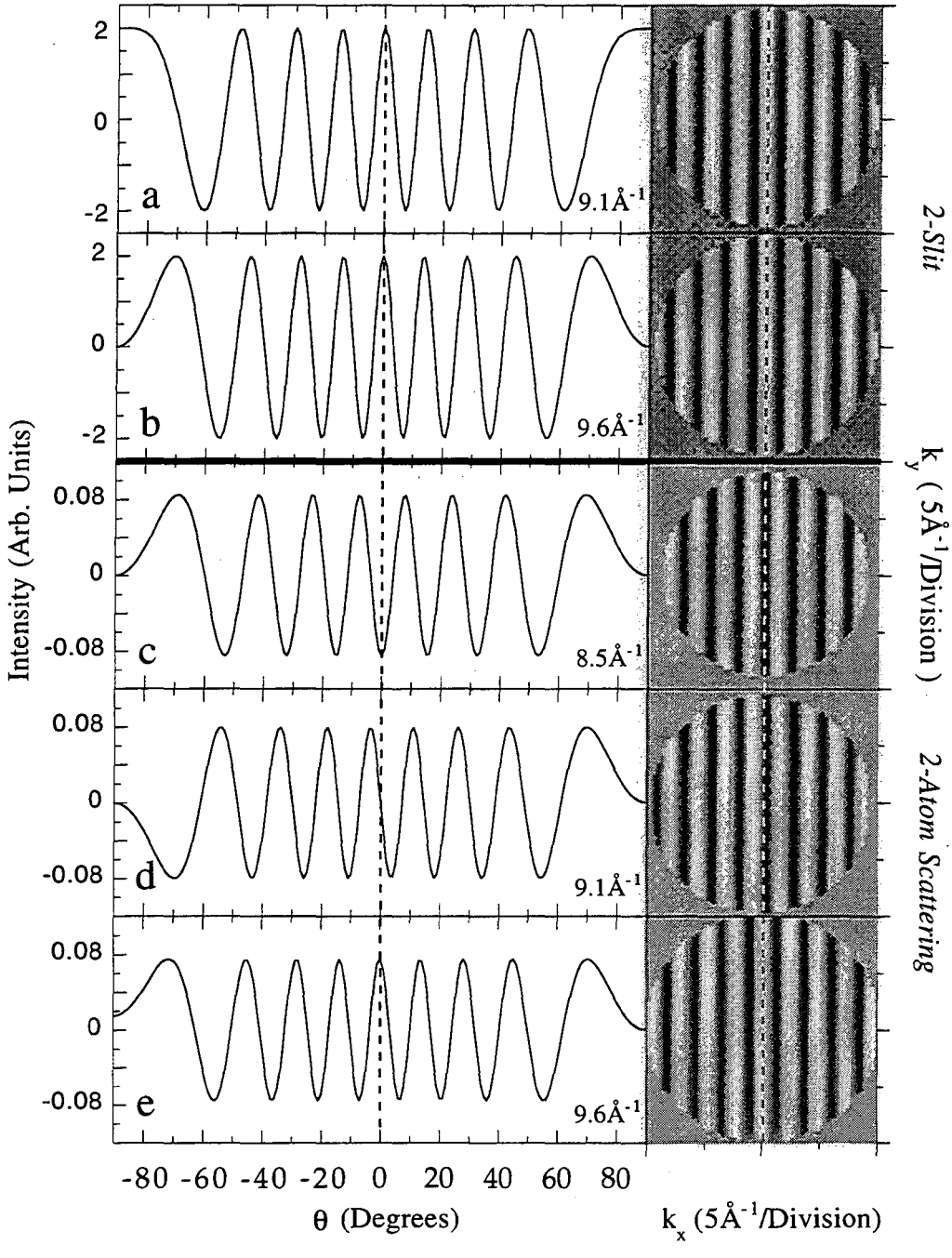
2
0
-2
a
9.1Å-1
b
9.6Å-1
0.08
0
-0.08
c
8.5Å-1
d
9.1Å-1
e
9.6Å-1
Intensity (Arb. Units)
-80 -60 -40 -20 0 20 40 60 80
θ (Degrees)
2-Slit
2-Atom Scattering
ky (5Å-1/Division)
kx (5Å-1/Division)

Figure 4.2

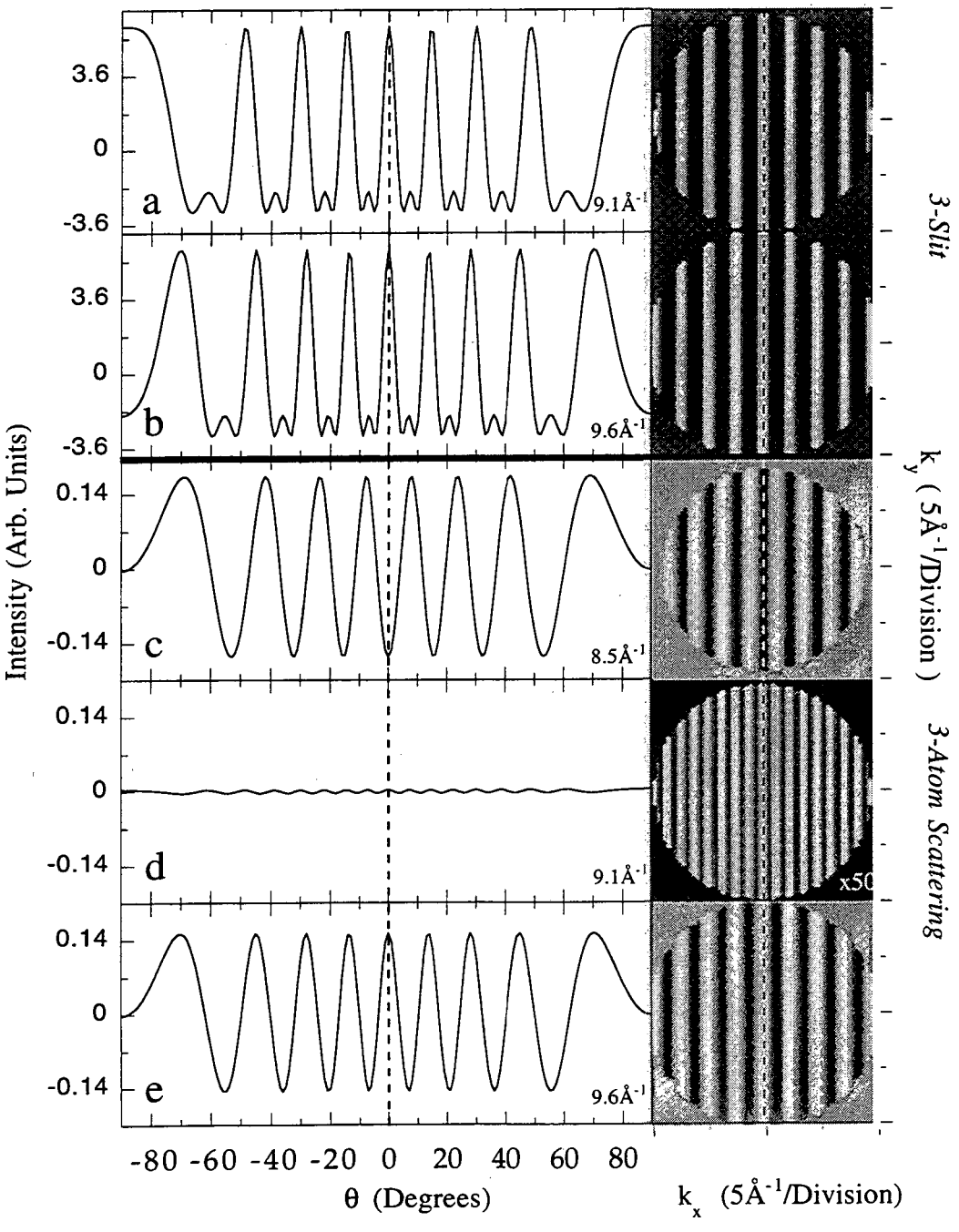
3.6
0
-3.6
a
9.1Å-1
3.6
0
-3.6
b
9.6Å-1
0.14
0
-0.14
c
8.5Å-1
0.14
0
-0.14
d
9.1Å-1
x50
0.14
0
-0.14
e
9.6Å-1
Intensity (Arb. Units)
-80 -60 -40 -20 0 20 40 60 80
θ (Degrees)
kx (5Å-1/Division)
ky (5Å-1/Division)
3-Slit
3-Atom Scattering

Figure 4.3

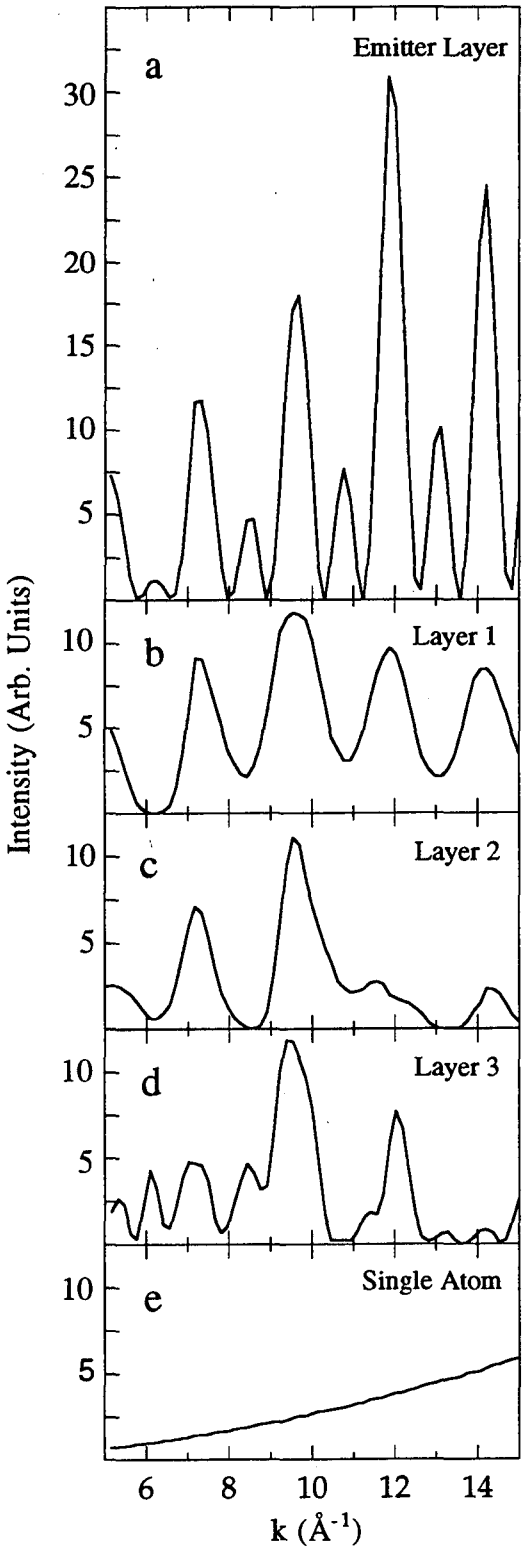
a
Emitter Layer
30
25
20
15
10
5
b
Layer 1
10
5
c
Layer 2
10
5
d
Layer 3
10
5
e
Single Atom
10
5
Intensity (Arb. Units)
6
8
10
12
14
k (Å^{-1})

Figure 4.4

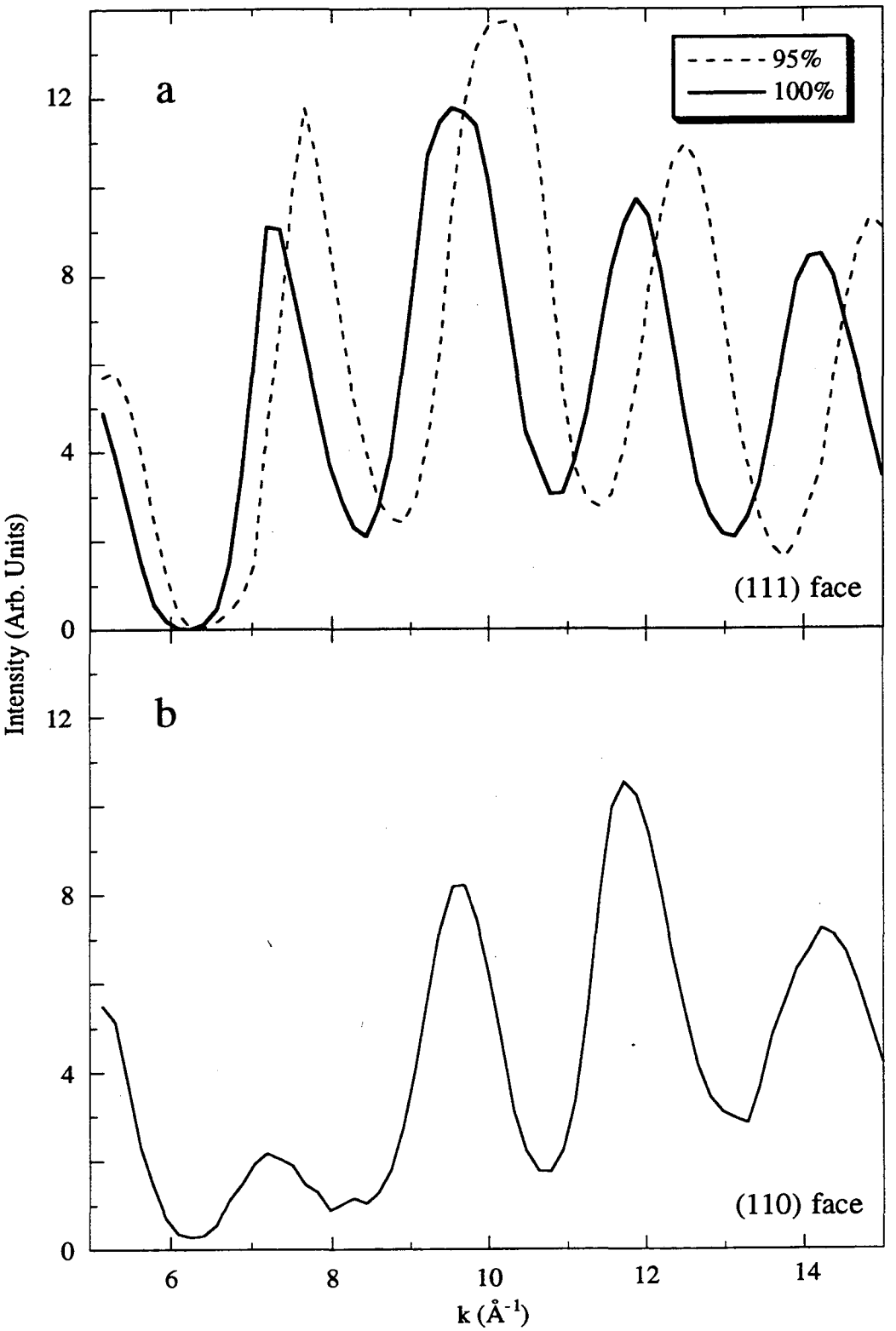
a
95%
100%
(111) face
b
(110) face
Intensity (Arb. Units)
k (Å^{-1})
0
4
8
12
6
10
14

Figure 4.5

Chapter 5

PLATINUM (111) AT 351 eV EXPLAINED: LOCALIZED-EMISSION ELECTRON HOLOGRAPHY USING BASIC SCATTERING THEORY

Abstract: Localized-emission electron holography is explored using a basic theoretical framework to model the different components of electron angular distribution patterns in order to fully describe an experimental set. This study includes a simplified formalism for electron scattering followed by applications of this theory to scattering factors, source waves, experimental configurations, and corrections. Scattering factor distortions of holographic images and corrections are shown and examined. Pattern intensities are explored as a difference between the contributions of the source wave at the scattering atom and the same wave at the detector, including the corresponding relation to imaging. Within this same formalism, the experimental configuration is considered as a determinant for the images obtained, in terms of imaged atom intensity and resolution. Corrective techniques are discussed with focus on Gaussian convolution using much smaller values of σ than reported in the work of others. This study culminates in a complete description of the origin and final holographically-determined images of the previously reported experimental data of a clean platinum (111) single crystal surface at 351 eV.

I. Introduction

Since the initial suggestion by Szöke [1] that electron wave intensity could be analyzed holographically for determination of atomic-scale structure, progress has been made toward its application to real systems. Barton's [2] establishment of a mathematical formalism for generating the images initiated the process of experimental confirmation of the technique [3], and the results of these early experiments gave rise to its subsequent development. Additional studies [4-8] established the wider applicability of the process and employed a variety of excitation methods and electron origins, which has led to the use of the generalized name, *localized-emission electron holography* (LEEH). Although this process has not been entirely straightforward, its early shortcomings have aided in refining expectations and have helped make improvements which will inevitably strengthen the technique. The final outcome promises the production of a holographic method for routine structural determination.

Probably the most valuable feature of localized-emission electron holography is its direct nature. In this technique, the result is obtained from the measured data without the necessity of theoretical comparison. Without this comparison, the data should reveal the *true* structure, which is not necessarily the same structure determined from theoretical simulations. Although theory-based procedures have worked with varying levels of success in the past, there remains potential for incorrect final geometries and often the intensive calculations become computationally prohibitive. Iterative fitting procedures are much better suited for application when an initial structure is known. Nevertheless, the success of obtaining valuable images from localized-emission electron holography will depend on the understanding of the theory governing electron emission. Variations from ideal models stem from the influence of the scattering physics Knowledge of the source of these variations can aid in their handling and lead to more ideal images.

The premise behind holographic imaging of atoms with electrons in localized-emission electron holography is the ability to use localized electron emission from a

specific atom which serves as a reference wave that may be scattered from surrounding atoms to produce secondary waves. These secondary waves interfere with the source wave in the far field region, and produce interference "holograms" with appropriate removal of the reference wave. This hologram retains the three-dimensional structural information of the emitting atom's local environment. Because of the generally limited mean free path of electrons with kinetic energies on the order of a few hundred electron volts (~<10Å), this process is particularly useful for surface, interface, thin film or even bulk studies of atoms and molecules organized in periodic structures. The chemical specificity associated with the atomic cores also allows choice of the emitting atom, which can help in the identification of individual atoms in multicomponent systems. Electron scattering and interference has been described in more detail elsewhere [9].

In LEEH experiments, electron angular distribution patterns (ADPs) are collected from as many angles as possible above the sample of interest. Unlike some types of XPS studies which attempt to use strong forward scattering features to determine the orientation of chains of atoms and relative angles, LEEH involves the direct transformation of this collected ADP to generate the three dimensional image [2]. Further improvements may be made by combination of patterns at other wavenumbers [10], to essentially complete the interference measurement and the third dimension of k-space. The present study is limited to the origin and understanding of the electron interference pattern at a single wavenumber.

It is possible to obtain images of atom intensity from direct measurements of electron intensity, as shown in numerous examples [3,5-8]. However, such straightforward acquisition of correct and indisputable information is not necessarily normal [11,12]. In fact, false peaks, artifacts, splittings, positional shifts, distortions, and intensity variations make any result unreliable. Corrective methods have been employed to some avail [13-16], but even these are often not sufficient to strengthen the questionable reliability of the technique. Only when this reliability is significantly

improved can we hope to make use of the valuable three-dimensional and direct characteristics of the method for routine surface, bulk, and interface structural determinations.

To improve the reliability of LEEH, it will be necessary to understand as much as possible about the technique with regard to the phase and amplitude relationships obtained from our measurements. There is a difference between knowing the origins of the results we expect and those of the results we actually obtain experimentally. An approach to the solution of this problem involves interpretation of the pattern constituents through relation to an ideal model which must necessarily always give the correct result. This process provides a simple tool to determine the origin of some of the unexpected results, to extract the appropriate information from the data, and to plan more effective future experiments. In Chapter 4 we explored atom intensity variation in LEEH as a function of only the wavenumber and the geometry of the system of interest [17]. In these studies, it was determined that a significant portion of the intensity resulting from the interference of the emitted wave and the wave scattered from a single atom must exist before an image of that atom can be obtained. In the this chapter, the study continues by exploring how the phase and amplitude effects due to the fundamental scattering physics of the system determine the pattern creation and its corresponding three-dimensional image.

Our primary interest is how the phase and amplitude inherent in the scattering process are manifested in the measured angular distribution pattern (ADP) of electron intensity. We want to know what portion of the pattern arises from a single scatterer, and how several or many of these interference patterns may combine. Some of these concepts have been explored previously [18,20], and the intention here is to continue the exploration by showing which features do not correspond to useful information and how they may alter or detract from the information necessary for imaging. From previous studies [18,19], it is known how atomic scattering factors modify the pattern and the

corresponding effect on the transformed images, and in this study we make use of this knowledge to extract the structurally meaningful information. The angular momentum contribution has been previously explored in some detail for spherically symmetric electron emission [20,21], where it was found that the source wave can cause changes in the measured patterns. Here, we examine the role of the final state of the emitted electron source wave with respect to spatial orientation due to linear polarization. These major components, the scattering factor and the source wave, form the basis of the information which is created in an electron scattering experiment, and deviations from ideal can usually be traced back to these fundamental concepts.

After establishing the origin of the features in the measured patterns, a study is made of the measuring process. Despite similarities, the experimental arrangement chosen in cases of anisotropic emission can determine the appearance of the pattern, as well as the image obtained upon transformation. Experimental factors also determine the resolution of the image and this potential contribution to the distortion of the atom shape. This knowledge may guide the choice of experimental approach and help predict the type of image expected from the studies chosen.

As the sources of problems are better understood, it is possible to apply appropriate corrective procedures to the data. These procedures can be used not only to eliminate or reduce problems, but also to further improve the images obtained prior to correction. It is important to understand differences between true and extraneous information, and how to separate the two. The goal has always been to obtain results which require no previous knowledge of the system under investigation, hence the corrections applied here are general and should be applicable to all systems. The main examples focus on the use of Gaussian convolution [19], a low pass filter which can be used as a tool. Other corrective techniques are also discussed.

In the last section, we observe how the preceding information applies to the experimental photoemission pattern obtained in Chapter 2, a platinum (111) single crystal

surface at k=9.6Å^{-1} (351 eV) [22]. The earlier results are confirmed with a more thorough applied approach. Using simple single scattering theory conscious of the experimental configuration, the major features of this pattern and its corresponding transformed three-dimensional image are reproduced. With this example, the intention is to show how improved knowledge of the electron scattering theory greatly improves the reliability of LEEH application and results.

II. The Interference View

Before exploring the focus of this chapter, the relation of phase and amplitude effects of the scattering physics to the outcome of the final image, it is important first to reestablish the importance of the concept of geometric effects and the differences between ideal imaging and LEEH as we apply it. This concept was explained in detail previously in Chapter 4, where it was shown how ideal holography can still lead to unphysical results (atom intensity variations) based solely on the relative positions of atoms in a crystal and the wavenumber of the emitted electrons [17]. The problem was attributed to the fact that holography as we apply it is based on the interference of the waves of two point sources, whereas in real experiments patterns from more than one scattering center, hence more than one "hologram", combine at the detector to form the measured result. Although it has been assumed that the overlap of separate atomic zone plates has no great effect [18], it was determined that the ability to obtain an image of a particular atom from a given pattern actually depends on how much of the information of that atom remains in the pattern after the combined waves interact at the detector.

In the current study, we still must consider this problem, although prediction of when it will happen will not be as straightforward as in the ideal case. Any variation which changes the form of the pattern we measure from a single atom will in turn change the combined interference, making our holographic analysis an increasingly complex problem. In certain specific cases, scattering factors may equivalently cancel from

inverse symmetry [23], but generally cancellation will be more indirect. Sometimes this change may help clarify the result, but at other times it may be detrimental. These interference effects are always present and their importance cannot be overlooked.

III. Ideal Theory

The ideal version of electron scattering necessary for LEEH is one where the intensity at the detector results from the coherent interaction of the source wave with the combination of all of the secondary waves created at and emitted from the scattering centers in the crystal. In the simplest case, the source wave, ψ_0, has the form of an isotropic spherical wave:

$$\psi_0(\boldsymbol{r}) = \frac{e^{ik|\boldsymbol{r}|}}{ik|\boldsymbol{r}|}, \tag{1}$$

where all constant factors have been removed and the asymptotic limit expansion of the Hankel function of the first kind ($h^{(1)}(r)$ *as* $r \to \infty$) is used. The scattered waves, ψ_S, can be written in a plane wave approximation as a geometrically phase-shifted plane wave proportional to the original source wave:

$$\psi_{S_a}(\boldsymbol{r}) = \psi_0(\boldsymbol{r_a}) \cdot \frac{e^{ik\cdot|\boldsymbol{r}-\boldsymbol{r_a}|}}{ik|\boldsymbol{r}-\boldsymbol{r_a}|} \tag{2}$$

$$= \frac{e^{ik|\boldsymbol{r_a}|}}{ik|\boldsymbol{r_a}|} \cdot \frac{e^{ik|\boldsymbol{r}-\boldsymbol{r_a}|}}{ik|\boldsymbol{r}-\boldsymbol{r_a}|}. \tag{3}$$

The total wave at the detector, $\Psi_T(\boldsymbol{R})$, is given as:

$$\Psi_T(\boldsymbol{R}) = \psi_0(\boldsymbol{R}) + \sum_n \psi_{S_n}(\boldsymbol{R}) + \sum_m \sum_n \psi_{S_n}(\boldsymbol{R})\psi_{S_m}(\boldsymbol{R}) + \ldots \tag{4}$$

$$= \frac{e^{ik|R|}}{ik|R|}\left(1+\sum_n \frac{e^{ikr_n}}{ikr_n}\cdot e^{-ik\cdot r_n}\right) \tag{5}$$

where the secondary scattering terms are assumed small and the far-field condition ($|R| >> |r_a|$) has been used. The total intensity is given by the absolute square of this wavefield.

In this ideal representation, the original and scattered waves are expressed as point sources or geometrically phase-shifted point sources without attention given to the factors associated with the atomic physics of the full scattering problem of atoms in crystals. For a more exact expression, we would also have to include the effective scattering factor, $f(k\cdot r)$, which describes more precisely how the source wave propagates at the scattering cores, and what will be termed a source wave angular factor, $A(r)$, comprised of an amplitude multiplied by a spherical harmonic, which gives information relating to the phase and amplitude of the emitted source wave when it is not purely spherical.

If we include *only* the scattering factor and the source wave angular factor in our ideal single scattering model expression, we arrive at a similar result as in (5), with general modifications given as:

$$\psi_0(r) = A(r)\cdot\frac{e^{ik|r|}}{ik|r|} \tag{6}$$

$$\psi_{S_a}(r) = \psi_0(r_a)\cdot f(k\cdot r_a)\cdot\frac{e^{ik\cdot|r-r_a|}}{ik|r-r_a|} \tag{7}$$

$$= A(r_a)\cdot\frac{e^{ik|r_a|}}{ik|r_a|}\cdot f(k\cdot r)\cdot\frac{e^{ik|r-r_a|}}{ik|r-r_a|}. \tag{8}$$

and

$$\Psi_T(\boldsymbol{R}) = A(\boldsymbol{R}) \cdot \frac{e^{ik|\boldsymbol{R}|}}{ik|\boldsymbol{R}|} \cdot \left(1 + \sum_n \frac{A(\boldsymbol{r}_n)}{A(\boldsymbol{R})} \cdot f(\boldsymbol{k} \cdot \boldsymbol{r}_n) \cdot \frac{e^{ikr_n}}{ikr_n} \cdot e^{-i\boldsymbol{k} \cdot \boldsymbol{r}_n} \right), \quad (9)$$

where in the plane wave case,

$$f(\boldsymbol{k} \cdot \boldsymbol{r}_n) = \frac{1}{ik} \sum_{l=0}^{l_{max}} (2l+1) T_l(k) P_l(\hat{\boldsymbol{R}} \cdot \hat{\boldsymbol{r}}_n), \quad (10)$$

$$T_l(k) = \frac{1}{2}(e^{2i\delta_l} - 1) = i \sin \delta_l \cdot e^{i\delta_l}, \quad (11)$$

and $P_l(\hat{\boldsymbol{R}} \cdot \hat{\boldsymbol{r}}_n)$ are the associated Legendre polynomials and δ_l are the calculated plane wave phase shifts. More exact representations can be expressed in alternative forms, for example, as "separable" Green's functions [24], which can be combined with spherical wave corrected atomic scattering factors [25,26] and multiple scattering [25,27]. The data is also sensitive to the already mentioned centrifugal potential (orbital angular momentum dependence) [20,21], as well as other factors including the inner potential, temperature, and random noise. These effects are not included directly in this study since they are outside of the scope of the more fundamental topics which we are exploring. We are making the general assumption that over the range of wavenumbers chosen, the patterns are dominated by single scattering features, which are the features most germane to LEEH. Curved wavefronts are modeled here by generalized plane wave approximations, and the angular dependence will vary for multiple final states [28].

Real-space images were obtained from the two-dimensional *k*-space $\chi(k)$ patterns of NxN points by multiplying them by a phasing term (to select the appropriate position in z) and then applying a two-dimensional image integral transform, digitized for use according to:

$$U_{p,q}(z) = \frac{4}{N^2} e^{-i\pi p - i\pi q} \sum_{m=0}^{N-1} \sum_{n=0}^{N-1} \chi_{m,n} e^{ikz\sqrt{1-k_x(n)-k_y(m)}} e^{i2\pi qm/N} e^{i2\pi pn/N} \quad (12)$$

where p and q are lateral x and y indices in the image [29]. This transformation yields a two-dimensional real-space slice of intensity at the selected z position. The most intense features in these slices should be centered around the x, y coordinates of atomic positions. Vertical slices are taken from three-dimensional volume sets obtained by stacking multiple x-y slices over the desired z-range. All matrices used in the k-space maps were 64x64 pixels in dimension, and the code used for all of the calculations were designed based on these equations.

Background Removal

At this point we consider the removal of the background and its implications in this work. According to the theory [2],the final interference portion, $\chi(k_x,k_y)$, is obtained from the total intensity, I_T, after removal of the source wave, I_0, by subtraction and division, as:

$$\chi(k_x,k_y) = \frac{I - I_0}{I_0}. \quad (13)$$

However, this expression is difficult to achieve experimentally and sometimes theoretically. Experimentally, it is impossible to measure I_0, that intensity due to the source wave alone, and the separate slowly varying intensity imposed across the recorded interference lines of separate atoms. We only measure secondary electrons and the analyzer throughput function. The 'I_0' is removed by convolution with a Gaussian and division from the total intensity I_T. Theoretically, there will be a problem not in the subtraction, but in the division whenever interference fringes and nodes meet. In s-wave types of emission and certain experimental configurations, I_0 serves only as a scaling factor; it becomes more of a problem in the case of anisotropic emission. For anisotropic

studies in this chapter, an approximation of the pattern is made by subtracting I_0 without dividing. Fortunately, the broad oscillation imposed onto the theoretical data does not largely affect the transform result and can be completely removed later with Gaussian convolution. In certain cases, symmetry averaging may reduce the effect, as it diminishes the localized anisotropy across a pattern. Extensive multiple scattering can also randomize the phase and amplitude of the wave at the detector [18], which makes it more isotropic and of a different form than at the source.

Attention in this study will be directed at the differences between equations (5) and (9) and the corresponding differences after application of the imaging integral. The following section will explore how scattering factors affect the final images, and section V will look more specifically at the form of the final state/source wave. The remainder of the chapter employs the information obtained in these studies for improved application and understanding of the technique.

IV. Scattering Factor

The first portion of our analysis examines the contribution of the effective scattering factor on the images obtained from LEEH. Although this contribution has been analyzed in some detail previously [18,19], the goal here is to review how the scattering factor is manifested in the pattern and its relation to the final images. It is primarily included for completeness. Knowing how the scattering factor affects the measured pattern also allows the ability for correction.

The effective scattering factor is a convenient mathematical expression which determines how the incoming wave is acted upon at the scattering center along its path to other atoms or the detector. In the case of pure elastic scattering, there is no modification, such that the scattered wave is simply a spherical wave of lower intensity than the original source wave. Formally, the wave incident on the scattering center is expressed as a summation of spherical harmonics at the location of an atom which is

acted upon by a scattering transition matrix which employs the calculated or experimentally determined angular momenta (l) dependent atomic phase shifts of the scattering atom [30]. Now, instead of purely spherical character, the scattered wave has angular dependent phase and amplitude modifications as it propagates either to other scattering atoms or to the detector. Approximations of this model use the plane wave limit at the scattering center to estimate the waveform in this vicinity, which simplifies the calculation of the scattering transition matrix. Further simplifications of this model include the use of only the dominant phase shifts of the lower angular momentum states to approximate the transition. Now a well understood phenomenon, the strongly peaked nature of the true scattering factor at higher wavenumbers leads to experimentally confirmed forward focusing, an effect often used for structural studies to determine the geometry of atoms on surfaces [9].

To observe an example of the presence of the forward focusing effect, a model system was used which consisted of a single platinum atom with coordinates (0, -1.59, 2.26), in the position of one of the three atoms directly above the emitter for the fcc (111) surface arrangement. Employing an ideal scattering model, a calculation was made of how the pattern would look under ideal conditions -- purely s-wave type emission at $k=9.6\text{Å}^{-1}$ with a full analyzer opening angle of 180°. This is essentially an atomic Gabor zone plate. The results of this calculation are shown in row A of Figure 5.1. The first column shows the calculated k-space ADP, with columns II and III showing slices through the three-dimensional x-y and x-z plane at the location appropriate for the expected position of this atom. As expected, the atom position falls exactly as it should in the ideal case, as marked by a cross.

Row B shows how the pattern changes as a result of using only the $l=0$ phase shift in the calculation of the scattering factor, a phase change of the scattered wave with no angular dependence. In this case, the change can be viewed directly as an intensity variation as compared to the ADP in row A. Although the pattern may have a different

appearance, its transformed image remains the same as in the ideal case, since the phase change has no effect on the imaging properties in this case [18]. Remember also that the shift of the interference intensity will change the atom intensity variations from those of the ideal case upon addition of more scatterers, as described in Section II.

Row C shows the result with the inclusion of the full expression of the plane wave phase shift, which increases the intensity of the pattern along the direction of forward scattering. The shape of this scattering factor amplitude is convoluted with the phase shifted original interference pattern. The image obtained after transformation results from a convolution of the scattering factor with the ideal atom image, giving positional displacement in the x-y and x-z planes, as well as an elongation along the scattering direction as seen in columns II and III. Although not as dramatic for platinum at this wavenumber, this is the primary source for the displacement of the intensity of the transformed atom image, as shown by others in earlier studies [18,19]. Also, it should be noted that no additional artifacts are present in the center portion of the image, since we only use a single scattering atom.

Row D shows the effect of the corrective method of convolution and division by a Gaussian, the basic details of which are covered in reference 18 and in Section VII. It is included here to show how removal of some of the anisotropy of the final pattern can help to reproduce the ideal expected images. Panel DI shows the same k-space pattern as in row C with the strong forward intensity reduced. Correction of the images is not perfect, but a returning tendency of the atom intensity to the correct position is observed in both the x-y and x-z slices (panels DII and DIII) along with reduction of the elongation away from the emitter. Other corrective techniques will also be discussed in Section VII.

The scattering factor has the effect of changing an ideal pattern in both phase and amplitude. The phase of the scattered wave can change the location of interference fringe intensity, giving rise to a complication of interference effects when more atoms are present in the system. The amplitude is convoluted with the ideal atom image, which

gives rise to both positional displacement and in some cases may also cause apparent splitting of atomic images, since variation of intensity of the scattering factor will also give corresponding variable intensity of the atom image in space.

V. Effect of the Source Wave

One of the most important concepts to understand in emission electron scattering is the effect of the source wave on the final measured result. In all cases of localized electron emission, scattered waves from surrounding atoms interfere with this source wave more strongly than with any other, so any detected variations in intensity are due mainly to this primary interference. This source wave can have many different forms, depending on the type of exciting radiation and the specific type of electrons studied. Photon stimulated emission can differ from electron stimulated emission, and polarized radiation can produce different source waves in terms of phase, shape, and orientation. The observed electrons and corresponding source wave can vary substantially between, for example, photoelectrons, Kikuchi electrons, and Auger electrons. Additionally, the source wave often becomes a complicated mixture of simpler waves, as in Auger or higher angular momenta photoemission, which makes interpretation of the scattering more complex. The current intention is to distinguish the general effects of the source wave due to these deviations from the ideal model, and eventually use this information to help interpret the measured results.

In this ideal model, the source wave is purely spherical, with phase and amplitude radially symmetric, as in s-wave ($lf = 0$) types of emission. Kikuchi electrons may fall into this category, and Auger electrons are assumed to have equal probability of emission in all directions since the Auger transition involves atomic inner-shell processes which lose memory of the initial excitation. Non-ideal source waves common to polarized photoemission can generally vary in both phase and amplitude per angular direction, and this variation is manifested in the resulting interference. In equation (9) this type of

variation is conveniently described as a complex angular factor $A(\boldsymbol{r})$, which becomes a prefactor for the ideal spherical wave expression, $exp(ikr)/ikr$, of the source wave, $\psi_0(\boldsymbol{r})$. From this method of writing the equation, it becomes apparent how the angular dependence affects the measurement in two distinct locations -- once at the initial creation of the scattered wave, $\psi_0(\boldsymbol{r_a})$, from equation (8), and again at the point of detection, $\psi_0(\boldsymbol{R})$, from equation (6). Knowing how this source wave at both locations determines the result gives us a key to understanding how the imaging takes place and, as we shall see in the next section, how the appearance of the measured ADP can be dependent on the experimental configuration.

To explore the consequences of non-s initial states, a study is performed using a simple photoemission example, an outgoing p-type (l_f=1), assuming a straightforward case of linearly polarized photons where the ε-vector is directed perpendicular to the incoming light. Centrifugal potentials [20,21] are not considered here. In this example, a display-type (or moveable) analyzer configuration (ε-vector fixed relative to sample) was chosen, where the detector measures the full 180° opening angle above a fixed sample. This detector type allows us to visualize the effects of wave anisotropy more directly than other possible experimental configurations, which will be described later. The goal is to isolate the effect of the source wave at the atoms, $\psi_0(\boldsymbol{r_a})$, and compare it with the source wave at the detector, $\psi_0(\boldsymbol{R})$. Since this is a hypothetical study, we can remove the anisotropy of either of these waves by setting the prefactor $A(\boldsymbol{r})$ to a constant value for the initial part of this study. The system consists of a four-atom cluster of platinum atoms which constitute the emitter atom and the three nearest neighbors one layer above for the Pt(111) surface. The results of this study are shown in Figure 5.2.

The rows of Figure 5.2 are divided into three panels: column I consists of a schematic of the analyzer with the four atoms shown and a graphical representation of the wave ψ_0, both at the atoms and at the detector, column II contains a k-space map at k=9.6Å^{-1} corresponding to the total 180° emission angle with the surface normal in the

center, and column III contains an x-y slice from the transform taken through the three atoms at z=2.26Å. Row 5.2A shows the ideal version, with spherical emission both at $\psi_0(\boldsymbol{r_a})$ and $\psi_0(\boldsymbol{R})$, along with its ADP and x-y slice. Rows 5.2B and 5.2C correspond to the contribution due to $\psi_0(\boldsymbol{r_a})$ when there is no angular contribution from $\psi_0(\boldsymbol{R})$. Row 5.2B shows the result when the polarization is θ=45° and ϕ=0°, where the lobe of $\psi_0(\boldsymbol{r_a})$ is directed toward one atom and the corresponding ADP is dominated by the interference of that atom, as well as the x-y slice as shown in panel BIII. Row 5.2C shows the result when the polarization is θ=45° and ϕ=180°, with the $\psi_0(\boldsymbol{r_a})$ lobe now directed between the other two atoms. In this case, the ADP is dominated by the interference of these two atoms, which the x-y slice reveals.

In rows 5.2D and 5.2E, $\psi_0(\boldsymbol{r_a})$ is left unaffected by the wave anisotropy and adjust $\psi_0(\boldsymbol{R})$. Row 5.2D shows the result when the polarization is θ=45° and ϕ=0°, and the corresponding ADP, in column II, shows that the relative interference of the three atoms does not change significantly from ideal, although the broad intensity across the pattern varies with angle. When this pattern is transformed all three atoms are imaged equally, column III, with some loss of resolution. Row 5.2E shows the same effect when the polarization is set at θ=45° and ϕ=180°.

Finally, rows F and G show the result of the combined effect, as might occur in an experiment with this configuration for the two different light polarizations. Here we see the relationship of the final transformed image to the directional effect and resolution. This is an ideal result. In an experiment, randomization due to multiple scattering may eliminate the anisotropy at the detector, giving a final result more closely related to rows 5.2B and 5.2C, if we assume the primary scattered wave to be the most intense scattered wave.

The example of Figure 5.2 shows the difference of the source wave at the scattering atoms and at the detector. The wave *at the scattering atoms* determines the initial form of the scattered wave at its own origin and hence its relative measured

intensity as compared with other scattering atoms. This relative intensity in the pattern corresponds directly with the atom's intensity in the transformed real-space image. This effect cannot be eliminated by simple I_0 removal, because it is now an intrinsic part of the scattered waves, ψ_{S_a}. The wave *at the detector* does not change the relative interference fringe intensity of different atoms with respect to each other. Instead, it has the broader purpose of determining which part of the pattern will be illuminated. Hence, it does not determine the presence or strength of an atom in the transformed image, only its resolution. As described in Section III, we can divide it out theoretically, but not experimentally.

This example shows how an ideal hologram retains all of the information of the image, no matter which portion is illuminated. All of these effects combine to give one result, but now we know the origin of this result and can see how the two separate effects can combine to give the final image. It should also be noted here that there are additional questions of phase and amplitude when multiple final states are involved, similar to those found in Auger type transitions [20]; however these questions are beyond the scope of this chapter.

VI. Experimental Configuration

In this section we look at how experimental parameters determine results obtained through LEEH. As in any experiment, the method by which we choose to collect our data determines the data we eventually obtain. With respect to electron ADPs, we have a few variable parameters, such as a fixed or moving analyzer, the electron wavenumber, the opening angle of collection, and the methods of symmetry averaging. Not only do we need to think about how to selectively capture electrons, we also need to know enough about the scattering physics to predict which configuration will best suit our purpose.

The two main analyzer configurations discussed here include the moveable analyzer/fixed crystal (or display), and the fixed analyzer/moveable crystal types. For the

moveable analyzer, all angles above a surface are explored simultaneously, such as in a display-type, or individually, as in an analyzer which can be positioned at different angles relative to the incoming radiation. The fixed angle-resolving analyzer maintains a constant angle between the incoming radiation and the analyzer, and requires rotation of the sample in order to explore the different angles. These two methods are fundamentally different in design and will potentially give different results. Sometimes the two types of analyzers are combined, and the results will be complicated according to how the measurement is performed.

In purely s-wave or spherically symmetric types of emission, the pattern will be independent of the type of analyzer used. The major differences in the collected data from the two analyzers arise when there is anisotropy in the source wave. The anisotropies cause inequivalent source wave phase and amplitude at the scattering centers, which then relate directly to the attributes of the scattered wave, according to equation (8). In the case of a display analyzer, the source wave variation is fixed in space relative to the atoms in the crystal, so the results produce patterns and corresponding images dominated by scatterers which receive the most intense portion of the source wave. For a fixed analyzer/moveable sample arrangement, the scattering atoms move through an unvarying source wave, while the analyzer's position relative to the ε–vector remains fixed (the angle between ε and $\boldsymbol{R}$ is constant), so the scattering strength varies depending on the atom's position relative to the source wave. Again, the patterns and images obtained will be dominated by the scatterers in the measured angular range which receive the most intensity from $\psi_0(\boldsymbol{r}_a)$.

Figure 5.3 shows a comparison of the ideal results we may expect from different types of analyzers with anisotropic final emitted states. No scattering factor is used in this study, only elastic spherical scattering from the surrounding cores. This is done to help isolate the effect due to the source wave. For simplification, a simple linearly polarized photoemission case has been chosen again, an l_i=0 initial state which generates

an l_f=1 final state wave with z-axis directed along the ε-vector. For our study, we compare a fixed analyzer condition where the analyzer is fixed at α=0°, where α represents the angle between ε and $\boldsymbol{R}$ (maximum amplitude in this case), with a display analyzer in two different ε-vector orientations with respect to the crystal surface, θ=0° and θ=45°, and the effect of symmetry averaging on the display analyzer. In column I is drawn a schematic showing the experimental configuration and the outgoing wave. The second and third columns show the ADP obtained from a two atom and ten atom system, respectively. Columns IV and V show the real space transformed x-y results corresponding to the ten atom system taken in the emitter layer and one layer above the emitter, z=0.00Å and z=2.26Å, respectively.

In the fixed analyzer example, row A, we can see the majority of the intensity in the two atom case is focused in the direction of the scatterer from the emitter. The most straightforward explanation for this effect is the fact that when the scattering atom is in the node of the p-wave, it receives no intensity from the emitted wave and does not contribute to the pattern. The highest intensity in this case will be when the ε-vector is aligned along the emitter-scatterer direction. Other regions of the pattern follow predictably from these two extremes. In the ten atom case, column III, the effect is the same -- the pattern is highlighted in the forward direction of each scattering atom, giving the richest information to the three atoms directly above the emitter. The most intense features for the emitter layer atoms lie along the outer portions of the pattern, but the measured k-space of the pattern is devoted equally to all of the atoms. The transform of this pattern shows equally intense features for the atoms both in the emitter layer and those one layer above, as can be seen in panels AIV and AV.

The second row shows the result from the calculation with the ε-vector fixed normal to the crystal. In the two atom case, the intensity variation at the detector is only due to the varying intensity of the source wave at the detector (it hasn't been divided out) because the atom receives a constant wave at the atom position. When the ten atom case

is calculated in column III, the resulting pattern is a combination of the intensities of the three atoms directly above the emitter, each of which receive the same initial value from the cylindrically symmetric emitted wave. There is no contribution to this pattern from the emitter layer atoms because they reside in the nodal plane of the outgoing wave. The transform results confirm what we read from the pattern, showing no intensity in the emitter layer, column IV, and three atoms in column V at z=2.26Å, as expected.

Another configuration of the moveable analyzer is shown in the row C, where the ε-vector is tilted to 45° off normal along the x-axis. In the two-atom case, column II, the intensity varies only with the wave intensity at the detector, since the scattered wave has the same initial value for all detector positions. In the ten-atom case, however, we see a marked difference from the previous two examples, since now two atoms in the emitter layer atoms and only two of the three atoms above are the main contributors to the measured pattern intensity. Again, the transform result agrees with our assessment, showing two atoms from the emitter layer at z=0.00Å (some image enhancement is due to twin images) and two atoms in the layer directly above the emitter at z=2.26Å.

Row D in Figure 5.3 shows the result obtained when the pattern of the 45° moveable analyzer is three-fold symmetry averaged, because of the known crystal symmetry. This action can complete the pattern, and the transformed images obtained become more ideal. In this case there is similarity between the three-fold symmetry averaged pattern and the fixed analyzer case of row A, but this will not always be true. The symmetry averaged version may be markedly different from the fixed analyzer depending on the polarization, scattering factors, and source wave final state. Note that symmetry averaging the two other patterns, rows A and B, would not be changed with averaging since they are already symmetric. Symmetry averaging in those cases would only serve to improve signal to noise ratios.

From Figure 5.3 we can see how the effect of the source wave in the near and far field regions is manifested in different measurement schemes based on the lowest level of

approximations applied to the ideal case. Another major factor we can control experimentally is the real space resolution of the final image. Resolution, as explained in reference 28, in the x and y directions is given as:

$$|\Delta x| = \frac{1.22\pi}{k\sin(\theta_o / 2)}, \tag{14}$$

while resolution in the z direction will be:

$$|\Delta z| = \frac{4\pi}{k\sin^2(\theta_o / 2)} - \frac{4\sin(\theta_o / 2)}{k}. \tag{15}$$

Further improvement may be obtained in the z direction by a multiple wavenumber phased-sum approach [10], although this will not be discussed here. From these expressions, it is apparent that the resolution is dependent on the electron wavenumber and the opening angle, θ_o. The resolution is generally dictated by the experimental limitations and it has a direct relationship to the shape of the resultant atom images.

The concept of resolution as determined by experimental configuration is explored tin Figure 5.4. In this figure, the ideal model of a single atom 2.26Å above the emitter and s-wave scattering are used to observe the basic effect of changing wavenumber and opening angle on the final transformed images. We observe the x, y, and z resolution decrease with a reduction of wavenumber and opening angle. In column I is a schematic of the analyzer configuration, with smaller hemispheres representing a full 180° pattern at lower wavenumbers and portions of the full k=9.6Å pattern used to show variation in opening angle. Column II shows the ADP obtained and columns III and IV show the transform results, an x-y slice at 2.26Å and an x-z slice at y=0.00Å, respectively, to show the two types of resolution.

Row A is our ideal pattern at k=9.6Å^{-1}. In this case, Δx=0.40Å and Δz=0.89Å, with larger z resolution resulting from measuring a smaller range of k_z than either k_x or k_y. Row B shows the result obtained from the ideal calculation at k=7.2Å^{-1}. Here, Δx=0.53Å and Δz=1.19Å, lower than the original due to the smaller wavenumber. This pattern is compared directly to the k=9.6Å^{-1} pattern in row C with an opening angle of 100°, where the k space range spanned is the same as in the k=7.2Å^{-1} case. As in that case, Δx=0.52Å, but now Δz=1.91Å, as a result of this experimental configuration. Finally, the last two rows, D and E, compare a pattern with k=4.8Å^{-1} (Δx=0.80Å, Δz=1.78Å) and another at k=9.6Å^{-1} with θ_O=60° (Δx=0.80Å and Δz=5.03Å), for a more extreme example. Particularly noticeable in this example is the vertical elongation of the atom image resulting from incomplete measurement of the full angular data range.

In addition to resolution, Figure 5.4 also gives a view of why patterns change with energy. Understanding this concept explains the variation of the ADP with wavenumber. Generally speaking, points where the interference fringes overlap in systems with more than one scatterer are the points of relatively greater intensity. This is the heart of understanding the kaleidoscopic effects of these patterns. The patterns drift further from the ideal at lower energies due to extensive multiple scattering effects and at higher wavenumbers because of the dominant scattering factor-related scattering anisotropies, which tend to dominate features of these ADPs. However, by phase-summing the individual results from a wide range of wavenumbers, images can be improved with an improvement in z-resolution along with a reduction of multiple scattering artifacts and twin images [10]. This idea involves measuring the variations along k_z as well as k_x and k_y, approximating through summation a full three-dimensional transformation from k space to real space.

In this section, an attempt was made to show how experimental configuration in measuring ADPs will be reflected in the atomic images obtained. Specifically, we examined the analyzer type and also the resolution as related to wavenumber and opening

angle. The techniques used to measure the data must always be considered when making final interpretations.

VII. Corrections

Knowing the constitution of a measured ADP will help in the assessment of whether or not an image may be obtained from that particular pattern. If the information we seek is not recorded in the pattern measured, there is no hope of making it appear by the haphazard application of 'corrective' techniques. This may occur even in the most ideal patterns. One of our most valuable assets becomes the ability to recognize the features in an ADP that give it holographic characteristics based on our knowledge of the ideal and at least the basics of scattering physics. Our corrections must be considerate of these factors and use this knowledge to our advantage.

The overriding requirement of any correction we apply is that it does not impose any outside information, or prior knowledge of the system under study, onto the data. The one standard we can never abandon is the application and success of the technique on entirely unknown systems. We also hope that any change made to the pattern does not add unphysical characteristics to the final result. This 'no assumptions - no additions' concept forces a careful handling of the data -- if we chose to make any changes at all.

Experimentalists and theoreticians alike have realized that leaving the data untouched leads to problems of interpretation. Forward scattering peaks lead to unwanted artifacts, and scattering factors (including phase shifts) distort the pattern from their ideal isotropic origins [18,19]. Source waves add their own amplitude and phase which do not necessarily disappear with simple background removal [20,21]. Additionally, random noise or angular distortions may arise during the experimental collection of data. Each effect compounds the problem of extracting valuable images, and each must be faced if we expect to make appropriate use of the technique.

Problems relating to the experiment itself, such as random noise or angular distortions may be handled directly -- angular distortions may be corrected by mapping and the noise generally falls out upon application of the Fourier-type transform. Fortunately, in most cases, the slowly varying I_0 may be approximated from the measured I_T as the broad features and removed by application of a low pass filter on the data. The method of removing the other problems is not so direct.

It has been suggested that the problems due to the scattering factor may be removed by division of the complex scattering factor from the pattern prior to transformation [14,15]. It has been shown to help in theoretical and some experimental applications [18,20]. Iterations on this technique have also been suggested [31]. However, since our goal is to apply the technique to unknown systems, we cannot rely on this correction for anything other than a potential improvement to images we fully understand, since this technique involves knowing both the atomic scattering phase shifts, and the sample constituents prior to application. There is also the more fundamental problem of dividing a real pattern by a complex scattering factor and expecting the result to approximate that of a complex pattern treated similarly. Finally, this correction may be inappropriate for accurate structural determination since distortions due to scattering factors may actually overcome some of the problems associated with the interference effects of ideal scattering mentioned in Section II.

Another technique suggested for the improvement of results involves a swept window method [13], wherein transformations of portions, or windows, of the entire data set are conducted in order to highlight those interference fringes due to a particular scatterer. In this way, images can be isolated separately, unaffected by their cross-relationships. This technique, however, assumes that the experimentalist knows the geometrical origin of all of the interference lines in a given pattern *and* has the ability to isolate them from one another. This tends to be easier at higher wavenumbers, since forward scattering is stronger, but in lower ranges more diffraction lines are present and

there is greater overlap across the pattern. This overlap makes the determination and separation of different regions of interference more difficult and also making the assumptions more unreliable.

The most effective and unobtrusive corrective technique which has been employed for background removal is a simple Fourier-filtering process which involves convolution of the two-dimensional pattern with a two-dimensional Gaussian [19] and subsequent division. In this process, the ADP and the Gaussian field of unitary total area and of variable σ are separately Fourier transformed, multiplied together in k-space, and the resulting matrix is inverse transformed back into real space. The original pattern is then divided, not subtracted, by the newly created Gaussian convolution and 1 is subtracted from the result to assure that the resulting interference waves oscillate around zero. By varying the value of σ for the two-dimensional Gaussian, we have an adjustable low pass filter which determines the lowest allowed frequency of the remaining pattern, or the breadth of the features we wish to remove.

There are three main types of broad oscillations we desire to remove using this technique. The first are the anisotropies or broad background due to the source wave, both over the entire pattern and that due to the variation of intensity caused by $\psi_0(\boldsymbol{r}_a)$, which imposes a broad feature across the recorded interference of an individual scatterer. The second broad features we try to remove are those imposed by the scattering factor -- forward scattering peak intensity that does not necessarily contribute to the desired holographic interference as partially discussed in section IV. The third type of feature we attempt to reduce are the intensities due to interference fringe crossings of the patterns due to the different scattering atoms. These features can generate symmetric points of intensity, sometimes called "diffraction peaks", which can be distributed randomly throughout the pattern. Their symmetry potentially generates unexpected artifacts which would not be present in the ideal two-atom ADP [18].

One other aspect that should be mentioned is the equalization of the fringe intensities due to the broader interference of close atoms and the higher frequency interference fringes of atoms which are further from the emitter. This allows for all of the atoms to be imaged with similar intensity upon transformation. The process is basically a reduction of the more dominant strength of the nearest neighbors due to their lower frequency of oscillation. This process involves using a much smaller σ value than suggested in reference 18, since we are now much more interested in removing artifacts completely and equalizing atom intensities throughout the image. The main difference in our application of this technique from other work is the smaller width (σ) of the Gaussian peak used for the convolution. By not limiting this σ value, it has been possible to equalize and retrieve relatively more information from the pattern by taking care to isolate the higher frequency oscillations, improving the image fidelity and often removing artifacts entirely.

Figure 5.5 illustrates the process of Gaussian convolution, removal, and the changes that result in the transformed images. The first three rows show the convolution process and its subsequent removal in the condition of a full 180° opening angle and purely isotropic source wave. A full plane wave scattering factor was used for the six nearest neighbors directly above the emitter, as shown above column I. Row A shows the ideal pattern, with background removed, and the integral transform at the layer of the emitter and one layer above. In columns II and III, there are strong artifacts in the emitter layer and the three nearest neighbors one layer above are highlighted at z=2.26Å. Row B is the result of convolution of the original pattern with a two-dimensional Gaussian field with σ=0.02. In general, it retains most of the broad features of the original. The second and third columns show the result of a direct transformation of this convoluted function, which show the features which are being removed. As seen, the artifacts and the stronger features of the layer above the emitter are present here. Finally, row C shows the result of the original pattern divided by the Gaussian convoluted function. Only the higher

frequency interference lines remain, and upon transformation now show artifacts in the layer of the emitter and six equal-strength intensities representing the atoms we were originally trying to image at z=2.26Å.

The two lower patterns, rows D and E are the same as the first and third patterns taken with a smaller opening angle, 100°. In this case, we examine how the physical removal of the higher frequency interference lines of the nearest neighbors leaves only high frequency interferences from the more distant atoms. This has the effect of reducing the intensity of the nearest neighbors to lower than that of the atoms further out. This problem may be remedied by using a Gaussian function with a larger sigma value. In this example, the hope is to better show the process that is occurring in this correction. In fact, the geometry of the analyzer as well as angular resolution may change the measured results by determining which interference fringes of separate scattering process are being measured and reduced.

Often after the removal of the convoluted function, the edges of the pattern are artificially high due to the inability of the Gaussian to closely model the step at the edge of the pattern. In these cases, the inner 90% of the pattern is usually taken and the data at the edge is sacrificed. Obviously this data could be saved by other methods, such as different modeling functions. The resulting pattern generally does not have many problems with Fourier ringing, primarily because the majority of the edge intensity is reduced with the Gaussian convolution. A method of further reducing edge effects involves the multiplication of the pattern by some edge-smoothing function prior to transformation. This has the effect of reducing small artifacts throughout the image and broadening atom images in the final result. In fact, the multiplication with a Gaussian function of σ=0.2 was the procedure followed in the sliced images of reference 21, in which the atoms are isolated with apparently fewer artifacts and poorer resolution. This Gaussian-multiplication technique has been found to potentially cause additional artifacts

in the three-dimensional volume and reduces valuable recorded information, making it difficult to use in more robust analytical applications.

In this section corrective procedures which are used on measured data to improve the result after holographic transformation have been discussed. The goal was to show how the corrective methods return the pattern to a more ideal form for holography, by considering those factors which we know are due to either the atomic scattering physics or the experimental configuration. Again it must be stressed that if the correct information was not measured initially, obtaining the exact result cannot be expected, even if the corrections could return the image to the perfect ideal isotropic scattering model. We can only hope for improvement of the information we measure by unobtrusive removal of the portion unrelated to the pertinent interference intensity which records the true structure.

VIII. Comparison of Simple Theory and Experiment

At this stage in the overview of LEEH, it becomes particularly illustrative to make a connection between the fundamental theory of the processes of LEEH and the presented experimental result. The goal has been to attempt to find the underlying causes for the particular data measured and understand the origins of these causes. Using the framework established in the previous sections of this chapter, the current intention is to show how the pattern at 351 eV was created. The model used is not exact. Rather, focus is directed intentionally on a simple model which does not allow us to lose sight of the fundamental holographic interference which underlies the experimental measurement and is vital to the creation of a useful three-dimensional image.

The (111) surface of a platinum single-crystal was cleaned by argon sputtering at $1x10^{-5}$ torr of argon for one hour, followed by resistively annealing for three minutes at ca 850° C. The sample cleanliness was monitored by the photoelectron spectrum of platinum, which was taken repeatedly throughout the experiment and compared to the

initial spectrum obtained immediately after sample preparation. The crystal was oriented so that the surface normal formed the central ray of the electron "cone" accepted in the display analyzer. The crystal position was fine-tuned by observing the symmetry of the Fermi-surface map obtained from angular distribution patterns from valence-band photoelectrons. The photon beam was incident upon the crystal at a 45° angle, and the electric polarization vector was therefore oriented at 45° relative to the surface normal. All measurements were made at room temperature.

The data were collected with the ellipsoidal mirror display analyzer [32] on the IBM U8 VUV beamline [33] at the National Synchrotron Light Source at Brookhaven National Laboratory. The acceptance angle of the analyzer is ca 84°, with a typical instrumental energy resolution of 0.3 eV while measuring holograms with an angular resolution of 1/4°. For the present measurements the analyzer was operated in the constant-final-state mode, in which electrons of a single energy are collected. The photon energy was changed when background electrons at the same wavenumber were desired, and the analyzer voltages were kept fixed. A background spectrum taken on the high-kinetic energy side of the photoelectron peak was used for normalization. The measuring time was ca. 2 hours for the background and ca. 1 hour for the higher-signal photopeak.

The data reduction process is shown in Figure 5.6. Panels 5.6A and 5.6B show the angle space intensity maps of the photopeak and background, respectively. In panel 5.6C, the result of the peak divided by the background is shown. The intensities at the given angles are mapped to their corresponding positions in momentum space in panel 5.6D, after centering and correcting for the 0.75 aspect ratio of the CCD video camera. Convolution with a Gaussian of σ=0.02 and subsequent division is performed on this data, producing the pattern of panel 5.6E. The final panel, 5.6F, is the 3-fold symmetry averaged version of 5.6E. This last pattern, retaining a total opening angle of about 70°, is the one used for the final symmetric transformed images.

To model this system, a basic cluster photoelectron scattering code for linearly polarized light with an l_i=0 (l_f=1) source wave and scattering was used, employing the plane wave scattering factor of platinum at 351 eV. The p-wave final state of the source wave was chosen as an approximation to the true l_f=2, 4 final state expected for emission from a 4f core level from dipole selection rules [34], which govern the angular momentum composition of the source wave. More attention is given to the basic effect of a strongly anisotropic, directional outgoing wave rather than to the exact solution. This system includes 19 emitter layer atoms, 21 atoms in each of the next two layers above, and 19 atoms three layers above an emitter in the center of the emitter layer for a total of 80 atoms. No atoms are included below the emitter layer because of the expected lower intensity due to backscattering. Only one emitter type is used, although all atoms in this bulk system are potential emitters.

In the theoretical calculation, the experimental configuration is modeled as closely as possible. This model assumes a display-type analyzer with the ε- and **a**-vectors fixed while varying **R**. The polarization of the light was 45° off normal at an angle of ϕ=195° from the arbitrary plane bisecting the triangles formed in the two layers above. The opening angle was 70°. After calculation, the pattern was three-fold symmetry averaged and the background was removed using a Gaussian with σ=0.02.

A brief description of the modeling process includes an initial photoelectron excitation by incoming light, with the outgoing p-wave generating a directionally variable wave. This wave only approximates the true relative initial strength of the wave at each atom, corresponding to the features in the interference pattern. The experimental geometry determines how the singly scattered electrons are measured at the detector. Phase shifts are used to calculate the plane wave scattering factor, which also dominates how the interference fringe intensity will be recorded. Since there is no strong forward focusing effect, the Gaussian removal here is included to equalize the intensity of near and far scatterer interference, to reduce the broader features resulting from "diffraction

peaks", and to more completely remove the broad intensity due to the source wave (which was not removed by division).

Figure 5.7 shows a comparison of the results of the experimental and theoretical ADPs. Along with the patterns are shown the results of the image integral transformation at four different x-y slices (shown on equivalent intensity scales) corresponding to the emitter layer and the 3 layers above. These slices are not as readily comprehensible as those shown in Chapter 2, because a Gaussian multiplication was not performed prior to transformation [21]. The slices in row B are essentially the same patterns which gave rise to the three-dimensional images shown in that same chapter. The features which should interest us most in this comparison are not only the intensities due to the atoms, but also the agreement between the artifacts of experiment and theory. Perhaps unexpectedly, artifact agreement becomes a good judge of the success of the modeling procedure. The differences in the emitter layer atom intensity are due to the simplistic modeling of the source wave.

In this example, it is possible to see how all of the different components related to an LEEH experiment combine fundamentally to give the final result. The good agreement between simple theory and experiment only help to support our understanding of how these patterns are formed and which features give rise to the three-dimensional images we obtain.

IX. Discussion

To reach the goal of reliable direct attainment of three-dimensional images of surface, bulk, or interface structure, it is essential to know the details of the experiment we perform. By knowing which features are related to structural information as determined by our fundamental understanding of electron wave interference leading to the hologram, we have an idea of when images will form and also which features due to the atomic scattering physics are unnecessary for retrieval of the structure. Only with

consideration of the complete picture can we ascertain the value of any particular experiment or predict its success.

The purpose of this chapter has been an attempted dissection of the major factors intertwined in a measured ADP. The premise has been the understanding of an ideal hologram obtained from purely isotropic source wave and subsequent scattering, which is the basis of the image integral transformation procedure. It is already known that this ideal does not always generate the correct image due to destructive interferences, however it is still our paradigm. Modifications of this ideal pattern in both phase and amplitude result primarily from the effects of the source wave and the scattering factor. These changes tend to either distort the atom image or vary the relative intensity of atoms around an emitter, sometimes adding unphysical artifacts in the process. Additionally, the fundamental differences in experimental configuration can also determine which interference fringes may be featured, which corresponds to different obtained patterns and apparently different results. Corrections may be applied to the data, but only when they do not impose features onto this data.

Complete or full scattering theories are much more involved than the examples which are used in this study. There are many effects which have been (admittedly) conveniently avoided, including multiple scattering, curved waves, multiple initial states, and centrifugal potentials, just to name a few. Additionally, a medium range of electron kinetic energy was maintained, avoiding the potential problems of extensive multiple scattering at lower and strong forward focusing at higher wavenumbers. The assessment is that the topics discussed here are the fundamental deviations from the ideal, and more complex deviations are often manifested in some form of these. For example, although multiple scattering obviously exists, the strongest features are often those resulting from primary scattering. This means that the general features of an ADP will be dominated by single scattering fringes, as well as the corresponding transform. Another example,

multiple initial states, will involve the combination of the effects from single anisotropic states.

This study does not attempt to model the data exactly. In fact, because a transformation based on an ideal model is used, more interest is directed at how simply the results can be modeled. This helps assess the appropriateness of such a direct transformation considering the complexity of the problem under consideration. One of the primary goals of this study is to determine how to design an experiment to take advantage of that information which is well understood, or to highlight the simple geometric information. In LEEH applications, we want to be able to move away from complex fitting procedures which are often time intensive and reduce the directness of the technique.

Multiple-wavenumber studies will obviously improve the quality of the result. Using a phased-sum approach [10,35], we can greatly reduce the effects of multiple scattering and twin images. Yet it is still important to understand that all the patterns measured at each wavenumber are dependent on these effects. The patterns must be individually considered prior to combination or problems may result. Even the multiple wavenumber phased-sum technique requires an ideal input for the transformations, or artifacts and distortions will potentially propagate through to the final result.

Although a bulk system in a forward scattering configuration was used for this study, it is important to point out that the concepts outlined here do not only pertain to this type of system. Backscattering systems follow the same principles, and are often easier to understand due to the more isotropic nature of the backscattering and no presence of twin images (beyond those in the emitter layer). By employing a system which uses forward scattering, it is shown that the technique should also be sufficient for providing the structure of sub-surface layers.

An important result obtained from this study is the value of the ideal result in prediction of our test systems and in the generation of potential patterns for unknowns.

Occasionally, the transform of the ideal system may agree with the experiment but not with the 'expected' result. The experimentalist must be familiar with the reasons why and when images may not be obtained, and how to obtain the most appropriate data for their experiment. Application without fundamental understanding of the principles behind the technique can potentially lead to pitfalls in the analysis of the final results.

X. Conclusion

In this chapter, the effects of fundamental atomic scattering theory on the results obtained in localized-emission electron holography have been examined. It can be seen how the phase and amplitude of the source and scattered waves manifest in the collected angular distribution pattern and the corresponding results after application of the imaging integral transformation. Additionally, the imaging effects of different experimental geometries are shown, as well as the changes which result from the application of corrective procedures. An experimental comparison is made with a simple theoretical model in order to show how the measured experimental pattern results from the scattering discussed. The goal is to gain a more solid grasp of the creation of interference patterns and their connection to holography to insure confident future application of the technique.

References

[1] A. Szoke, in *Short Wavelength Coherent Radiation: Generation and Applications*, edited by D.T. Atwood and J. Bokor (AIP Conf. Proc. 146, New York, 1986).

[2] J.J. Barton, Phys. Rev. Lett. 61 (1988) 1356.

[3] G.R. Harp, D.K. Saldin and B.P. Tonner, Phys. Rev. Lett. 65 (1990) 1012; G.R. Harp, D.K. Saldin and B.P. Tonner, Phys. Rev. B. 42 (1990) 9199.

[4] D.K. Saldin, P.L. De Andres, Phys. Rev. Lett. 64 (1990) 1270.

[5] C.M. Wei, T.C. Zhao, and S.Y. Tong, Phys. Rev. Lett. 65 (1990) 2278.

[6] P. Hu and D.A. King, Nature 353 (1991) 831.

[7] G.S. Herman, S. Thevuthasan, T.T. Tran, Y.J. Kim and C.S. Fadley, Phys. Rev. Lett. 68 (1992) 650.

[8] L.J. Terminello, J.J. Barton and D.A. Lapiano-Smith, Phys. Rev. Lett. 70 (1993) 599; J. Vac. Sci. Technol. B 10 (1992) 2088.

[10] S.A. Chambers, Surf. Sci. Reports 16 No. 6 (1992) 261, and C.S. Fadley in Synchrotron Radiation Research: Advances in Surface Science, edited by R.Z. Bachrach (Plenum Press, New York, 1990).

[10] J.J. Barton and L.J. Terminello, in Structure of Surfaces III, Milwaukee, edited by S.Y. Tong, M.A. Van Hove, X. Xide, and K. Takayanagi (Springer-Verlag, Berlin, 1991) 107; J.J. Barton, Phys. Rev. Lett. 67 (1991) 3106.

[11] A.Stuck, D. Naumović, H.A. Aebischer, T. Greber, J. Osterwalder and L. Schlapbach, Surf. Sci. 264 (1992) 380; Surf. Sci. 274 (1992) 441.

[12] R. Dippel, D.P. Woodruff, X.-M. Hu, M.C. Asensio, A.W. Robinson, K.-M. Schindler, K.-U. Weiss, P. Gardner and A.M. Bradshaw, Phys. Rev. Lett. 68 (1992) 1543.

[13] H. Huang, H. Li and S.Y. Tong, Phys. Rev. B 44 (1990) 3240.

[14] B. P. Tonner, Z.L. Han, G.R. Harp and D.K. Saldin, Phys. Rev. B 43 (1991) 14423.

[15] S.Y. Tong, C.M. Wei, T.C. Zhao, H. Huang and H. Li, Phys. Rev. Lett. 66 (1991) 60.

[16] S. Thevuthasan, G.S. Herman, A.P. Kaduwela, R.S. Saiki, Y.J. Kim, W. Niemczura, M. Burger and C.S. Fadley, Phys. Rev. Lett. 67 (1991) 469.

[17] B.L. Petersen, L.J. Terminello, and D.A. Shirley (in publication). (See Chapter 4)

[18] D.K. Saldin, G.R. Harp, B.L. Chen and B.P. Tonner, Phys. Rev. B 44 (1991) 2480.

[19] G.R. Harp, D.K. Saldin, X. Chen, Z.-L. Han and B.P Tonner, J. Electr. Spectros. Relat. Phenom. 57 (1991) 331.

[20] D.K. Saldin, G.R. Harp, and B.P. Tonner. Phys. Rev. B 45 (1992) 9629.

[21] J.J. Barton and L.J. Terminello, Phys. Rev. B 46 (1992) 13548.

[22] B.L. Petersen, L.J. Terminello, J.J. Barton and D.A. Shirley, Chem. Phys. Lett. 213 (1993) 412. (See Chapter 2)

[23] P. M. Len, S. Thevuthasan, C.S. Fadley, A.P. Kaduwela, and M.A. Van Hove, Phys. Rev. B. 50 (1994) 11275.

[24] J.J. Rehr and R.C. Albers, Phys. Rev. B. 41 (1991) 8139.

[25] J.J. Barton, S.W. Robey, and D.A. Shirley, Phys. Rev. B 34 (1986) 778.

[26] V. Fritsche and P. Rennert, Phys. Status Soldi B 135 (1986) 49.

[27] A.P. Kaduwela, D.J. Friedman, and C.S. Fadley, J. Electron Spectrosc. Relat. Phenom. 57 (1991) 223.

[28] D.J. Friedman and C.S. Fadley, J. Electron Spectrosc. Relat. Phenom. 51 (1990) 689.

[29] J.J. Barton, J. Electron Spectrosc. 51 (1990) 37.

[30] A. Messiah in Quantum Mechanics Vol. I (North-Holland Publishing Company, Amsterdam, 1958).

[31] D.K. Saldin, X. Chen, N.C. Kothari, and M.H. Patel, Phys. Rev. Lett. 70 (1993) 1112.

[32] D.E. Eastman, J.J. Donelon, N.C. Hien and F.J. Himpsel, Nucl. Instrum. Methods 172 (1980) 327.

[33] F.J. Himpsel, Y. Jugnet, D.E. Eastman, J.J. Donelon, D. Grimm, G. Landgren, A. Marx, J.F. Morar, C. Oden, R.A. Pollack, J.Schneir and C. Crider, Nucl. Instrum. Methods Phys. Res. 222 (1984) 107.

[34] S.M. Goldberg, C.S. Fadley, and S. Kono, J. Electron Spectrosc. Related Phenom. 21 (1981) 285.

[35] B.L. Petersen, L.J. Terminello, and D.A. Shirley, Chem. Phys. Lett. 220 (1994) 46. (See Chapter 3).

Figure Captions

Figure 5.1. *Effect of the scattering factor.* Column I shows the full 180° opening angle momentum space electron intensity maps of a theroetical emitter-scatterer system in four different configurations. Column II shows the corresponding x-y slice in the layer of the scatterer, z=2.26Å, and Column II shows the corresponding x-z slice taken at y=0.00Å. Row A is the result from an ideal calculation at k=9.6Å^{-1} with no scattering factor, and Row B shows the same result with only the$l$=0 phase shift included in the scattering factor. In Row C the full plane wave scattering factor is included, and Row D shows the result of C with some anisotropy removed by Gaussian convolution and subsequent division.

Figure 5.2. *Effect of the source wave in the near and far field regions, $\psi_O(r)$.and $\psi_O(R)$.* Column I is a schematic of the relationship between the source wave in the range of the atoms and in the region of the detector. Column II shows the resulting ideal momentum space electron intensity map at k=9.6Å^{-1} obtained for the three nearest neighbors directly above the emitter when no scattering factor is used. Column III shows the corresponding x-y slices taken at the level of the three atoms, at z=2.26Å. Row A is the ideal case, with spherical (l_f=0) emission in the near and far regions. Rows B and C show how the anisotropy of the source wave in the region of the atoms, $\psi_O(r)$., vary the pattern and the corresponding x-y slices using l_f=1 emission with polarized radiation in opposite directions. Rows D and E show the variation resulting from anisotropy in the far field region, $\psi_O(R)$, again at two different polarizations. Rows F and G show the expected result for the combined effect for a single scattering case.

Figure 5.3. *Effect of the analyzer configuration.* Column I shows a schematic of the analyzer arrangement used, either fixed or moveable, and the orientation of the emitted

photoelectron source wave at k=9.6Å^{-1}. Column II shows the electron intensity map for a full 180° pattern for a simple emitter-scatterer system. Column III shows the corresponding map for a ten atom system, arranged as shown above the column. Columns IV and V give x-y slices through the transformed images at z=0.00Å and z=2.26Å, respectively. Row A is the fixed analyzer case, in which the crystal is moved while the angle between the ε-vector and the analyzer remains constant. Rows B and C show the corresponding result for a display analyzer, where the angle between the ε-vector and crystal axes remains constant, in two separate light polarizations, (B) has $\theta=0°$, $\phi=0°$, and (C) has $\theta=45°$, $\phi=0°$. Row D gives the three-fold symmetry averaged result of the ten atom case of row D.

Figure 5.4. *Image resolution as related to experimental arrangement.* Column I gives a schematic showing the configuration used to measure the ideal spherical wave pattern for an emitter-scatterer system while varying the wavenumber of the emitted electrons or the analyzer opening angle. Column II shows the image in the x-y slice through the atom center at z=2.26Å. Column III presents the image in an x-z slice through the atom center at y=0.00Å. Row A is the ideal pattern measured at k=9.6Å^{-1}. Row B is the result for a pattern measured over the same k-space range for k=7.2Å^{-1}. Row C shows the result at k=9.6Å^{-1} with an opening angle, θ_O,of 100°. Rows D and E give a similar comparison to Rows B and C with (D) θ_O=180°, k=7.2Å^{-1}, and (E) θ_O=60°, k=9.6Å^{-1}.

Figure 5.5. *Effect of Gaussian convolution.* Column I shows the electron intensity momentum space map calculated for six scattering atoms above an emitter at k=9.6Å^{-1}. Column II shows the real space transform result x-y slice taken at z=0.00Å. Column III gives the x-y slice through the same volume set at z=2.26Å. Rows A through C show the process of convolution and division, with the initial full 180° plane-wave scattering factor included l_f=0 emission result shown in Row A. Row B shows the Gaussian convoluted

function (σ=0.02) obtained from the pattern in Row A, along with its corresponding transform. In Row C the divided result is shown in Column I, along with the reduced artifact layer at z=0.00Å in column II and the six atoms at z=2.26Å in Column III. Rows D and E show the same patterns as in (A) and (C), and their corresponding transform results when the opening angle is reduced to 100°.

Figure 5.6. *Data reduction.* This figure shows the reduction of the Pt $4f_{5/2}$ (111) surface photoemission data at k=9.6Å^{-1}. Panel (A) shows the collected raw angle-space data and (B) is the background. Panel (C) is the result of the peak divided by the background. Panel (D) shows the result after conversion to a momentum space map and correcting for the aspect ratio of the digitized image. Panel (E) shows the result of (D) after convolution with a Gaussian of σ=0.02, and Panel (F) is the final three-fold symmetry averaged result.

Figure 5.7. *Comparison of experiment with simple theory.* Column I shows the momentum space map of electron intensity for the experiment and theoretical calculation at k=9.6Å^{-1}. Columns II through V show the x-y slices taken at each of four layers above and including the emitter plane. Row A gives a schematic of the slices taken through the volume, with gray used to show the lower intensity atoms in a given layer. Row B shows the experimental pattern of Figure 6F with its corresponding transformed images at each layer. Row C shows the result calculated using a simple single scattering l_f=1 theoretical model conscious of the basic scattering processes and employing the same experimental configuration as in the experiment.

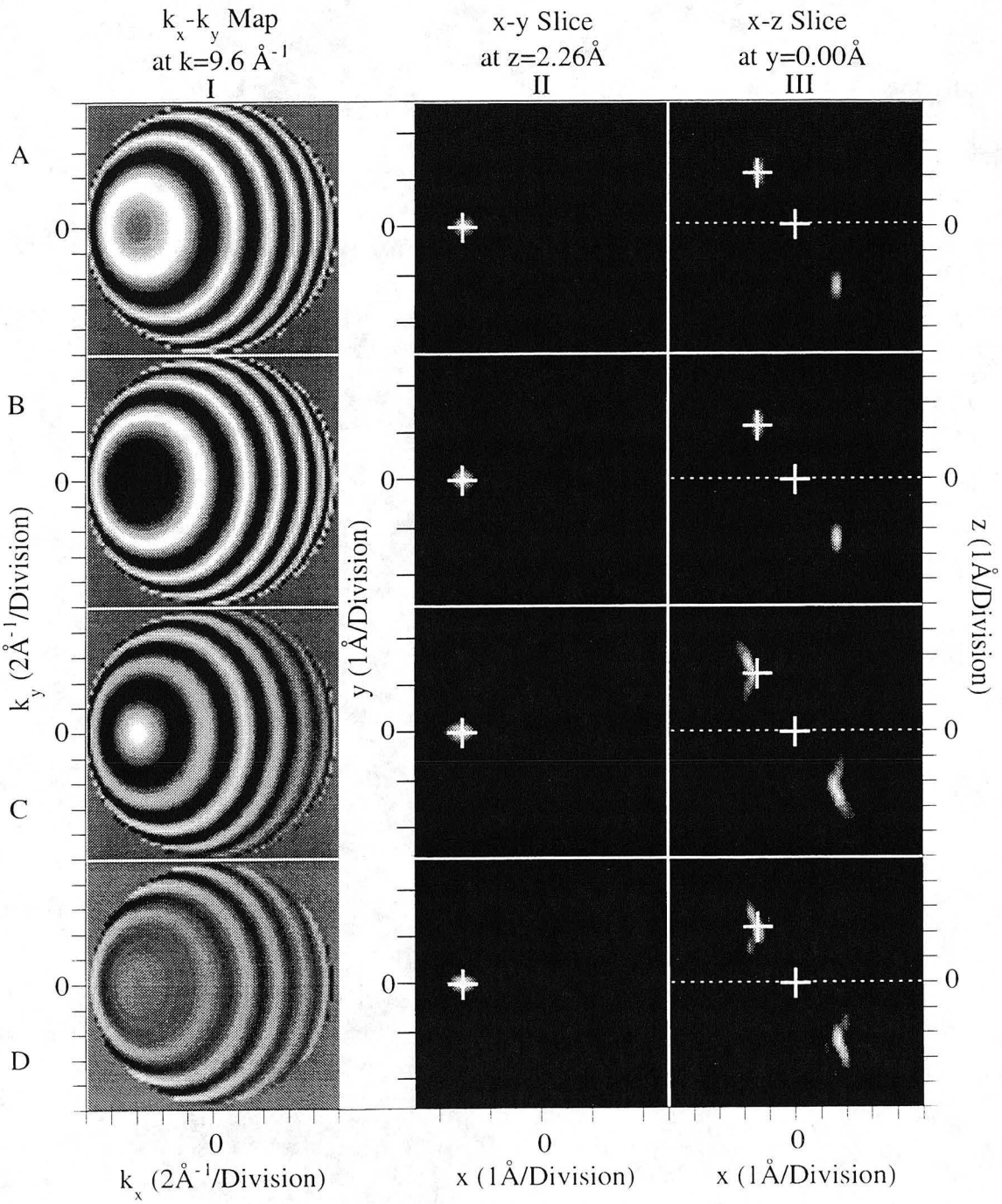
Scattering Factor
k_x-k_y Map
at k=9.6 Å^-1
I
x-y Slice
at z=2.26Å
II
x-z Slice
at y=0.00Å
III
A
B
C
D
0
k_y (2Å^-1/Division)
y (1Å/Division)
z (1Å/Division)
k_x (2Å^-1/Division)
x (1Å/Division)
x (1Å/Division)

Figure 5.1

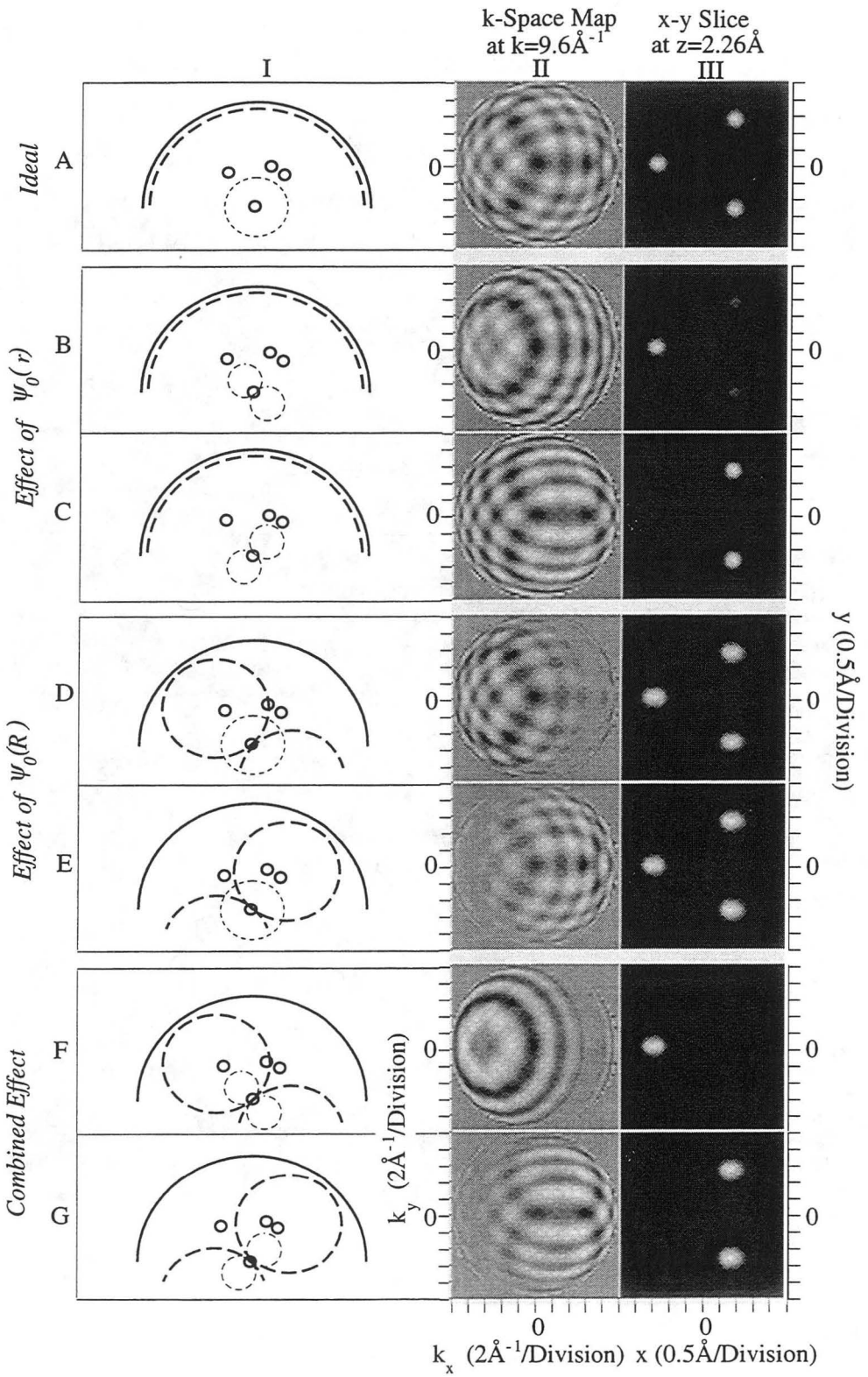
k-Space Map
at k=9.6Å^{-1}
x-y Slice
at z=2.26Å
I
II
III
Ideal
A
Effect of $\Psi_0(r)$
B
C
Effect of $\Psi_0(R)$
D
E
Combined Effect
F
G
0
k$_y$ (2Å^{-1}/Division)
y (0.5Å/Division)
k$_x$ (2Å^{-1}/Division) x (0.5Å/Division)

Figure 5.2

k-Space Maps at k = 9.6Å^{-1}
I
II
III
IV
x-y Slice at z=0.00Å
V
x-y Slice at z=2.26Å
A
Fixed Analyzer
B
Moveable Analyzer
θ = 0°
φ = 0°
C
Moveable Analyzer
θ = 45°
φ = 0°
D
Symmetry-Averaged Moveable Analyzer
0
k$_y$ (2Å^{-1}/Div.)
k$_x$ (2Å^{-1}/Division)
x (1Å/Division)
y (1Å/Division)

Figure 5.3

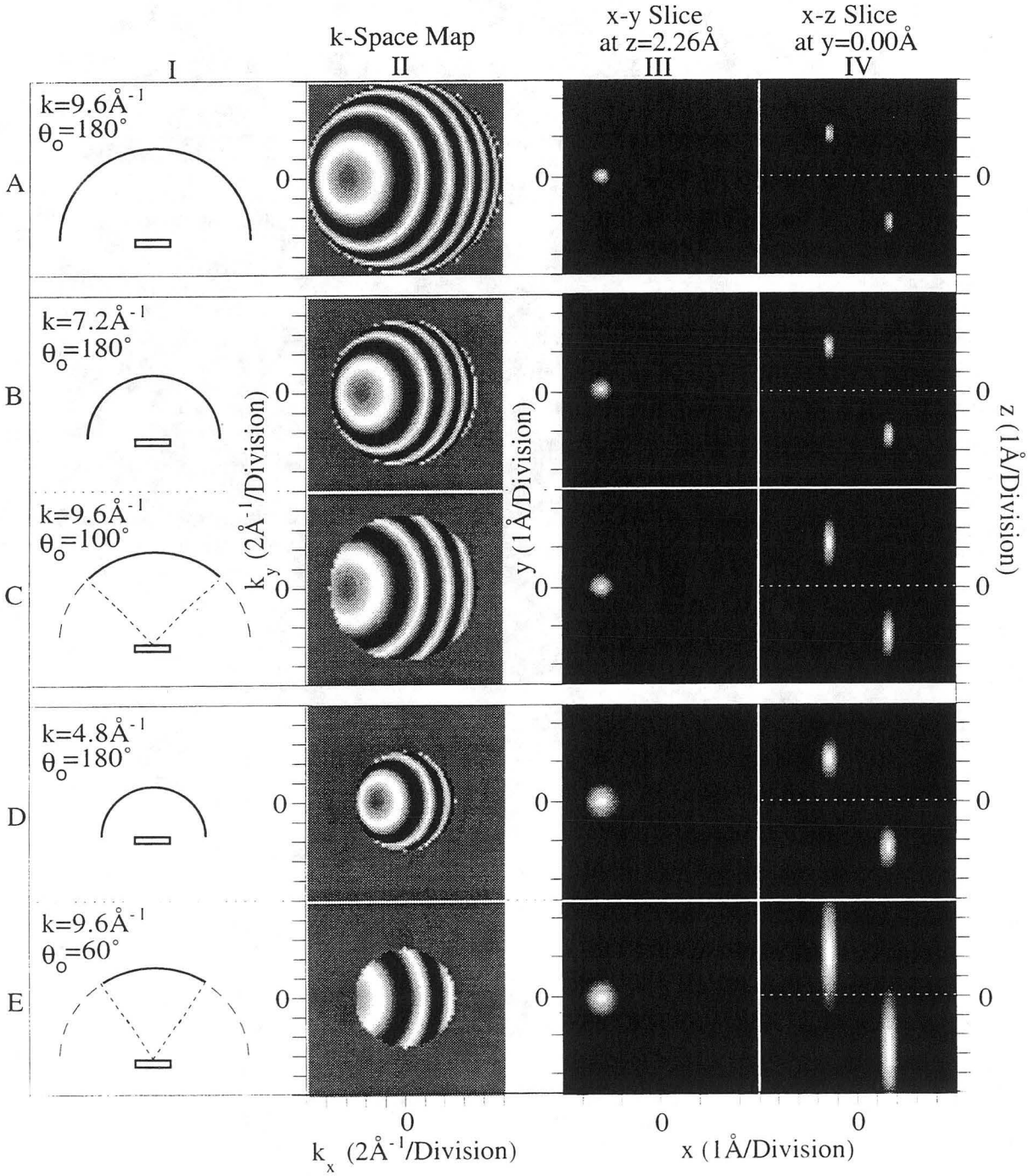
k-Space Map
x-y Slice at z=2.26Å
x-z Slice at y=0.00Å
I
II
III
IV
A
B
C
D
E
k=9.6Å^{-1}
θ$_o$=180°
k=7.2Å^{-1}
θ$_o$=180°
k=9.6Å^{-1}
θ$_o$=100°
k=4.8Å^{-1}
θ$_o$=180°
k=9.6Å^{-1}
θ$_o$=60°
k$_y$ (2Å^{-1}/Division)
y (1Å/Division)
z (1Å/Division)
k$_x$ (2Å^{-1}/Division)
x (1Å/Division)
0

Figure 5.4

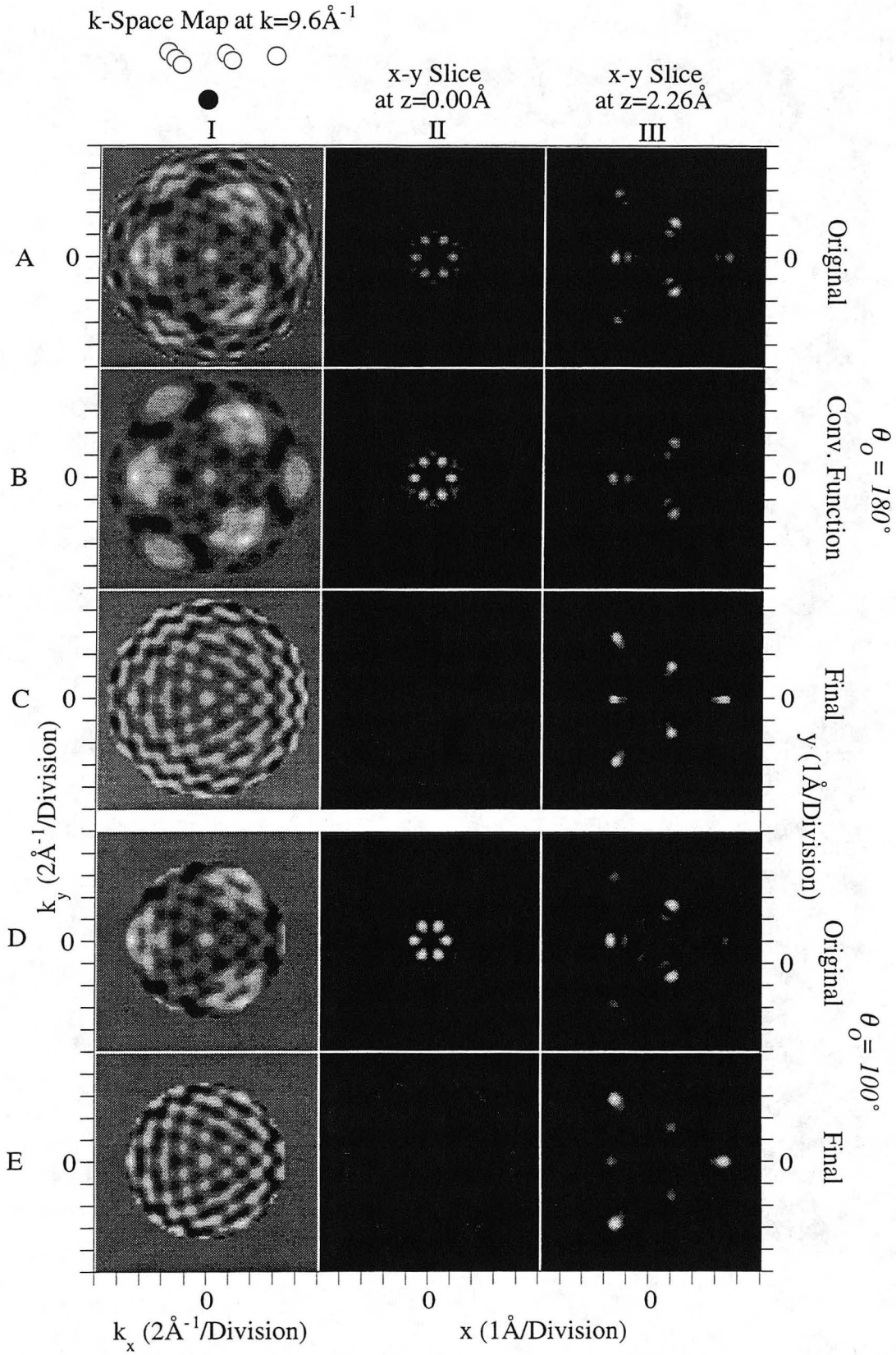
k-Space Map at k=9.6Å^{-1}
I
x-y Slice at z=0.00Å
II
x-y Slice at z=2.26Å
III
A
B
C
D
E
0
Original
Conv. Function
Final
Original
Final
θ_O = 180°
θ_O = 100°
k_y (2Å^{-1}/Division)
y (1Å/Division)
k_x (2Å^{-1}/Division)
x (1Å/Division)

Figure 5.5

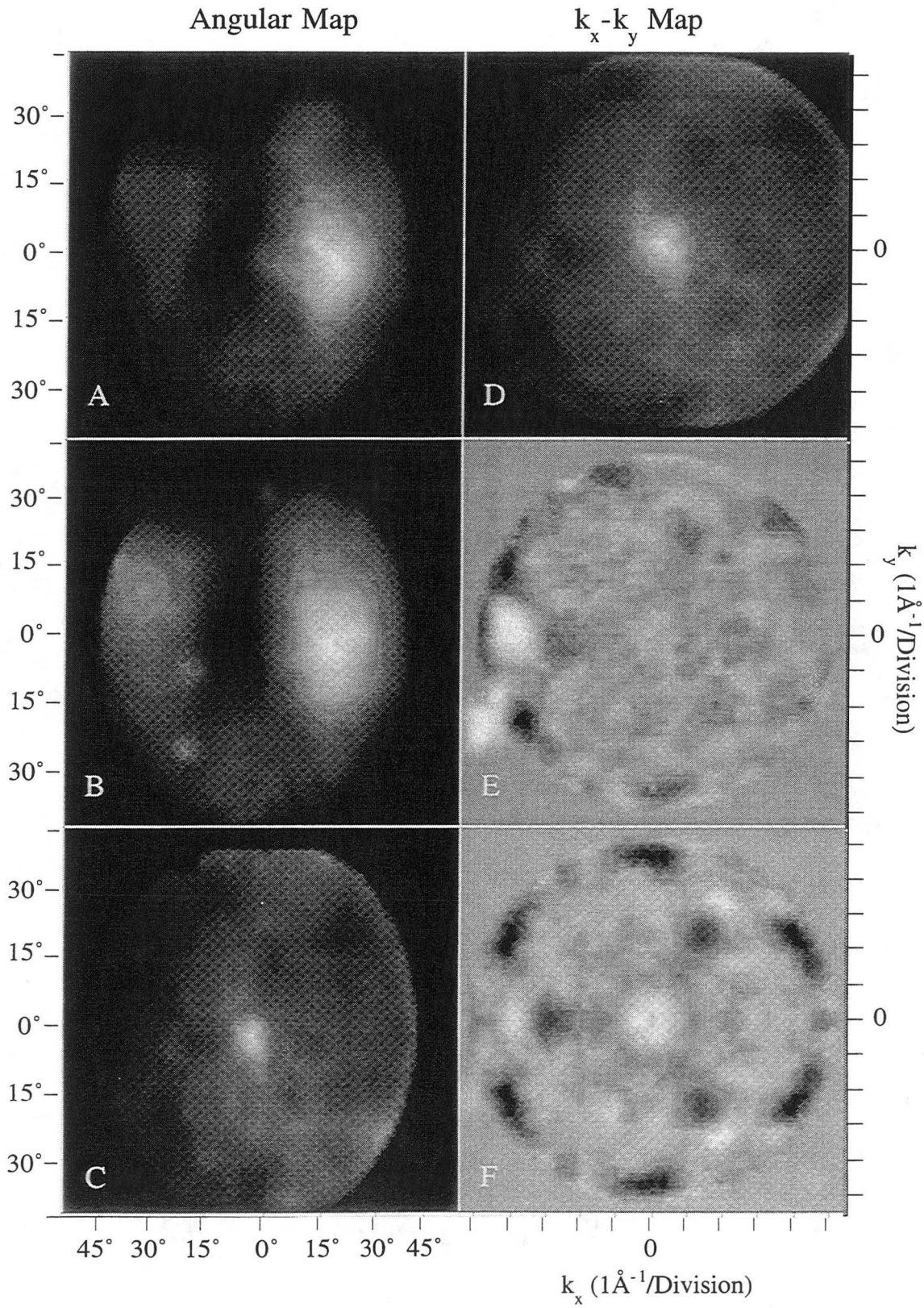
Angular Map
k_x-k_y Map
30°
15°
0°
15°
30°
A
D
B
E
C
F
45° 30° 15° 0° 15° 30° 45°
0
k_x (1Å^{-1}/Division)
k_y (1Å^{-1}/Division)

Figure 5.6

x-y Slice
at z=0.00Å
x-y Slice
at z=2.26Å
x-y Slice
at z=4.52Å
x-y Slice
at z=6.79Å
I
II
III
IV
V
A
k-Space Map
at 9.6Å-1
B
C
0
0
0
0
0
0
0
0
ky (1Å-1/Division)
kx (1Å-1/Division)
x (1Å/Division)
y (1Å/Division)
Experiment
Theory

Figure 5.7

Chapter 6

PHOTOELECTRON INTERFERENCE OF PT(111) FROM 6.0 TO 12.2A^{-1}

Abstract: A fully reduced experimentally-measured set of electron intensity patterns obtained from the Pt $4f_{5/2}$ photopeak of the (111) surface of platinum are presented. The set is compared to a simple theoretical model which accounts for many of the major features in the patterns and allows for a relationship to be made between electron scattering and holographic imaging. The theory also successfully models previously obtained multiple wavenumber imaging results for eight patterns from k=8.8 to 10.2 Å^{-1}.

I. Introduction

The measurement of electron intensity is used widely as a technique for making structural determinations of single crystal surfaces and surface systems. The advantages of using chemically specific electrons as localized sources for these studies is multifold, and is now fully appreciated in a variety of existent and new applications. Our interest in this area involves the understanding of how the structural information is stored and retrieved from the measured interferences. Such knowledge will be necessary for continued success of the techniques employing these electrons. In Chapters 2, 3, and 5, portions of a measured platinum (111) data set were used as examples for electron scattering in single crystals [1-3], and the entire set will be presented here. By pursuing a

well-understood system like platinum, the known structural information can be compared to its representation in a more complex manner as the interference of electrons collected above the sample.

Our intentions in this study are much more straightforward than the detailing of all the complexities of the problem, which would result in a full description of the measured results or, at best, a multi-dimensional fitting scheme. Knowing that the structural determination algorithms are fundamentally based on the simplest models of electron scattering in solids, the focus has been similarly directed at how simply the experimental data can be modeled. Although this approach is inappropriate for high-precision structural determinations, it serves well in cases where correct approximate structures are desired to answer questions without the need for a more time intensive iterative fitting approach.

Our past work with this platinum system has addressed the applicability of collected interference patterns as effective holograms for use in structural studies. Upon the suggestion by Szöke that a photoemitted electron wave in solids acts as a source wave and the scattered waves become object waves as in a holography experiment [4], Barton subsequently developed a theoretical formalism for testing the hypothesis [5,6]. With this in mind, we can effectively devise a premise for the work that follows in this chapter. The goal is to create a hologram we fully understand and can compare to the data. With such a complete data set, we have the unique ability to examine measured effects over a wide range of wavenumber. An exact theoretical fit of the data is often too far removed from the holographic process for us to gain sufficient insight about direct image formation. By examining the corresponding results from simple models, however, we can learn how the images form, what to expect from the data, and the best parameters to use for successful experiments. Additionally, the model can be used to reproduce results similar to those already obtained in Chapter 3, and to directly answer questions about the experiment which were previously incompletely understood.

II. Experimental

The platinum (111) crystal used in this experiment was prepared by sputtering for one hour in argon at $1x10^{-5}$ torr, followed by resistive annealing at 850° C for 3 minutes. This produced a clean, ordered surface as determined by XPS spectra. The crystal had been characterized earlier by LEED and oriented by Laue diffraction. Normal orientation of the crystal with respect to the analyzer was done using valence band photoemission. An energy-selective ellipsoidal mirror analyzer [19] was used for all spectra taken in this experiment, which was conducted on the IBM U8 beam line [20] at the National Synchrotron Light Source. In this analyzer, the sample was placed at one focus of an ellipse with the detector behind the other. An ellipsoidal electrostatic mirror, used as a low-pass electron energy filter, faced both the sample and detector. One hemispherical grid in front of the sample was used for retardation, while another in front of the detector acted as a high-pass energy filter. The detector consisted of a video camera arranged behind microchannel plates and a phosphor screen, collecting data at a rate of 30 frames per second in a 512x512 pixel array. The angular acceptance of the analyzer was ~84°, with a typical energy resolution of 0.3 eV and angular resolution of 1/4°. Photons from the U8 monochromator were used in the range from ca 200-600 eV, the energies required for this experiment.

For the measurements, Pt $4f_{5/2}$ electrons were monitored for each photon energy selected. Electron angular distribution patterns taken at the high-energy side of the photopeak were used for background normalization and for correction of the analyzer through-put function. Nine patterns from $k = 7.8Å^{-1}$ to $12.0Å^{-1}$ with wavenumber separation $0.6Å^{-1}$ were taken at the first sample position . The sample was then removed, cleaned, and returned to the same position where 24 additional patterns were measured, and the combined total had wavenumbers ranging from $6Å^{-1}$ to $12Å^{-1}$ with a step size of $0.2Å^{-1}$. Typical measuring times were about 1 hour for the photopeak and 2 hours for

the background, although later the background patterns were found to be practically interchangeable, potentially reducing the measuring time considerably.

The experimental data reduction process is described completely in reference 3 and briefly here. The two dimensional photopeak array at a single kinetic energy is divided by the background, resulting in an angular space map of the total intensity due to the atomic and interference portions of the ejected electrons. The intensities at the given angles are then mapped to their corresponding momentum space (k_x, k_y) coordinates, after centering and correcting for the 0.75 aspect ratio of the CCD video camera. No angular corrections were made to the data to correct for analyzer distortions. Convolution with a Gaussian of σ=0.04 and subsequent division is performed on this data prior to a 3-fold symmetry averaging operation. This last pattern, retaining a total opening angle of about 70°, is the one used for the final symmetric transformed images.

III. Theory

The theory employed here has been previously described [3], and a more detailed description may be found within that reference. The physical phenomenon used for structure involves the variation of electron intensity over angle due to the interference between the probability amplitude for the photoemitted electron to travel from the ionized atom to the detector and that for the electron to scatter from a nearby atom. We use a simple single scattering model employing linearly polarized photons which generate an oriented outgoing p-wave (l=1) to approximate the l=2,4 combination predicted for emission from an l=3 initial state [9]. This is represented by spherical waves of the form $\exp(ikr)/ikr$ in proportion to the incident wave amplitude, emitted from the scattering cores. To make the model even more ideal, only the isotropic l=0 scattering atom phase shift was chosen in order to account for the dominant contribution in the calculation of the scattering factor. This is done not to produce an exact result, but instead to preserve

the simplicity and more intuitively straightforward spherical form of the scattered waves while maintaining the major features in the calculated patterns. The single scattering equation which governs the scattering process and gives the total amplitude, Ψ_T, can be expressed as follows:

$$\Psi_T(\boldsymbol{R}) = A(\boldsymbol{R}) \cdot \frac{e^{ik|\boldsymbol{R}|}}{ik|\boldsymbol{R}|} \cdot \left(1 + \sum_n \frac{A(\boldsymbol{r_n})}{A(\boldsymbol{R})} \cdot f(\boldsymbol{k} \cdot \boldsymbol{r}_n) \cdot \frac{e^{ikr_n}}{ikr_n} \cdot e^{-i\boldsymbol{k} \cdot \boldsymbol{r}_n} \right) \tag{1}$$

where A represents a complex angular dependent non-structural factor and f represents the scattering factor. The interference portion is obtained from the total measured intensity at the detector at $\boldsymbol{R}$ by removal of the intensity due to the reference wave, according to:

$$\chi(\boldsymbol{R}) = \frac{I_T(\boldsymbol{R}) - I_0(\boldsymbol{R})}{I_0(\boldsymbol{R})}, \tag{2}$$

which gives

$$\chi(\boldsymbol{R}) = \sum_n C_n(\boldsymbol{R}) \cos\left[kr_n(1-\cos\theta_n) + \phi_n\right], \tag{3}$$

where C($\boldsymbol{R}$) is an angle-dependent combination of structural factors, θ_n is the angle between the direction from the emitter to the scattering atom and that to the detector, and ϕ_v represents the scattering atom phase shift.

For this study, only one emitter in an entirely forward scattering 80 atom cluster was used in the simulated electron angular distribution patterns. The forward scattering cluster was used because the measured intensities for forward scattering are much larger in this system and the angular transforms are much more sensitive to this intensity. The ε-vector was directed 45° from the sample normal and the azimuth 15° from the 100 direction, as in the experiment. For the final symmetric patterns these calculated images

were three-fold symmetry-averaged identically to the experimental set. A background based on the reference wave was removed, leaving only the interference of the reference and scattered waves, $\chi(k_x,k_y)$. No Fourier filtering operations were done on the theoretical calculations. This approach underscores the domination of the hologram by atomic geometry information, and not these other factors.

All other higher theoretical constructs were not included in this calculation, some of which include: scattering factors, multiple scattering, inner potentials, multiple initial states, temperature, multiple emitters, the acceptance angle, vibrational and inelastic damping, mean free path attenuation. Additionally, no fitting was done. This is not because of any wish to deny the importance of these factors in exactly describing a measurement, but instead to simplify the problem and allow for efficient testing while keeping the model intuitively uncomplicated.

The reasoning behind this simple theory is that the holographic theory employed is one based on simple point sources and a spherical source wave. As has been well documented [10-13], the effects of the full scattering theory required for accurate fits of the data are deleterious to the pure holographic images. These details are in fact a necessary component of the more quantitative ARPEFS technique. Distortions, artifacts, and other undesirable features can appear in the final transformed result. More importantly, trying to remove or directly manipulate the data to account for theoretical known distortions is fundamentally counterproductive for a process which presupposes the ability to identify the unknown. Anything that this technique will retrieve from an unknown system will also have to be successful on the simplest of systems. We cannot hope to draw information from an experimental data set which has been modified to the point where it no longer contains the information sought. This theory gives us a convenient reference for comparison to the measured data and to ideal holograms.

IV. Results

The fully reduced three-fold symmetry-averaged experimental data set is plotted on the left of the columns shown in Figures 6.1 and 6.2. In the lower left corner of each individual panel is noted the wavenumber of the electrons measured in inverse angstroms. Alongside each experimental data panel is a corresponding simple theoretical calculation at the corresponding wavenumber. All panels have been plotted in the same k-space range, that of the highest energy pattern at k=12.2Å^{-1}. The pattern at k=12.0Å^{-1} could not be retrieved in its entirety but is included for completeness.

Figure 6.3 compares the 3-dimensional image obtained from the eight patterns from k=8.8 to 10.2Å^{-1} studied in Chapter 3 to the simple theoretical result. On the left in panel A is the experimental result, and the right, panel B, is its theoretical partner calculated from the eight patterns shown. Panel C shows the result if only a simple spherical wave theory is used, including a spherically symmetric emitter and no scattering factor. Panel C is included to show that the major characteristics of the transformed result are entirely due to the interference, not the nature of the source wave or scattering factor. Panel D shows the ideal image from the forward scattering atoms from a platinum (111) face.

V. Discussion

The full Pt(111) data set clearly reveals the process that occurs in any photoelectron 'diffraction' (interference) experiment. It gives the viewer an idea of how these electron patterns change with kinetic energy in a way which can be followed throughout the set. Since we know they were all generated from the same source wave in the same sample, we can observe how the kaleidoscopic changes occur. In this medium energy range, from 137-567 eV, it is evident that these patterns are dominated by features which we can understand in terms of the most basic principles of electron scattering in solids. In fact, the simplicity which prevails is reassuring.

We have included a simple theoretical comparison because its appropriateness to this technique. The reason this theory is employed so readily is because its relationship to the holographic images formed is fully understood. If the data can be compared to these simply calculated patterns, the origin of the generated images can be fully realized. Upon close inspection, almost all of the features noted in the data are reproduced in some form by the theoretical model, with the notable exception being the group of patterns from about k=7.6 to 8.2Å^{-1}. Admittedly, the experimental data had Gaussian removal of broad features through convolution, but the order of the remaining features agrees in nature to those obtained in the calculation. Although dominated by forward scattering, none of these features is due to 'forward focusing', since the theory employed uses purely isotropic scattering. In reality, the scattering factors of platinum in this wavenumber range are not as far from isotropic as in lighter elements. Additionally, using the simple theory lets us follow the formation of the primary interferences which eventually generate holographic images. In fact, a pattern can be easily 'dissected' in order to determine how a single layer contributes to the whole, and even to surmise the contribution of one particular atom in relationship to the total collected interference pattern.

The differences between the simple theory and experimentally obtained patterns is expected and in favorable cases can be described using the theoretical constructs originally avoided. The primary problem is the nature of the source wave, since in this energy range the incomplete form of the scattering factor for this system is not so detrimental. Our symmetrically inappropriate p-wave does not sufficiently model the asymmetry-parameter modulated source wave which exists in theory [9], and this may explain some of the inverted phase effects noted with radial distance in some patterns. The source wave angular momenta-related distortions are described in more detail elsewhere [14, 15]. Another obvious difference is the previously mentioned discrepancy of the patterns from k=7.6 to 8.2 Å^{-1}, which do not agree with the theory. Multiple

scattering may also be the cause of some of the poor agreement here and at the lower energies [16, 17].

One of the biggest successes of the simple theory is its agreement with the three-dimensional images obtained in the multiple-wavenumber calculation comparison of Figure 6.3, panels A and B. In this figure, we note the expected poor z-resolution, but also we can see that the second layer is weaker in intensity that the third and first layers. This is an imaging effect related to the amount of information recorded for that layer in the measured patterns in this wavenumber range [18] and the opening angle of the analyzer. The same lack of artifacts and identical highlighted atoms shows that the model chosen and the previous experimental results are closely related. In fact, the central intensity component is also reproduced in the theory, although it is not expected nor an appropriate conclusion to assume that the emitting atom images itself.

There are a variety of other questions which the simple theory now allows us to answer. In the multiple-wavenumber calculations, patterns below k=8.8 $Å^{-1}$ could not be used because they did not improve the image. Although not shown in detail here, the theoretical model answers this question by showing that at this opening angle, it is impossible to obtain an image of the nearest neighbors above the emitter below this value. There is not enough information measured from the interference to reproduce the image of the nearest neighbors upon transformation. On the higher energy side, the experimental patterns above k=10.2 $Å^{-1}$ (396 eV) favor images of atoms directly above the emitter when transformed. This does not happen in the simple theory and is attributed it to Debye-Waller damping at higher wavenumbers and our experimental limitations. Above k=10.2$Å^{-1}$, we left the best flux range of the x-ray monochromator employed with a significant decrease in signal-to-noise. The lack of exact angular corrections becomes more important. Atoms further from the emitter give smaller oscillations, and the oscillations due to atoms directly above the emitter are comparatively dominant. After image integral transformation, those atoms dominate in the final real-space image.

In both theory and experiment, the z-resolution is limited by the diffraction limit imposed by the opening angle of the analyzer in this energy range. The images are elongated into cigar-type shapes. It is important to note that in this case the elongation is not due to the scattering factor, but rather the experimental geometry. The resolution should be expected to improve slightly with the addition of patterns from more wavenumbers over a wider range of electron kinetic energy [6]. Atoms in backscattering configurations will tend to benefit more from the phase-summing technique, since the phase for these will vary more over a shorter range of wavenumber.

It is also important to remember that these patterns are specific to the analyzer employed [3]. In this case, the ε-vector is always fixed relative to the atoms in the crystal. This tends to break some of the symmetry imposed by the crystal lattice and impose the symmetry due to the source wave. It also forces a constant source wave relative to the atoms in the crystal. In configurations where the ε-vector remains fixed relative to the detector and varies with respect to the atoms in the crystal, or in other combined variations, the measured results may prove to be different.

VI. Conclusion

In this chapter, a full experimental data set obtained for the platinum (111) surface for electrons with wavenumbers k=6.0 to 12.2$Å^{-1}$ was presented. Along with the data, a simple single-scattering theoretical calculation was included for direct comparison to the experimental results. This was done because the holography is well understood for the ideal case. Previous experimentally obtained multiple-wavenumber results were explained using the simple theoretical model. The results of the comparison allow us to better understand the process of photoelectron interference and how it relates to holographic imaging using collected electron interference data.

References

[1] B.L. Petersen, L.J. Terminello, J.J. Barton and D.A. Shirley, Chem. Phys. Lett. 213 (1993) 412. (See Chapter 2)

[2] B.L. Petersen, L.J. Terminello, and D.A. Shirley, Chem. Phys. Lett. 220 (1994) 46. (See Chapter 3)

[3] B.L. Petersen, L.J. Terminello, and D.A. Shirley, to be published. (See Chapter 5)

[4] A. Szoke, in *Short Wavelength Coherent Radiation: Generation and Applications*, edited by D.T. Atwood and J. Bokor (AIP Conf. Proc. 146, New York, 1986).

[5] J.J. Barton, Phys. Rev. Lett. 61 (1988) 1356; J.J. Barton, J. Electron Spectrosc. 51 (1990) 37.

[6] J.J. Barton and L.J. Terminello, in Structure of Surfaces III, Milwaukee, edited by S.Y. Tong, M.A. Van Hove, X. Xide, and K. Takayanagi (Springer-Verlag, Berlin, 1991) 107; J.J. Barton, Phys. Rev. Lett 67 (1991) 3106.

[7] D.E. Eastman, J.J. Donelon, N.C. Hien and F.J. Himpsel, Nucl. Instrum. Methods 172 (1980) 327.

[8] F.J. Himpsel, Y. Jugnet, D.E. Eastman, J.J. Donelon, D. Grimm, G. Landgren, A. Marx, J.F. Morar, C. Oden, R.A. Pollack, J.Schneir and C. Crider, Nucl. Instrum. Methods Phys. Res. 222 (1984) 107.

[9] S.M. Goldberg, C.S. Fadley, and S. Kono, J. Electron Spectrosc. Related Phenom. 21 (1981) 285.

[10] D.K. Saldin, G.R. Harp, B.L. Chen and B.P. Tonner, Phys. Rev. B 44 (1991) 2480.

[11] G.R. Harp, D.K. Saldin, X. Chen, Z.-L. Han and B.P Tonner, J. Electr. Spectros. Relat. Phenom. 57 (1991) 331.

[12] D.K. Saldin, G.R. Harp, and B.P. Tonner. Phys. Rev. B 45 (1992) 9629.

[13] J.J. Barton and L.J. Terminello, Phys. Rev. B 46 (1992) 13548.

[14] D.K. Saldin, G.R. Harp, and B.P. Tonner. Phys. Rev. B 45 (1992) 9629.

[15] J.J. Barton and L.J. Terminello, Phys. Rev. B 46 (1992) 13548.

[16] J.J. Barton, S.W. Robey, and D.A. Shirley, Phys. Rev. B 34 (1986) 778.

[17] A.P. Kaduwela, D.J. Friedman, and C.S. Fadley, J. Electron Spectrosc. Relat. Phenom. 57 (1991) 223.

[18] B.L. Petersen, L.J. Terminello, D.A. Shirley, to be published. (See Chapter 4)

Figure Captions

Figure 6.1. *Full Pt(111) data set with theoretical comparison, k=6.0 to 9.0Å^{-1}.* The left column presents the three-fold symmetry averaged experimental $\chi(k_x,k_y)$ The calculated theoretical patterns are shown to the right of each pattern. The wavenumber of each set is shown in the lower left corner of the experimental pattern.

Figure 6.2. *Full Pt(111) data set with theoretical comparison, k=9.2to 12.2Å^{-1}.* The left column presents the three-fold symmetry averaged experimental $\chi(k_x,k_y)$ The calculated theoretical patterns are shown to the right of each pattern. The wavenumber of each set is shown in the lower left corner of the experimental pattern.

Figure 6.3. *Three-dimensional volume comparison.* Panel A shows the experimental result from a multiple-wavenumber analysis using eight patterns from k=8.8 to 10.2 Å^{-1}. Panel B shows the theoretical comparison using the corresponding eight calculated patterns. Panel C shows the ideal theoretical image obtained with no included source wave or scattering factor components. Panel D shows a model image for the forward scattering atoms of the platinum (111) system, included for comparison.

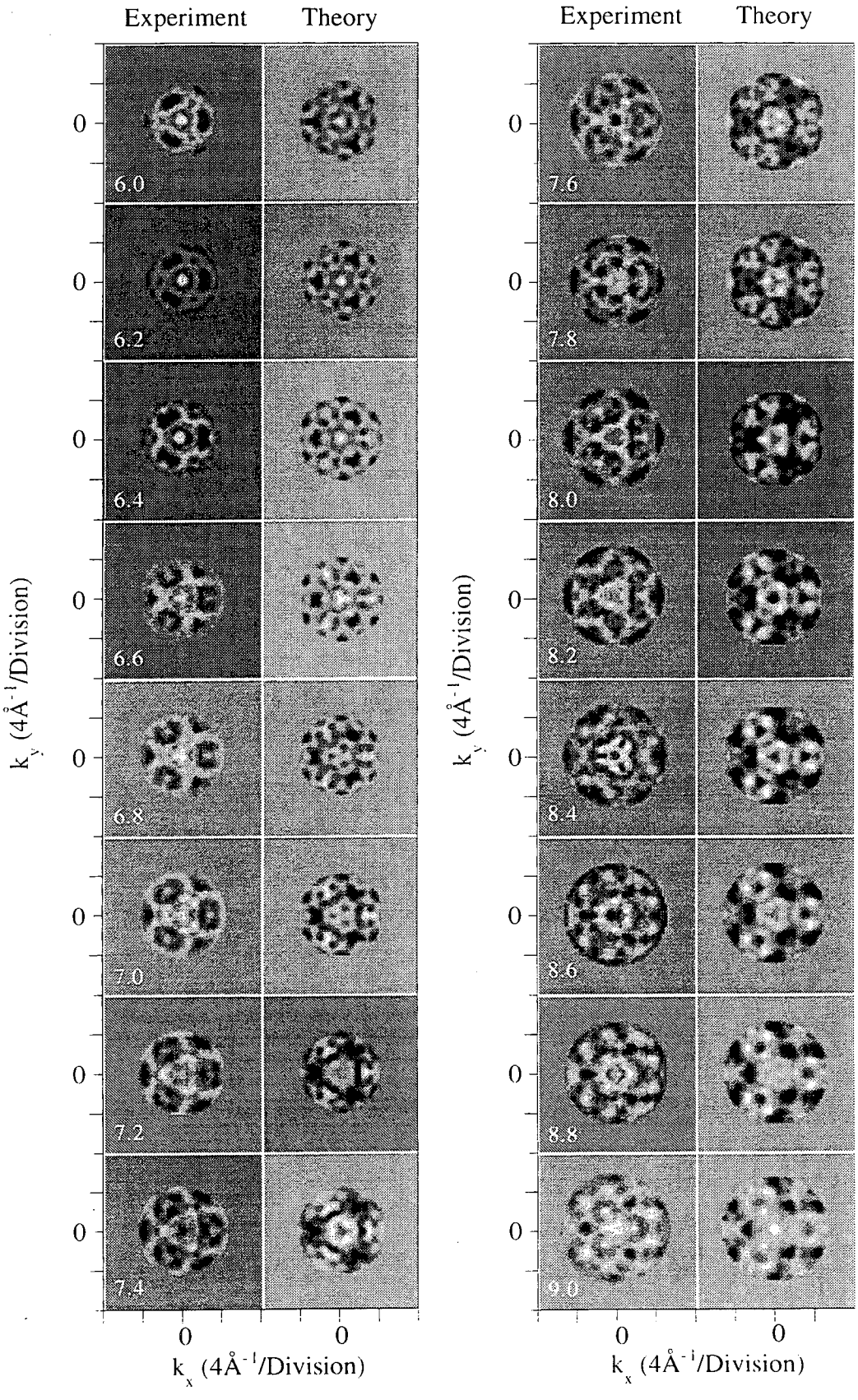
Experiment
Theory
Experiment
Theory
6.0
6.2
6.4
6.6
6.8
7.0
7.2
7.4
7.6
7.8
8.0
8.2
8.4
8.6
8.8
9.0
0
k_y ($4Å^{-1}$/Division)
k_x ($4Å^{-1}$/Division)

Figure 6.1

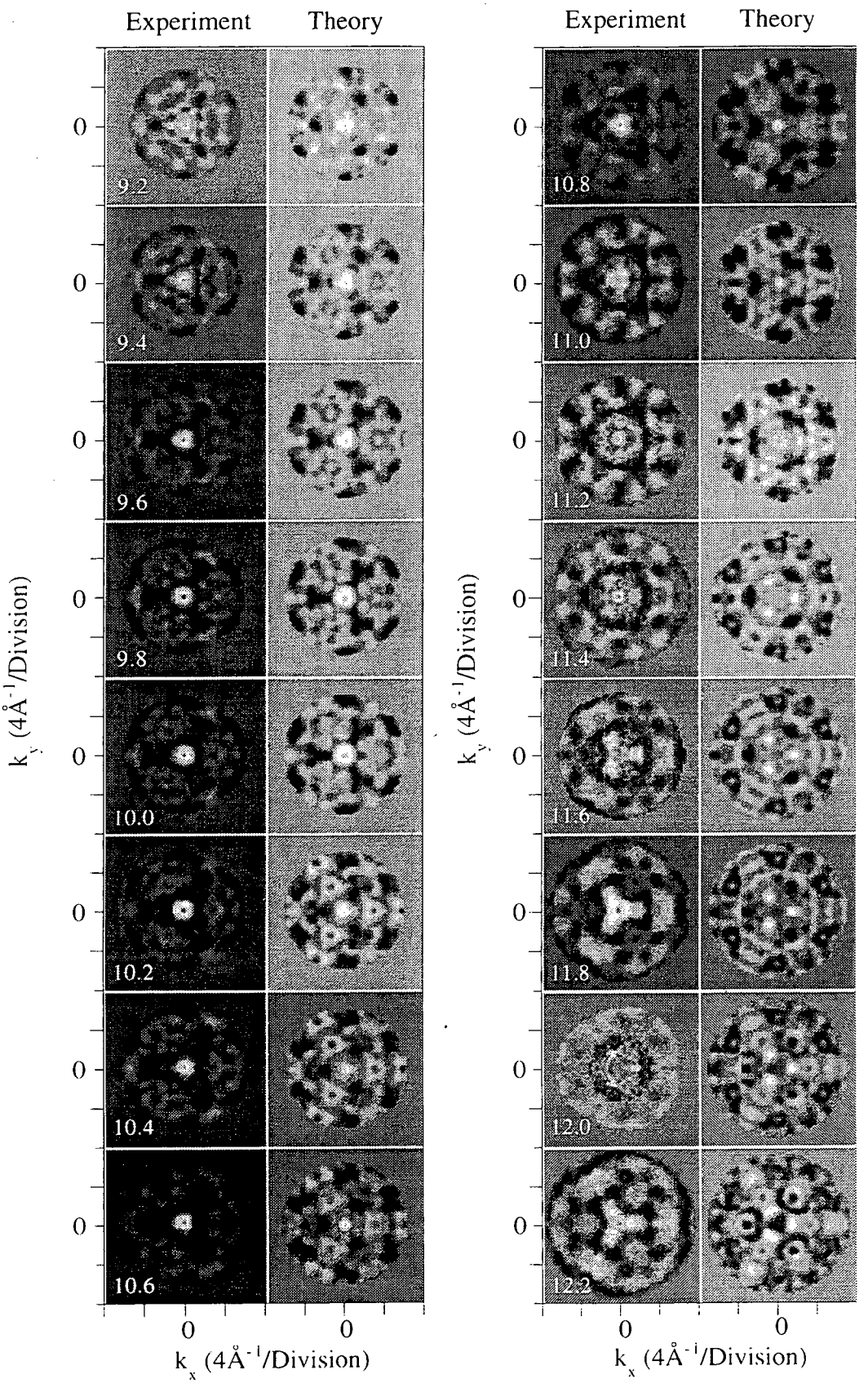
Experiment
Theory
Experiment
Theory
9.2
9.4
9.6
9.8
10.0
10.2
10.4
10.6
10.8
11.0
11.2
11.4
11.6
11.8
12.0
12.2
0
k_y (4Å^{-1}/Division)
k_x (4Å^{-1}/Division)

Figure 6.2

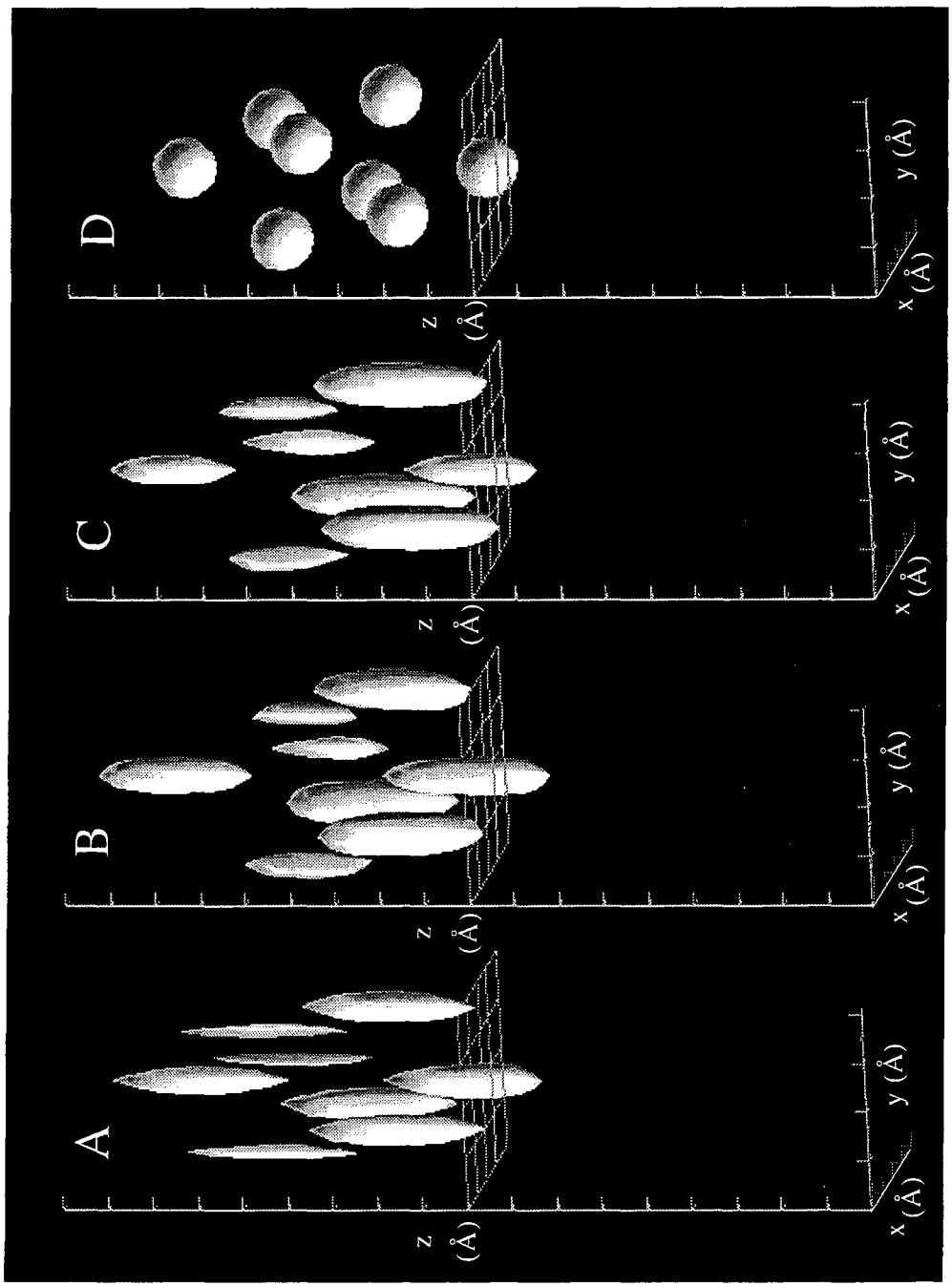

Figure 6.3

Chapter 7

A SECOND METAL SYSTEM: COPPER(001) IMAGED USING PHOTOELECTRON HOLOGRAPHY

Abstract: A revised analysis scheme is applied to a previously published data set in order to improve the reported result. Four atoms are found one layer above the emitter at the appropriate location although shifted by 0.2Å. To strengthen this analysis, a comparison is made with a simple model which gives a similar result. A theoretical study is also done to show why a holographic analysis scheme tends to preferentially image forward scattering atoms if they are present in an imaged system.

I. Introduction

The technique employing electron interference for creation of holographic images of surface structure was suggested by Szöke [1] and later formalized by Barton [2]. These images use the combination of the inherent reference wave of a photoemitted core-level electron or core-like electron and the scattered waves from surrounding atomic cores to generate an interference pattern, which is collected using an angle and energy-selective electron spectrometer. Photons are used to emit electrons with kinetic energies ranging from 100 to 600 eV. The resulting pattern can be transformed mathematically over both angle and wavenumber in order to generate an angstrom-resolution image of surface structure, represented as real space intensity at specific locations surrounding the

emitter. Since it requires no theoretical comparison, this technique offers a direct method of imaging a surface for structural determination.

In Chapters 2 through 6, studies have been conducted to establish and verify this technique based on a full platinum (111) data set [3-7], which allowed for a careful study of its application to a real system. It was possible to image forward scattering atoms of the hcp lattice in both the single and multiple-wavenumber cases, and these results were verified with simple theoretical models. The work described has led to a more generalized and also more confident analysis procedure which can be used to obtain higher quality images and heighten the confidence of the images obtained. The success has been due to the ability to understand the source of the interference patterns and how holographic images form from these patterns. With this standardization, it is possible to apply the technique to any other system while maintaining consistency and directness.

In the current study, attention is focused on a second system, the (001) surface of copper. Nine interference patterns were collected using electrons emitted from the copper 3p initial state. This system has been studied in detail previously [8], but based on the platinum work it is possible to make a reassessment of those results. In truth, copper is a much more difficult system to study than platinum using this technique due to its more anisotropic scattering factor. The anisotropy distorts the interferences necessary for holographic imaging when compared to that expected for an ideal holographic case. This distortion limits the uncorrected imaging capability of such a measurement, but does not make it impossible. Here, using the same analysis procedure as applied in the platinum case, correct images of the nearest neighbor copper atoms are shown directly above the emitter and a simple theoretical comparison which verifies those results is provided.

Because clean metal surfaces have identical emitting atoms in all layers, there have been some questions raised [9] as to the source of the images obtained. Because there are twin images above and below the z=0 plane, the images above any emitter may be identical to those below the emitter. In the case where the twin images are removed,

the question arises as to whether the final images are due to back or forward scattering atoms. In the case of back scattering, the images would consist of those atoms which lie below the emitter. This would be an appropriate technique to use in a situation where adsorbate species resides in an unknown location on top of a substrate. In the case of forward scattering, the atoms which are imaged lie above the emitter and the emitter is thus buried beneath the topmost surface layers. This technique would be applicable to studies of adsorbates too, but also to materials such as buried interfaces which require the ability to produce images of atoms surrounding and especially above the emitting atom of interest. In either case, back or forward, it is important to know which is being imaged for obvious reasons.

There are two commonly employed and fundamentally related techniques used to determine surface structure using energy and angular electron intensities measured in the hemisphere above the sample of interest. The first is angle-resolved photoemission fine structure, or ARPEFS [10], and the second is photoelectron holography [2]. ARPEFS initially involves measuring intensity over a specified range of wavenumber at a given angle. Photoelectron holography involves measuring intensities over many angles at a single wavenumber. Transforms are then done over the wavenumber, in the case of ARPEFS, or over angle, in the case of holography. The logical next step is to vary the angle in ARPEFS, and to vary the wavenumber in the holography studies. In both cases, the same information is being measured. The difference is in the treatment of the data.

ARPEFS is a technique that involves measuring data along a single axis, and the Fourier transform of these wavenumber oscillations, much like in the case of EXAFS [11,12], results in structural information. The peaks of the transformation appear at path length differences defined as $r_j(1-\cos\theta_j)$, where θ_j is the angle between a scattering atom center at r_j and the direction to the detector from the emitter. The oscillations dominate for a given scatterer whenever θ_j is 180°, which is the definition of direct back scattering. At the same time, when θ_j is 0°, or direct forward scattering, the path length difference is

zero and no path length difference can be recorded for any energy. To remove peaks at lower path lengths (which correspond to forward scattering atoms), ARPEFS analysts often filter the total intensity over wavenumber in order to remove the slowly oscillating features. All that remains is back scattering information, with the strongest information due to direct back scatterers. No directional information can be obtained in this technique without theoretical comparisons or by making similar measurements in different directions and taking full advantage of direct back scattering to locate repeated high intensity [13].

In photoelectron holography, the analysis is different. In this case, the data is a two-dimensional array. The first transform is done over k_x and ky using a holographic imaging integral of which a portion may be expressed as a two-dimensional Fourier transform [2]. But unlike ARPEFS, this transform has no predilection for direct back scattering and rather images all atoms equally, dependent only upon the intensity of the oscillations from a given scattering atom. Because forward scattering intensities often dominate measured interference patterns when both forward and back scatterers are present, holographically determined structures will be dominated by forward scattering images. By employing a multiple-wavenumber analysis scheme [14], the resolution of back scatterers will improve but the forward scatterers will still tend to dominate over the medium range of electron kinetic energy because of their greater intensity. If no forward scattering exists (as in ideal isotropic scattering), both forward and back scatterers will be almost equivalent in holography (back scattering intensity is slightly less due to distance from the detector), since the hologram treats all directions equally.

This chapter presents the results of multiple-wavenumber photoelectron holography to a copper (001) surface. It compares the experimental data measured at nine wavenumbers to a simple theoretical model, as well as the resulting images. Because copper has a strong scattering factor, it is used as an example to show how forward scattering dominates in holographic analysis schemes. The goal here is to

attempt to further understand electron scattering and its use as a tool for surface structural determination.

II. Copper (001)

A. Experimental

A copper (001) crystal was used in this experiment and was prepared by according to well-established cleaning and annealing procedures [15]. This produced a clean, ordered surface as determined by XPS spectra. Normal orientation of the crystal with respect to the analyzer was done using valence band photoemission. An energy-selective ellipsoidal mirror analyzer [16] was used for all spectra taken in this experiment, which was conducted on the IBM U8 beam line [17] at the National Synchrotron Light Source. In this analyzer, the sample was placed at one focus of an ellipse with the detector behind the other. An ellipsoidal electrostatic mirror, used as a low-pass electron energy filter, faced both the sample and detector. One hemispherical grid in front of the sample was used for retardation, while another in front of the detector acted as a high-pass energy filter. The detector consisted of a video camera arranged behind microchannel plates and a phosphor screen, collecting data at a rate of 30 frames per second in a 512x512 pixel array. The angular acceptance of the analyzer was ~84°, with a typical energy resolution of 0.3 eV and angular resolution of 1/4°. Photons from the U8 monochromator were used in the range from ca 200-600 eV, the energies required for this experiment. For these measurements, Cu 3p electrons were monitored for each photon energy selected. Spectra taken at the high-energy side of the photopeak were used for background normalization and for correction of the analyzer through-put function. Nine patterns from k = 8.0Å^{-1} to 11.2Å^{-1} with wavenumber separation 0.4Å^{-1} were measured. Typical measuring times were about 1 hour for the photopeak and 2 hours for the background, although the backgrounds were found to be interchangeable throughout this energy range.

B. Data Analysis

The initial measured data were collected as an angular map, or a hemispherical pattern projected onto a flat surface. In the second step, the pattern was converted from real space to momentum space coordinates, using the total energy of the outgoing electrons and the geometry of the analyzer. Corrections were also done to account for the pixel aspect ratio of the original data, but no analyzer angular transmission corrections were made.

Slow oscillations from the original (atomic) photoelectron final-state angular distribution, or the reference wave, and broad diffraction features tend to give false intensities near the center of the transformed image in real space. We overcame this problem by convoluting the data with a Gaussian and subsequently removing the convoluted function, in effect Fourier-filtering the data to remove low frequencies. The convoluted function was removed by division and subsequent subtraction of a unit field, leaving a pattern which oscillates around zero, reducing unwanted intensity at the origin after transformation. Edge effects from the division were minimized by circularly trimming the pattern edges to 90% of the original measured range. Finally, channels were summed, reducing the 512 x 512 pattern to 64 x 64 in order to increase the signal to noise ratio in each pixel and provide a good matrix density for Fourier transformation to an appropriate real space density. At this point the suitably processed data set was ready for application of the imaging integral transform.

Real-space images were obtained from these reduced two-dimensional k-space patterns by multiplying by a phase factor and applying a two-dimensional image integral transform according to:

$$U(r) = \iint_s \chi(k) e^{-ikr\cdot\hat{k}} d\sigma \qquad (1)$$

where $\chi(k)$ represents the reduced two-dimensional interference pattern. The result of this transform was a two-dimensional real-space x-y slice of intensity at the chosen z position, where the most intense features ideally correspond to atomic positions. For three-dimensional images, x-y slices over a specified range were stacked.

For improvement of z-resolution and reduction of multiple-scattering artifacts and twin images, a multiple-wavenumber analysis was employed. The process involved the combination of interference patterns taken with varying kinetic energies in order to step through k_z as well as k_x and k_y to approximate a complete three-dimensional image integral transform, expressed as:

$$M(r) = \sum_i F_i(k_i, \chi_i, r) e^{-ik_i r} \qquad (2)$$

which is a sum over each image reconstruction, F_i, computed from the individual patterns $\chi(k_i)$ measured at wave vector k_i, multiplied by exp(-*ikr*), the phase term that draws out the real, single-scattering contribution to the reconstruction as outlined in reference 14. After proper phasing and summation of the complex real-space intensities of single-wavenumber patterns transformed to a common three-dimensional real-space, the absolute square was taken of the resulting wave field. Since the peak intensities caused by integrating over angle and those caused by integrating over wavenumber do not coincide, double scattering, twin images, and most of the self-interference terms were suppressed.

The primary difference between the analysis scheme described here and the one previously employed [8] is the width of the Gaussian used in the convolution step. In this study, σ=0.02 is used as compared to $\sigma\approx$0.1. Additionally, no multiplication by a Gaussian function was used for reducing edge effects, instead the circular trimming process was employed. This had the effect of preserving more interference information across the patterns.

C. Theory

The theoretical analysis here has been described in more detail previously [6] and is based on a simplistic single scattering approach to electron scattering. The reason the simplest models are used in these studies is because the holographic analysis scheme used is based on straightforward interference of spherical waves. Rather than an exact fit of the data, it is more instructive for a technique that attempts to image surface structure directly to examine the images that will necessarily work in holography and see how experimental data compares to these models. At this stage it is not a scheme for a highly quantitative imaging procedure, but rather one that provides a clear image directly from straightforward measurements and analyses. It is also important not to insert any prior knowledge of the system into the analysis procedure. The data alone must give the images of interest, or the technique is not truly direct.

The physical phenomenon used for structure involves the variation of electron intensity over angle due to the interference between the probability amplitude for the photoemitted electron to travel from the ionized atom to the detector and that for the electron to scatter from a nearby atom We use a simple single scattering model employing photons which generate an spherical outgoing s-wave (l=0) to roughly approximate the l=0,2 combination predicted for emission from an l=1 initial state [18]. The scattering is represented by spherical waves of the form exp(*ikr*)/*ikr* in proportion to the incident wave amplitude, emitted from the scattering cores. The full plane wave scattering factor is used in these calculations. The equation governing the scattering of total amplitude, Ψ_T, is expressed as:

$$\Psi_T(\mathbf{R}) = \frac{e^{ik|\mathbf{R}|}}{ik|\mathbf{R}|} \cdot \left(1 + \sum_n f(\mathbf{k}\cdot\mathbf{r}_n) \cdot \frac{e^{ikr_n}}{ikr_n} \cdot e^{-i\mathbf{k}\cdot\mathbf{r}_n}\right) \qquad (3)$$

where f represents the full expression for the scattering factor and no source wave angular factor is used. After removal of the atomic portion, the interference terms, $\chi(\boldsymbol{R})$ in the case of an s-wave initial state reduce to:

$$\chi(\boldsymbol{R}) = \sum_n A_n(\boldsymbol{R}) \cos\left[kr_n(1-\cos\theta_n)+\phi_n\right], \qquad (4)$$

where θ is the angle between the direction from the emitter to the scattering atom and that to the detector, A is a nonstructural pre-factor, and ϕ represents the scattering phase shift.

An entirely forward scattering cluster with 110 atoms was used for the calculations. The cluster of atoms above the emitter was used because the measured intensities for forward scattering are much larger in this system and the angular transforms are much more sensitive to this intensity. This effect will be covered in more detail later in this chapter. A background based on the reference wave was removed, leaving only the interference of the reference and scattered waves, $\chi(k_x,k_y)$. Fourier filtering operations were done on the theoretical calculations using a Gaussian of width σ=0.02, similarly to the data.

It is worthwhile at this point to note the value of the simplicity of this calculation. No other higher theoretical constructs were included, some of which include: scattering factors, multiple scattering, inner potentials, multiple initial states, temperature, multiple emitters, the acceptance angle, vibrational and inelastic damping, mean free path attenuation. The point of this simple model is to highlight the assumptions which form the basis of the holographic procedure and compare it to an experiment. This will give us a realistic assessment of the direct nature of the technique.

D. Results

In this section a new version of the reduced experimental data and its theoretical counterpart are presented. The two-dimensional $\chi(k_x,k_y)$ patterns are shown along the top

row of Figure 7.1. Above the patterns are listed the corresponding kinetic energies in eV. All of these patterns are plotted on the same linear intensity scale. Below each experimental pattern is the result of the theoretical calculation at the particular kinetic energy of interest. Although by no means a perfect match, upon close inspection it is possible to find many related features in the two sets.

Figure 7.2 shows the corresponding three-dimensional comparison of experiment and theory, along with a two-dimensional x-y slice through the first layer above the emitter, at z=1.8Å. Panel A shows the experimental result, while panel B shows the single scattering result calculated from the nine theoretical patterns of Figure 7.1. The volumes are created as iso-intensity surfaces at 75% of the total intensity. It must be noted that these 3D images are not representative of the resolution of the technique, but rather chosen to highlight the most intense atoms directly above the emitter. In the upper right corner of each pattern is the two-dimensional slice, with crosses showing the expected location of the atoms. Atom images are outside of the true locations due to distortions of the scattering factor. However, there is significant agreement between experiment and theory with regard to the extent of this shift.

III. Forward Scattering Dominance in Holography

A. Theoretical Study

In order to show how forward scattering dominates the images formed in a photoelectron holography experiment, a simple example is employed in this section to show the effect. Using the theory of section IIB with full plane wave scattering factors, a model system is created which explores the greater intensity contribution of forward scattering atoms to the interference pattern and its resulting effect in holographic analysis schemes.

The model employed includes the five nearest neighbors to the emitting atom both above and below the z=0 plane. The five atoms above the emitter include the four atoms

in a fourfold pattern at z=1.8Å and the single atom directly above at z=3.6Å. Similarly, the five atoms below the emitter include the four atoms one layer below and the single atom two layers below, essentially a "twin" of the atoms above. A third system will include all 10 atoms in addition to the emitter, five above and five below. The atoms above the emitter constitute the 'forward scatterers', the atoms below constitute the 'back scatterers.'

To conduct the study, three test data sets will be created: back, forward, and combined. Using the same experimental parameters as used for the more thorough study above, interference patterns will be created which reflect the true experimental set. These will include nine patterns from k=8.0 to 11.2 $Å^{-1}$ (244 - 478 eV) with a step size of 0.4 $Å^{-1}$. A multiple wavenumber analysis will be conducted on each separate set and the final result help us establish how the holographic images form.

B. Results

In Figure 7.3 the results of the calculations are shown. In the first row, the backscattering result is shown. In the middle row are the forward scatterer patterns. Finally, in the third row the combined result is shown. The intensities between members of the same row are equivalent, but the columns each have a separate intensity scale. The combined result is essentially a combination of the first and second rows.

Figure 7.4 shows the iso-intensity surface result of all three test cases upon multiple-wavenumber analysis. Panel A shows the back scattered atoms (top row of Figure 7.3), below the plane of the emitter, as expected. Panel B shows the forward scattered atoms (middle row of Figure 7.3), above the plane of the emitter with much poorer z-resolution. Finally, panel C shows the result of the combined set (bottom row of Figure 7.3). All iso-surfaces are shown at 50% of the highest intensity within the volume.

IV. Discussion

This chapter discusses two topics, the improved holographic analysis of data measured from a copper (001) surface and the inherent ability of holography to preferentially image forward scatterers. Both topics are related, and copper serves as a good test system to show the forward dominance effect. However, the general condition of the anisotropic scattering factor which peaks in the forward direction makes this more of a general effect, not limited solely to copper.

The copper (001) surface analysis shows concisely the successful application of multiple-wavenumber photoelectron holography to an experimental system. It represents the improvement of a previously published result following directly from an improvement in the analysis procedure. The procedure changed as a result of experience with the creation of the pattern and a fundamental understanding of the holographic process. As an aid to achieve this understanding, the most basic models of electron scattering theory are used to determine how a hologram might form from non-ideal systems. This procedure helps to establish the parameters most appropriate for image creation and gives a model for comparison. The most important fact, however, is that it shows that the measured patterns are not that far from the simplest models. This means that direct holographic imaging of surface structure based on principles of single scattering, when properly applied, is readily achievable. Unknown structures may be determined using this technique.

In Figure 7.3 it is possible to learn a lot about the recording of the scattering process. From equation (4), we know that the oscillations over wavenumber will be related to the phase term $kr(1-\cos\theta)$. As described in the introduction, the $1-\cos\theta$ term will be maximum when $\theta = 180°$, the direct back scattering case, and minimum in the forward scattering case when $\theta = 0°$. As k is varied, the phase change will be much greater for back scattering atoms than for forward scattering atoms. This phase change will be recorded in the measured interference pattern, as evidenced in Figure 7.3. As we

observe the patterns of separate wavenumbers along the same row, the differences become apparent. For the back scattering case, patterns of different wavenumbers have distinctively different characteristics, which relate to the phase of the scattered wave changing significantly with small changes in wavenumber. For the forward scattering case, the patterns have similar features, varying slowly along the row. As the combined case also changes slowly and follows the middle row, it is not surprising that the forward scattering features dominate in Figure 7.4C. To relate this effect to the experimental result, notice also that the experimental data does not change rapidly with wavenumber throughout this range. This is a key to knowing that forward scattering dominates these images. The same effect can be noted in the previous studies with platinum [7].

ARPEFS and ARPEFS-related techniques are essentially insensitive to forward scattering atoms while holography is more sensitive to this region. This is because forward scatterers tend to give a more intense interference pattern. With regard to these electron scattering techniques, holography stands out with the ability to image the environment above a buried emitting atom. This may prove useful in cases such as buried interfaces or adsorbates which may require a sub-surface probe.

V. Conclusion

Using the established techniques for surface imaging using photoelectron holography, images were obtained for the four nearest neighbors above an atom in a copper (001) surface. The results of the analysis were compared with a simple theoretical model which must necessarily give the expected result. The obtained images were different from previously published results, but were confirmed by the simple theory. In addition, the dominance of forward scattering in holographic analyses was discussed in terms of a simple model which accounts for the anisotropic effects of the scattering factor. Photoelectron holography may be better suited for sub-surface imaging than

techniques which rely primarily on back scattering to obtain direct images of surface structure.

References

[1] A. Szöke, in *Short Wavelength Coherent Radiation: Generation and Applications*, edited by D.T. Atwood and J. Bokor (AIP Conf. Proc. 146, New York, 1986).

[2] J.J. Barton, Phys. Rev. Lett. 61 (1988) 1356; J.J. Barton, J. Electron Spectrosc. 51 (1990) 37.

[3] B.L. Petersen, L.J. Terminello, J.J. Barton and D.A. Shirley, Chem. Phys. Lett. 213 (1993) 412. (See Chapter 2)

[4] B.L. Petersen, L.J. Terminello, and D.A. Shirley, Chem. Phys. Lett. 220 (1994) 46. (See Chapter 3)

[5] B.L. Petersen, L.J. Terminello, and D.A. Shirley, to be published. (See Chapter 4)

[6] B.L. Petersen, L.J. Terminello, and D.A. Shirley, to be published. (See Chapter 5)

[7] B.L. Petersen, L.J. Terminello, and D.A. Shirley, to be published. (See Chapter 6)

[8] L.J. Terminello, J.J. Barton and D.A. Lapiano-Smith, Phys. Rev. Lett. 70 (1993) 599; J. Vac. Sci. Technol. B 10 (1992) 2088.

[9] C.M. Wei, I.H. Hong, P.R. Jeng, S.C. Shyu, and Y.C. Chou, Chem. Phys. Lett. 228 (1994) 513.

[10] J.J. Barton, C.C. Bahr, Z. Hussain, S.W. Robey, J.G. Tobin, L.E. Klebanoff, and D.A. Shirley, Phys. Rev. Lett. 51 (1983) 272.

[11] Edward A. Stern, Phys. Rev. B 10 (1974) 3027.

[12] P.A. Lee and J.B. Pendry, Phys. Rev. B 11 (1975) 2795.

[13] J. G. Tobin, G.D. Waddill, H. Li, and S.Y. Tong, Phys. Rev. Lett. 71 (1993) 4150.

[14] J.J. Barton and L.J. Terminello, in Structure of Surfaces III, Milwaukee, edited by S.Y. Tong, M.A. Van Hove, X. Xide, and K. Takayanagi (Springer-Verlag, Berlin, 1991) 107; J.J. Barton, Phys. Rev. Lett 67 (1991) 3106.

[15] C.C. Bahr, J.J. Barton, Z. Hussain, S.W. Robey, J. G. Tobin, and D.A. Shirley, Phys. Rev. B 35 (1987) 3773.

[16] D.E. Eastman, J.J. Donelon, N.C. Hien and F.J. Himpsel, Nucl. Instrum. Methods 172 (1980) 327.

[17] F.J. Himpsel, Y. Jugnet, D.E. Eastman, J.J. Donelon, D. Grimm, G. Landgren, A. Marx, J.F. Morar, C. Oden, R.A. Pollack, J.Schneir and C. Crider, Nucl. Instrum. Methods Phys. Res. 222 (1984) 107.

[18] S.M. Goldberg, C.S. Fadley, and S. Kono, J. Electron Spectrosc. Related Phenom. 21 (1981) 285.

Figure Captions

Figure 7.1. *Experimental and Theoretical Cu(001) Interference Patterns.* The top row shows nine experimentally measured and subsequently reduced interference patterns obtained from a Cu(001) surface. The bottom row shows the theoretical comparison, using a single scattering model with spherically symmetric initial state and a plane wave scattering factor, included for comparison.

Figure 7.2. *Experimental and Theoretical Cu(001) Iso-intensity Surfaces.* Panel A shows the three-dimensional volume view of the multiple-wavenumber result at 75% of the highest intensity. The inset is an x-y slice through the layer shown, at z=1.8Å above the emitter. Panel B presents the same view for the theoretical model, with the same corresponding x-y slice inset.

Figure 7.3. *Forward vs. Back Scattering Comparison Interference Patterns.* The top row shows nine patterns calculated for a Cu(001) surface of the five nearest neighbors below the emitter. The middle row shows the result of the same calculation for five atoms above the emitter. The bottom row shows the result obtained for the combination of all ten atoms.

Figure 7.4. *Forward vs. Back Scattering Iso-intensity Surfaces.* Panel A shows the three-dimensional volume view obtained from the multiple-wavenumber analysis of the top row of Figure 3, when the atoms are in the back scattering position. Panel B shows the result obtained from the middle row of Figure 3, when the atoms are in the forward scattering position. Panel C shows the result obtained from the combined case, the bottom row of Figure 3.

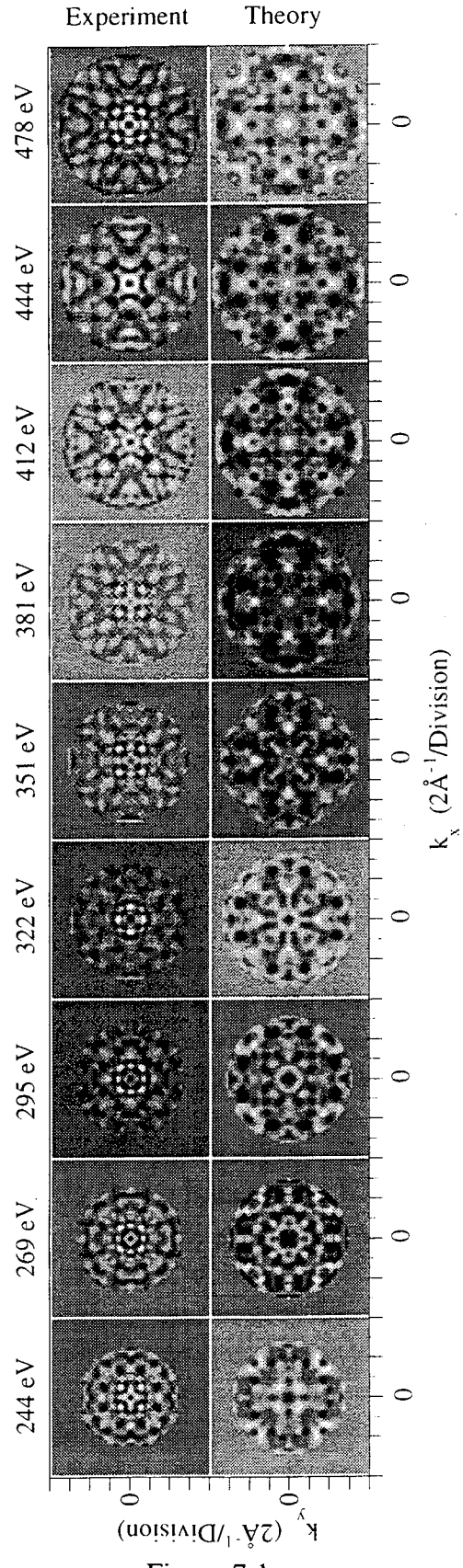
Experiment
Theory
478 eV
444 eV
412 eV
381 eV
351 eV
322 eV
295 eV
269 eV
244 eV
0
k_x (2Å^{-1}/Division)
k_y (2Å^{-1}/Division)

Figure 7.1

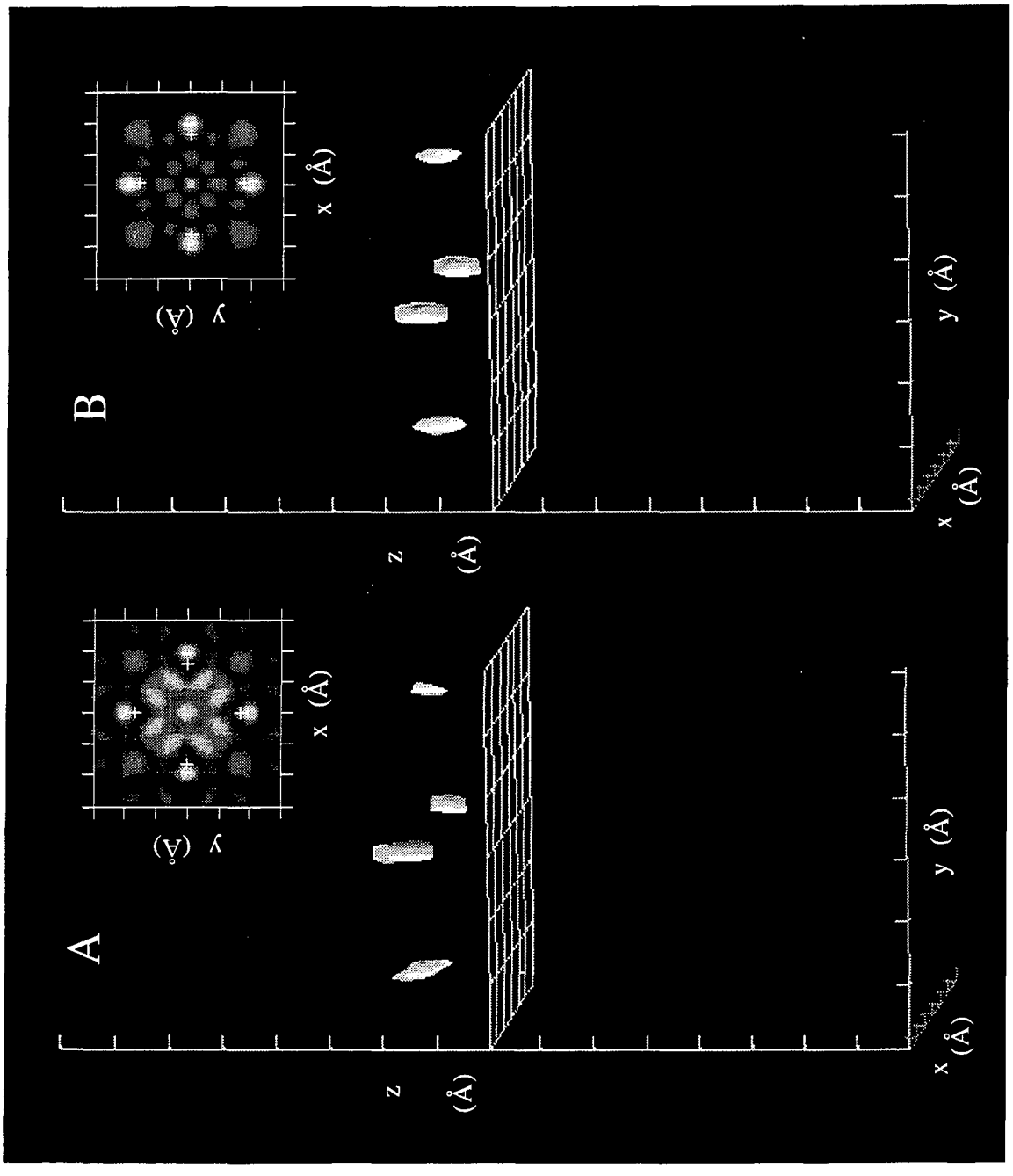

Figure 7.2

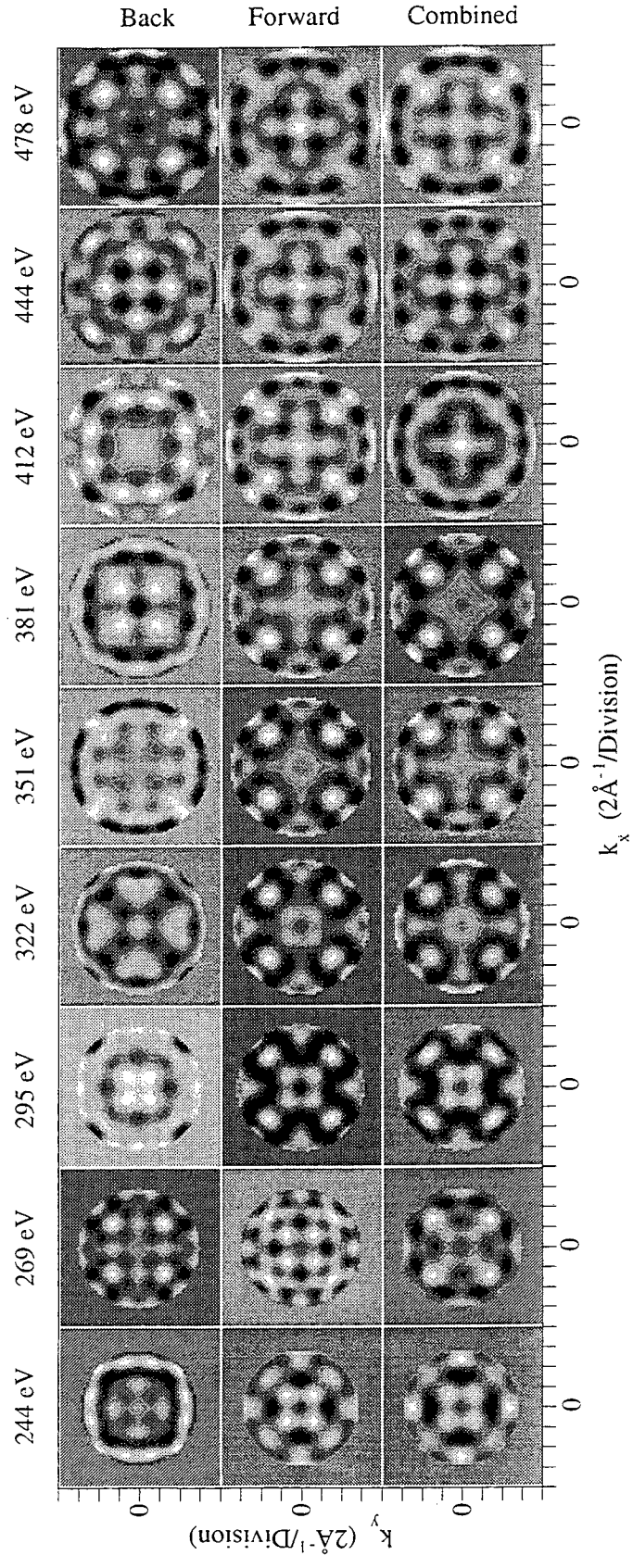
Back
Forward
Combined
478 eV
444 eV
412 eV
381 eV
351 eV
322 eV
295 eV
269 eV
244 eV
0
k_x (2Å^{-1}/Division)
k_y (2Å^{-1}/Division)

Figure 7.3

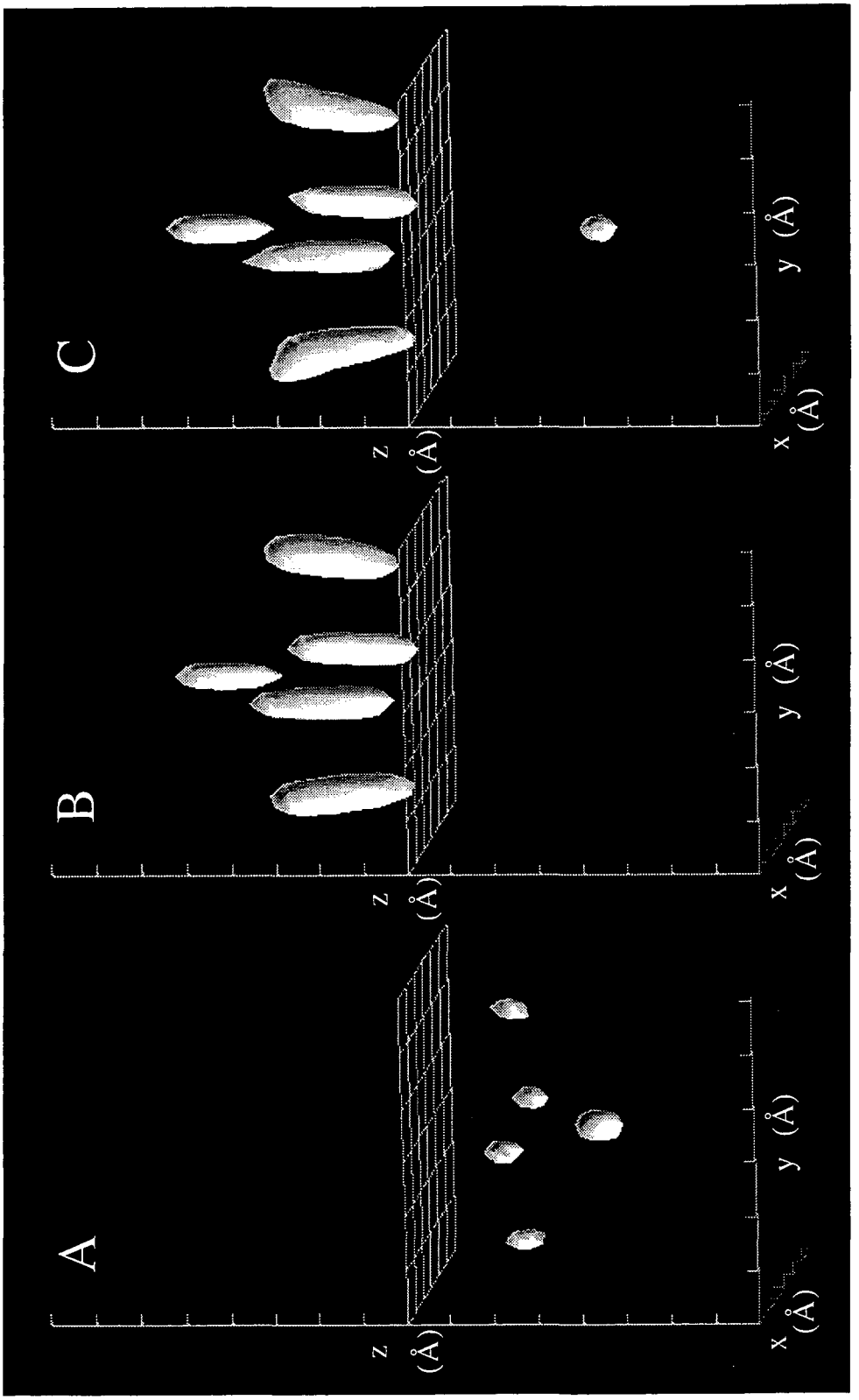

Figure 7.4

Chapter 8

CONCLUSION

Photoelectron holography shows great promise as a technique for the direct determination of surface structure. This dissertation explored the method through an observation of its application to the model system of a clean metal surface. This involved a reduction of the components of a measured electron "hologram" to a combination of pure interference and the scattering process. Although each topic discussed in the present work leads to many directions of further exploration, the material presented here should provide an adequate general background for those wishing to employ the technique to the solution of *unknown* surface structures. The first section of this concluding chapter will start with a summary of the content of the preceding chapters. The following section presents some of the more salient results of these studies. In the third section, an assessment of the technique is made based on the experience gained from this work. Future research directions suggested by these studies will be the topic of the fourth and final section.

I. Summary

The original goal of this research was to obtain experimental verification of the theoretical proposal by Szöke [1] and Barton [2] that electron waves could be used to generate holograms which could be mathematically transformed to directly reveal angstrom-scale three-dimensional structures. To this end, a platinum (111) single crystal

surface was employed as a test case for an experiment. Chapter 2 outlines in detail the process by which a holographic image was obtained from experimental data of photoemitted electrons collected with a kinetic energy of 351 eV. The strength of these images results from the fact that they are essentially free of artifacts and show atoms imaged beyond nearest neighbors, including atoms within the surface layer of the emitter. The lack of artifacts allows the images to be displayed in three-dimensional 'volume' views, which constitutes one of the strongest characteristics of this technique.

The second goal of the research was to experimentally confirm the image improvement made possible by using a multiple-wavenumber phased-sum approach [3]. In Chapter 3, eight patterns of the same Pt(111) system measured from k=8.8 to 10.2 $Å^{-1}$ (295 to 396 eV) were used to obtain reduction of the twin image and multiple-scattering artifacts present in the single wavenumber studies. This experiment was possible because of the relatively large data set of thirty-two patterns taken from k=6.0 to 12.2 $Å^{-1}$. Although all of the patterns could have been used in this study, the quality of the images was found to decrease with the full set. The lower wavenumber patterns did not successfully image the three nearest neighbors above the emitter and the patterns above 10.2 $Å^{-1}$ tended to preferentially image those same three atoms. This effect could not be adequately explained until later, in Chapter 6, when simple theoretical models could be compared with the data to reveal the cause.

Chapter 4 presents the results obtained from reducing the holography problem to the simplest ideal case of the scattering of spherical waves. In this case, the modeling showed that at certain wavenumbers atoms in various layers would disappear upon transformation. This was discovered to be the result of cancellation of interferences due to more than one scattering atom, and could be compared to the two-slit problem, where now the initial phases of the two emitters were different. This was not the first time that this type of atom-intensity variation was observed[4], but it accounts for the effect by explaining it in terms of primary interferences and purely geometrical relationships. All

additional components of the theoretical scattering physics must incorporate this interference cancellation which arises when there is more than one scattering center. This is the weakest feature of photoelectron holography as a structural probe, since the technique is based on a single scattering atom and its interference with the reference wave. Without adequate theoretical modeling, it will be hard to predict when the cancellation will occur in future implementations of the technique.

The process of holographic image formation and transformation at a single wavenumber as it relates to the scattering physics is discussed in Chapter 5. In this chapter, components beyond the purely geometry-related factors of Chapter 4 are explored. Consideration is given to the scattering factor, source wave, and experimental configuration, with some attention also directed at corrective procedures. The discussion culminates with a theoretical comparison which successfully predicts the major features of the experimental data and holographic images presented in Chapter 2.

The entire measured platinum data set and a simple theoretical comparison are presented in Chapter 6. A theoretical comparison reproduces the experimental multiple-wavenumber result of Chapter 3. Additionally, it is found that due to the limited opening angle, patterns below $k \approx 9$ $Å^{-1}$ in this experimental geometry have insufficient information to image the three nearest neighbors above the emitter. Above $k=10.2$ $Å^{-1}$, the theoretical comparison reveals that the signal-to-noise ratio of the experimental data is inadequate to produce images of atoms beyond the nearest neighbors. The photon intensity from the synchrotron radiation monochromator employed for these experiments drops significantly at higher photon energies and directly affects the signal-to-noise. Additionally, Debeye-Waller damping increases at higher wavenumbers, and this effect was not adequately modeled by these calculations. The results noted in Chapter 3 are consistent with these observations.

Finally, Chapter 7 applies the constructs developed with the platinum system to another clean metal surface data set, Cu(001), with a similar result. This analysis proves

to be an improvement over the previously published result [5]. Additionally, this data set is explored in more detail to show from basic principles that photoelectron holography tends to favor the imaging of atoms in forward scattering positions, when compared with angle-resolved photoemission-related techniques which involve a transformation over energy prior to an angular transformation in the image reconstruction. The technique will thus be applicable to sub-surface analyses.

Taken together, the work in this dissertation can be described as a study of the holographic process of imaging atomic-scale crystal structure. Model systems are used to obtain experimental data, which is then compared to ideal models of electron scattering in solids. The holographic process is analyzed in terms of the interferences due to the individual atoms which create the pattern. The origin of the measured patterns is explained with reference to first principles, confirming the imaging results and ultimately the validity of the technique. Such a straightforward comparison is necessary for verifying a method intended for utilization as a direct surface probe.

II. Results of this Work

The major contributions of this work lie in the areas of analysis optimization, how to best conduct the experiment, and determination of appropriate applications. The first component involves the study of the origin of the interference pattern in the measured data and its subsequent reduction to form an image. The second portion involves consideration of the experimental apparatus based on an understanding of the measurement. The third component uses conclusions drawn from the other two areas to determine the potential success of application of the technique to a given system of interest.

Holograms result from interference between the source and scattered waves. This principle and the position of various atoms at a crystal surface lead to the intensity patterns formed when photoemitted electrons are collected in the hemisphere above a

surface. One of the major features that this work offers is the ability to appreciate how the interference from each atom contributes to the entire pattern, and how this interference leads to holographic images. Additionally there is the area of data reduction, in which the parameters chosen at the different stages can substantially affect the appearance of the final image. A working knowledge of the source of each component in the image, real or artifact, allows for the most appropriate optimization procedure, and also the best final images.

When knowledge of the pattern collection and reduction is combined with the experimental parameters of a measurement, there is a greater likelihood of producing a successful final result. Factors such as the range of electron kinetic energy, the analyzer configuration, and the surface chosen for study are all components of potentially successful image production. These parameters are directly affected by the type of pattern which must be measured to produce correct images.

With some knowledge of the analysis procedure and the experimental configuration, another important step is the assessment of which material systems might be best suited for this type of structural probe. Distortions due to the inherent atomic scattering physics modifies the ideal interference pattern and limits the positional accuracy, but the direct nature of the technique strengthens its usefulness in structural determinations. Multiple-wavenumber studies may improve the reliability of the measurement, but measurement time and computational limitations may in some cases favor single-wavenumber applications. Although it is possible to study overlayer systems with this technique, backscattering methodologies may also be suited to accurately determining overlayer structures. Also, emitters in inequivalent sites will prove frustrating to resolve by holographic analysis. On the other hand, buried interfaces may be ideally suited to a technique which allows for true three-dimensional probing of the environment around a specifically chosen emitting atom. The system chosen will often dictate the necessary operating parameters. The work presented in this dissertation

provides a basis for choosing these parameters, and the thorough study of one system can offer some guidance to those which follow.

III. Assessment

The purpose of this section is to provide a realistic assessment of the technique of photoelectron holography based on the experience gained through these applications to real systems. A general overview of advantages and complications of such an application will be presented, followed by a statement about corrective procedures. The material covered in this section results not only from the work described in this thesis, but also from experiences of applying the technique to data from various other sources, the study of previously published material, and/or conversations with others practicing in the field. The goal is to develop a working understanding of what to expect from this technique.

As mentioned in the previous section, there are certain applications for which photoelectron holography is ideally suited, and others which may be better served by alternate structural probes. In general, the strength of this technique of holographic analysis lies in its ability to get a true direct representation of the full three-dimensional environment around an emitting atom without the need for theoretical fitting. However, because of the limited resolution of the technique of ~1Å in the workable medium electron kinetic energy range (200-600 eV), exact structural determinations of high precision should not be expected from this technique alone. Although a tentative low resolution structure may be appropriate for some applications, probably the most valuable application of the technique will be in generating initial parameters for other, more intensive theoretical comparisons. In this way, the ambiguity associated with more computationally intensive fitting schemes is removed or diminished. Additionally, unlike other direct probes which primarily take advantage of backscattering information [6,7] or directly probe the surface like STM [8] or AFM [9], photoelectron holography offers the unique ability to explore the region surrounding a buried atom. This capability may be

advantageous in the study of systems such as buried interfaces, which require such a specific probe.

Attention was given in Chapter 4 to the fact that even in an ideal scattering situation the real-space atom intensity variations may be hard to predict. Image formation depends on both the unknown atomic geometry and the wavelength of the emitted electron wave. Because this combination is impossible to predict for unknown systems, there will be a fundamental problem with single-wavenumber measurements. Better results may be obtained from the measurement of patterns at different wavenumbers, but the problem may persist. In these cases, it helps to have some type of theoretical comparison to check the validity of the measurement. Often image quality may be reduced in a multiple-wavenumber result if several of the combined patterns do not form valid images independently.

Another challenge in the interpretation of this data is understanding the origin of artifacts, or unphysical intensity, apparent in the real-space transformed images. Locations of high intensity in the final reconstructions are generally due to symmetric areas of similar intensity which exist in the pattern prior to image integral transformation. These intensities are often due to the expected scattering, and for the most part are valuable for obtaining the final image. However, symmetric areas of intensity can also result from strong forward scattering [10], from "diffraction peaks" which arise from scattered wave interferences [11], or from random noise which appears in a pattern. Often, the unphysical intensities may fall at the same location as real peaks, which can lead to confusion. In most cases, experience with processing holographic data helps to determine which artifacts are real and which are spurious. Simple theoretical calculations can also be useful for comparison and clarification.

A question which must be considered in detail is the data reduction process. Of concern here are primarily issues of corrective procedures. We have always been proponents of the direct qualities of the technique. In this respect, any treatment of the

data which involves theoretical modification is considered unacceptable. The reasoning for this approach is simply the fact that the method should be applicable to unknown systems. Poorer resolution of the obtained images is preferable to a questionable higher quality result obtained with structural knowledge of the "unknown" system. The multiple-wavenumber analysis scheme can be employed to substantially reduce twin images and some multiple scattering artifacts. Another unobtrusive correction we support is the Gaussian convolution with subsequent division [12], which is used in this work and described in detail in Chapter 5. The important thing to remember in all of these cases is that the correct result will always be apparent before further improvement are made through applied corrective methods.

Photoelectron holography can be used successfully for surface imaging. There are some applications to which it is better suited than others. In all cases, it is necessary that the user understand some of the fundamental concepts behind the image formation and analysis in order to produce the most useful images.

IV. Future Directions

It is difficult to ask more from a momentum-resolved ($\boldsymbol{k}$) photoelectron intensity experiment than the capability of measuring all electron kinetic energies at all angles. This work represents a significant advance in the extraction of structural information from measurements of photoelectron interference. Effectively, we perform a transformation from k-space to real space in three dimensions and the success of these experiments confirms the viability of the method. If it can be done on one system, other systems should necessarily follow. Future goals might involve both the refinement of the methods and procedures described in this thesis, as well as developments in areas which as yet remain unexplored. The methodology developed in these studies may also be useful in applications that are not necessarily directly related to the field of photoelectron spectroscopy or even surface science.

Immediately achievable goals beyond this thesis should include the study of new systems of unknown structure. These include surface overlayers, multi-component bulk systems, and interfaces. Many of these studies are currently in progress. Variations of the working parameters will allow for more studies along the same lines. For example, surface magnetism can be explored using angular distributions of spin-polarized electrons [13]. A wide range of materials fall into these categories and this holographic technique will definitely prove beneficial.

Additionally, following the same data analysis procedure, other sources of excitation or emitted photons and particles may be explored. All that is necessary is the short wavelength coherent source wave and a method of detecting the interference intensity. Likewise, other experimental configurations will offer more efficient collection of the necessary data and continued increases in computer speed and memory will potentially lead to real-time transformations. In the some cases, it may even be possible to perform complete experiments in a laboratory without requiring a necessity of a synchrotron as an excitation source.

Other components of this work may extend to other fields. On a broader scope, this work develops a system of two-dimensional data collection, reduction, and storage on a large scale. Additionally, two and three-dimensional transformations combine elements from optics and electron scattering. Because this work involves the mathematical creation and processing of holographic images, these formalisms can also be applied to other computer-generated holographic applications. Development of analyzers which perform this type of measurement efficiently will also find uses in many other experiments that require a large two-dimensional energy selective analyzer. All of these examples will provide exciting routes for exploration and discovery.

V. Conclusion

This final chapter attempts to unify the material presented in the earlier chapters for the convenience of the reader. A summary of that work was presented, followed by a brief description of the conclusions which could be drawn. A realistic assessment of the technique was made based on experience gained through the research. Finally, ideas of directions for continued research were suggested. The technique of photoelectron holography should now be more firmly established for its application to more complex systems.

References

[1] A. Szoke, in *Short Wavelength Coherent Radiation: Generation and Applications*, edited by D.T. Atwood and J. Bokor (AIP Conf. Proc. 146, New York, 1986).

[2] J.J. Barton, Phys. Rev. Lett. 61 (1988) 1356.

[3] J.J. Barton and L.J. Terminello, in Structure of Surfaces III, Milwaukee, edited by S.Y. Tong, M.A. Van Hove, X. Xide, and K. Takayanagi (Springer-Verlag, Berlin, 1991) 107; J.J. Barton, Phys. Rev. Lett. 67 (1991) 3106.

[4] P. M. Len, S. Thevuthasan, C.S. Fadley, A.P. Kaduwela, and M.A. Van Hove, Phys. Rev. B. 50 (1994) 11275.

[5] L.J. Terminello, J.J. Barton and D.A. Lapiano-Smith, Phys. Rev. Lett. 70 (1993) 599; J. Vac. Sci. Technol. B 10 (1992) 2088.

[6] J.J. Barton, C.C. Bahr, Z. Hussain, S.W. Robey, J.G. Tobin, L.E. Klebanoff, and D.A. Shirley, Phys. Rev. Lett. 51 (1983) 272.

[7] J. G. Tobin, G.D. Waddill, H. Li, and S.Y. Tong, Phys. Rev. Lett. 71 (1993) 4150.

[8] G. Binnig and H. Rohrer, Helv. Phys. Acta 55, (1982) 726.

[9] G. Binnig, C.F. Quate, and C. Gerber, Phys. Rev. Lett. 12 (1986) 930.

[10] G.R. Harp, D.K. Saldin and B.P. Tonner, Phys. Rev. Lett. 65 (1990) 1012; G.R. Harp, D.K. Saldin and B.P. Tonner, Phys. Rev. B. 42 (1990) 9199.

[11] S. Thevuthasan, G.S. Herman, A.P. Kaduwela, R.S. Saiki, Y.J. Kim, W. Niemczura, M. Burger and C.S. Fadley, Phys. Rev. Lett. 67 (1991) 469.

[12] G.R. Harp, D.K. Saldin, X. Chen, Z.-L. Han and B.P Tonner, J. Electr. Spectros. Relat. Phenom. 57 (1991) 331.

[13] A.P. Kaduwela, Z. Wang, S. Thevuthasan, M.A. Van Hove and C.S. Fadley, Phys. Rev. B. 50 (1994) 9656.

LAWRENCE BERKELEY LABORATORY
UNIVERSITY OF CALIFORNIA
TECHNICAL INFORMATION DEPARTMENT
BERKELEY, CALIFORNIA 94720